# UNIVERSITA' DEGLI STUDI DI PADOVA

Università degli Studi di Padova

Dipartimento di Scienze Chimiche

SCUOLA DI DOTTORATO DI RICERCA IN SCIENZA ED INGEGNERIA DEI MATERIALI

XX CICLO

**MODELING THE OPTICAL PROPERTIES OF NANOCLUSTER-BASED FUNCTIONAL PLASMONIC MATERIALS**

**Direttore della Scuola :** Ch.mo Prof. Gaetano Granozzi

**Supervisore** :Ch.mo Prof. Giovanni Mattei

**Dottorand**o : Giovanni Pellegrini

DATA CONSEGNA TESI
31 gennaio 2008

# Contents

**Introduction** v

**I. Theory** 1

**1. Generalized Multiparticle Mie theory approach: theory and implementation** 3
1.1. Introduction . . . 3
1.2. Generalized Multiparticle Mie problem . . . 4
1.2.1. Statement of the problem . . . 4
1.2.2. Extension of the Mie theory . . . 5
1.2.3. Solution of the linear system . . . 9
1.2.4. Extinction, scattering and absorption cross sections of a set of spheres . . . 10
1.3. Appendix: relevant numerical aspects of GMM theory . . . 12
1.3.1. Computation of radial functions: spherical Bessel and Riccati-Bessel functions . . . 13
1.3.2. Computation of angular functions: $\tau_{mn}$, $\pi_{mn}$, associated Legendre polynomials and rotation matrix elements . . . 14
1.3.3. Computation of Gaunt coefficients . . . 17
1.3.4. Computation of classical Mie coefficients . . . 18
1.3.5. Computation of vector translation coefficients . . . 18
1.3.6. Matrix vector multiplication . . . 19
1.3.7. Computation of local field . . . 21

**2. Generalized Multiparticle Mie: far-field** 25
2.1. Introduction . . . 25
2.2. Extinction properties of nanoparticle dimers . . . 25
2.3. Extinction properties of nanoparticle chains . . . 29
2.3.1. Nanoparticle chains . . . 29
2.3.2. Nanoparticle chains supporting photonic modes . . . 30
2.4. Conclusion . . . 31

**3. Generalized Multiparticle Mie: local-field** 33
3.1. Introduction . . . 33
3.2. Local-field enhancement properties of nanoparticle dimers . . . 34
3.3. Local-field enhancement properties of nanoparticle chains . . . 36
3.3.1. Nanoparticle chains . . . 36

3.3.2. Self similar chains . . . 36
3.4. Conclusion . . . 39

**II. Optical properties of metallic nanoplanets 41**

**4. Synthesis and characterization of bimetallic nanoplanets 43**
4.1. Introduction . . . 43
4.2. Synthesis and characterization of Au-Ag alloy nanoclusters . . . 44
4.3. Synthesis and characterization of Au-Ag alloy nanoplanets . . . 44
4.3.1. Conclusions . . . 49

**5. Modeling far- and local-field properties of bimetallic nanoplanets 51**
5.1. Introduction . . . 51
5.2. Far-field properties of alloy nanoplanets . . . 52
5.2.1. Nanoplanet extinction properties by Generalized Multi-particle Mie approach . . . 52
5.2.2. Nanoplanet far-field properties by Hybrid Mie Maxwell-Garnett approach . . . 54
5.3. Nanoplanet local-field properties by GMM approach . . . 56
5.4. Conclusions . . . 59

**6. Local-field enhancement optimization in metallic nanoplanets 61**
6.1. Introduction . . . 61
6.2. Local-field tuning in strongly asymmetric dimer . . . 61
6.3. Local-field enhancement in metallic nanoplanets . . . 67
6.4. Conclusions . . . 71

**III. Multiple coupled cluster plasmonic nanoantennae 73**

**7. Plasmonic nanoantennae in the GMM framework 75**
7.1. Introduction . . . 75
7.2. Methods: GMM framework and the multisphere nanoantenna problem . . . 76
7.3. Application of GMM approach to the single spherical antenna problem . . . 78
7.4. Application of GMM approach to the dimer nanoantennae . . . 80
7.5. Conclusions . . . 83

**8. Tunable efficiency enhancement via mixed plasmonic-photonic modes 85**
8.1. Introduction . . . 85
8.2. Light extraction properties of single building blocks . . . 85
8.3. Light extraction via mixed plasmonic-photonic modes . . . 86
8.4. Conclusions . . . 89

**Summary 91**

## Contents

**Sommario** **93**

**List of publications** **95**

# Introduction

Metal nanoparticles peculiar optical properties may be used to manipulate light behavior at the nanoscale dimension [1; 2]. Metal nanoparticles provide this chance since they support surface plasmons, i.e., collective oscillations of the conduction electrons. These oscillations are resonant in the visible range, at frequencies that can be tailored by engineering the nanoparticle size, shape or, in the last years, interparticle coupling in nanocluster ensembles. Resonances originate from the fact that the conduction electrons are confined within the nanoparticle, therefore the electromagnetically induced displacement of the conduction electrons sets up a surface polarization. Due to the restoring force of the positive background, free electrons are bound to the nanoparticle, and the oscillator strength of the conduction electrons is compressed into a rather narrow spectral band, causing the nanoparticle to be strongly polarizable at the plasmon resonance frequency. On resonance, the energy supplied by an incident electromagnetic wave is effectively drawn into the particle by the large polarizability. The result is a field enhancement concentrated volume comparable with the particle dimension. The energy that is captured by the plasmons is partially dissipated in the metal and partly reradiated in the far-field. The relative intensity of the two processes depends on the nanoparticle composition and geometry, as well as on the interparticle coupling if coupled ensembles are concerned. Noble metals, and in particular silver and gold are the materials with the smallest dissipative losses at optical frequencies, and thus they are characterized by the strongest resonant behavior. For smaller particle dimension the dissipation dominates the plasmon decay, whereas reradiation becomes important for larger sizes. By engineering the nanoparticle geometry, and even more by controlling the interparticle electrodynamic coupling in interacting ensembles, it is then possible to control how the captured electromagnetic energy is manipulated and distributed.

The peculiar optical properties of metal nanoparticles make them very attractive for a wide spectrum of applications. Glass-embedded noble metal nanoparticles exhibit strong surface plasmon absorption in the visible spectrum [1; 2], and can increase the third-order susceptibility $\chi^{(3)}$ of the matrix by several orders of magnitude [3]. In the case of spherical isolated metal nanoparticles the plasmon resonance frequency and electromagnetic field configuration depend on the cluster size and on the metal and matrix dielectric functions. In ensembles of interacting clusters the plasmon peak position and the local-field are influenced by the interparticle electromagnetic coupling. Parameters like particle size, number and relative position as well as incident light polarization state influence the extinction spectrum and the local-field enhancement [4–6]. If metal alloy nanoparticles are considered, alloy composition is one additional parameter to play with for the plasmon tuning [7; 8]. Given their far- and local-field

properties, strongly coupled clusters attracted much interest in the field of single molecule sensing applications, such as surface enhanced Raman scattering and molecular plasmon rulers [9; 10], and are promising for miniature nonlinear optical elements and polarization sensitive photonic devices [11; 12]. The possibility of three-dimensional (3-D) subwavelength confinement and plasmon waveguiding has been explored as well [13; 14].

Recently much attention is also devoted to metal nanoparticles employed as optical nanoantennae, i.e. as devices that convert localized energy into free propagating radiation [15]. Plasmons strongly influence the luminescence features of optical emitters near a metal nanoparticle surface, with the coupling of an emitter to plasmon modes affecting both the emitter radiative and nonradiative recombination rates. This phenomenon is based on the principle that the strength with which an emitter couples with the electromagnetic field depends on the emitter electromagnetic environment [16]. This environment is modified by placing strongly polarizable objects in the vicinity of the emitter, where in our case ensembles of interacting nanoparticle will be the choice of reference. In the same way the energy is captured from an incident plane wave, so the emitter transfers its energy to the plasmon modes, where the energy is dissipated in the particle or reradiated in the far-field. The first process is responsible for enhanced nonradiative recombination, the latter for enhanced radiative decay. The balance between dissipation and far-field radiation depends strongly on the antenna topology and geometry, therefore the engineering of efficient particle coupling schemes in terms of light extraction is of paramount importance for the optimization of nanoantenna enhanced luminescence. Despite the fact that metals are rather lossy in the optical regime, the luminescence intensity of optical emitters can potentially be enhanced by several orders of magnitude by metallic nanoantennae.

Plasmonic properties of noble metal coupled nanoparticles, as well as their application in the design of efficient light extraction devices, are the principal subjects of this thesis.

## Content of this thesis

This thesis focuses on modeling the optical properties of nanocluster-based plasmonic materials. As a first step we develop reliable theoretical tools in the framework of Generalized Multiparticle Mie (GMM) theory [17]. The method is first applied to study the optical properties of basic coupled sphere plasmonic ensembles, then extending its use to the analysis of extremely complex, strongly coupled structures which are obtained by ion beam processing. These systems will be called nanoplanets [8](i.e. a central cluster surrounded by small satellite clusters very close to its surface). In the end the already tackled plasmonic ensembles are employed as metallic nanoantennae, taking benefit of the high flexibility provided by these strongly coupled structures.

Part I of this thesis describes the theoretical aspects of the GMM approach as well as its application to basic plasmonic structures:

- Chapter 1 describes the GMM derivation and formalism. Maxwell equa-

tions are solved by using a multipolar expansion approach and explicit expressions for fundamental physical quantities such as internal and scattered fields and absorption and scattering cross-sections are derived;

- Chapter 2 regards the application of GMM formalism to the study of far-field properties of basic plasmonic structures such as noble metal sphere dimers and chains. Influence on the extinction spectra of structure composition and geometrical parameters are studied;

- Chapter 3 focuses on the local-field investigation of basic sphere ensembles. Field focusing and enhancement properties are studied as a function of system geometrical and compositional features. Combined analysis of far- and local-field investigations allows a good comprehension of the physical phenomena underlying the optical properties of coupled plasmonic structures.

Part II of this thesis describes the application of GMM theory to the analysis of metal nanoplanet optical properties:

- Chapter 4 describes the ion beam processing steps which bring to the synthesis of AuAg alloy nanoplanets. Topological nanoplanet features are then discussed as a function of ion beam synthesis parameters;

- Chapter 5 focuses on the extinction properties of alloy nanoplanets, and on their interpretation on the basis of GMM results. Local-field GMM simulations finally allows to draws connection between nanoplanet far- and local-field features.

- Chapter 6 regards predictive application of GMM theory. Our theoretical approach is applied to model nanoplanets whose composition and topology are tailored in order to maximize plasmon tuning and local-field enhancement features.

Part III finally describes, by the GMM approach, the light extraction properties of multiple coupled clusters nanoantennae:

- Chapter 7 describes light extraction properties of single sphere and dimer nanoantennae as a function of their geometrical properties. It is shown that GMM approach is able to handle nanoantenna problems just by integrating minor changes in the formalism;

- Chapter 8 describes an original approach to light extraction problems, which allows to overcome some of the limitations imposed by classical nanoantennae. Regular nanospheres array supporting mixed plasmonic-photonic modes are used as nanoantennae, obtaining tunable and wavelength selective recombination rate enhancement.

Altogether this thesis provides an interesting insight in the plasmonic properties of functional multiple coupled cluster nanostructures.

# Part I.

# Theory

# 1. Generalized Multiparticle Mie theory approach: theory and implementation

## 1.1. Introduction

During the last two decades there has been a growing interest in interaction of light with metallic nanostructures, leading to the the newly born field of plasmonics, which holds great promises for the creation of integrated and nanoscale optical devices, bridging the gap between current nanoelectronics and microphotonics [18–26]. Among the wealth of plasmonic structures, clusters of interacting metal nanoparticles have attracted a considerable attention for their peculiar far- and local-field optical properties. High local-field enhancements present at nanoparticle junctions are suitable for Surface Enhanced Raman Scattering (SERS), sensing application, and the synthesis of materials with large third-order susceptibility $\chi^{(3)}$ [9; 11; 27–29]. Strong electrodynamic coupling allows to obtain three-dimensional sub-wavelength confinement, along with plasmon waveguiding on a typical lengthscale of hundreds of nanometers [13; 30–34], and polarization sensitive devices [4]. Finally plasmon resonance dependence on the interparticle separations in sphere dimers open the possibility to build effective plasmon rulers, that may be employed on length scales which can not be explored by conventional FRET techniques [10].

A further phenomenon related to large field enhancements is the boosting of the luminescence of an optical emitter in proximity of metallic particles. In this case nanoparticles are employed as nanoantennae, i.e. as devices that convert localized energy into free propagating radiation. Considerable effort has been put in the design of efficient nanoantennae characterized by different geometries, with promising results coming from nanoantennae composed by coupled nanoscopic ellipsoids [15].

The theoretical framework which is most widely adopted in order to study the optical properties of metallic nanoparticle is probably constituted by the well known Mie theory [1]. This method is based on a multipole expansion of the involved electric and magnetic fields, with its application limited to systems characterized by a spherical symmetry [1; 2].

Different theoretical approaches overcome the limitations imposed by Mie theory: to name but a few we mention finite-difference time-domain (FDTD) calculations, boundary element method (BEM), multiple multipole (MMP) method and Generalized Multiparticle Mie (GMM) theory [17; 28; 35; 36]. In spite of the limitations concerning the geometries which can be possibly modeled, multipole expansion GMM approach was chosen as the theoretical

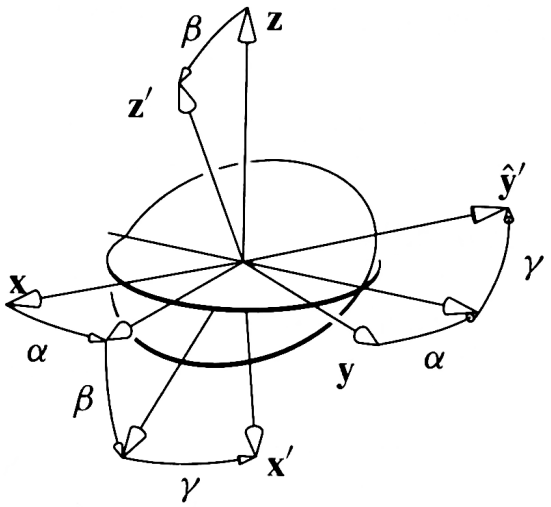


Figure 1.1.: $(x, y, z)$ and $(x', y', z')$ reference frames obtained by a $(\alpha, \beta, \gamma)$ Euler angle rotation following the **zyz** convention.

framework to be adopted throughout this thesis, since it offers advantages from the point of view of computational requirements, maximum dimension of the system to be modeled and result accuracy.

In the first part of this chapter we present a description of Generalized Mie theoretical framework: the multisphere problem is stated and solved with the aid of translation theorems [17]. Once that the expansion coefficients are know the calculation of relevant far-field and local-field quantities may be carried on in the second part of the chapter. Relevant numerical aspects of the calculation are reported in the appendices.

## 1.2. Generalized Multiparticle Mie problem

### 1.2.1. Statement of the problem

We consider a cluster of $N_S$ non-intersecting, homogeneous spheres with radius $R^j$ and known complex dielectric function $\varepsilon^j$ for the $j$-th sphere. The aggregate is embedded in a non-absorbing medium characterized by dielectric constant $\varepsilon_m$ and vacuum magnetic permeability, where $\sqrt{\varepsilon_m} = n_m$, with $n_m$ the refractive index of the medium. Each sphere is located at a position $\mathbf{r}^{j,0} = \hat{\mathbf{e}}_x X^j + \hat{\mathbf{e}}_y Y^j + \hat{\mathbf{e}}_z Z^j$ in a coordinate system fixed to the particle ensemble (cluster reference frame). The distance between two particles is defined as $\mathbf{r}^{j,l} = \mathbf{r}^{j,0} - \mathbf{r}^{l,0}$ with $g^{j,l} \equiv g = r^{j,l} - (R^j + R^l)$ and of course $|\mathbf{r}^{j,l}| = r^{j,l} \geq R^j + R^l$. We suppose that the incident beam illuminating each sphere can be represented by elementary spherical waves about the center of each sphere. The incident wave is monochromatic and arbitrary in profile, but in most cases a linearly polarized plane wave is considered. The state of the linearly polarized incident field may be described by the Euler angles $\alpha$, $\beta$ and $\gamma$, with this meaning that the cluster reference frame $(x, y, z)$ is rotated by the Euler angles $(\alpha, \beta, \gamma)$, following the **zyz**

convention, to get the new incident reference frame $(x', y', z')$. The wavevector can be defined as $\mathbf{k} = \frac{2\pi n_m}{\lambda}\hat{\mathbf{e}}'_z$, with $\hat{\mathbf{e}}'_z = \sin\beta\cos\alpha\,\hat{\mathbf{e}}_x + \sin\beta\sin\alpha\,\hat{\mathbf{e}}_y + \cos\beta\,\hat{\mathbf{e}}_z$, and polarization along $x'$ axis (parallel case, $\|$) or $y'$ axis (normal case, $\perp$). The scattering, extinction and local-field properties of such a cluster of spheres will be examined analytically.

### 1.2.2. Extension of the Mie theory

Given the adopted approach it is now needed to express the electromagnetic fields in infinite series expansions at all points in the space, more specifically in terms of elementary spherical waves about a fixed center.

We are dealing with time harmonic electromagnetic fields in a sourceless, isotropic and homogeneous medium: fields $\mathbf{E}$ and $\mathbf{H}$ are thus divergence free and satisfy the vector wave equations

$$\nabla \times \nabla \times \mathbf{E} - k^2\mathbf{E} = 0, \qquad \nabla \times \nabla \times \mathbf{H} - k^2\mathbf{H} = 0, \tag{1.1}$$

where $k = |\mathbf{k}|$ is the wavenumber. A set of linearly independent solutions in spherical polar coordinates $(r, \theta, \phi)$ is given by the spherical vector wave functions $\mathbf{M}_{mn}$, and $\mathbf{N}_{mn}$ which may be written as

$$\begin{aligned}
\mathbf{N}^{(J)}_{mn}(\rho,\theta,\phi) &= \Bigg\{\hat{\mathbf{e}}_r n(n+1)P^m_n(\cos\theta)\frac{z^{(J)}_n(\rho)}{\rho} \\
&\quad + \Big[\hat{\mathbf{e}}_\theta\tau_{mn}(\cos\theta) + \hat{\mathbf{e}}_\phi i\pi_{mn}(\cos\theta)\Big]\frac{(\rho z^{(J)}_n(\rho))'}{\rho}\Bigg\}, \\
\mathbf{M}^{(J)}_{mn}(\rho,\theta,\phi) &= \Big[\hat{\mathbf{e}}_\theta i\pi_{mn}(\cos\theta) - \hat{\mathbf{e}}_\phi\tau_{mn}(\cos\theta)\Big]z^{(J)}_n(\rho)e^{im\phi},
\end{aligned} \tag{1.2}$$

where $\hat{\mathbf{e}}_r$, $\hat{\mathbf{e}}_\theta$ and $\hat{\mathbf{e}}_\phi$ are unit vector in spherical coordinates, $\rho = kr$ and the prime symbol stands for the derivative with respect to the function argument; $z^{(J)}_n$ represents an appropriately selected spherical Bessel function, i.e.

$$z^{(1)}_n = j_n, \quad z^{(2)}_n = y_n, \quad z^{(3)}_n = h^{(1)}_n, \quad z^{(4)}_n = h^{(2)}_n, \tag{1.3}$$

where $j_n$ and $y_n$ are spherical Bessel functions of the first and second kind and $h^{(1,2)}_n$ are spherical Hankel functions of the first and second kind(see Sec.1.3.1). $P^m_n$ is the associated Legendre function of the first kind, with $\tau_{mn}$, $\pi_{mn}$ defined as:

$$\begin{aligned}
\tau_{mn}(\cos\theta) &= \frac{d}{d\theta}P^m_n(\cos\theta), \\
\pi_{mn}(\cos\theta) &= \frac{m}{\sin\theta}P^m_n(\cos\theta).
\end{aligned} \tag{1.4}$$

Degree $n$ and order $m$ are integers with $1 \le n < \infty$ and $-n \le m \le n$. Relevant recursion formulae for $z^{(J)}_n$ and $\tau_{mn}$, $\pi_{mn}$ are given in the appendix at the end of the chapter.

It is now assumed that all the involved fields may be expanded in vector spherical wave functions in reference frames located at the center of each sphere of the aggregate:

$$\mathbf{E}^j_{\text{inc},0} = -i\sum_{n=0}^{\infty}\sum_{m=-n}^{n} E_{mn}\left[p^j_{mn}\mathbf{N}^{(1)}_{mn}(\rho,\theta,\phi) + q^j_{mn}\mathbf{M}^{(1)}_{mn}(\rho,\theta,\phi)\right],$$
$$\mathbf{H}^j_{\text{inc},0} = -\frac{k}{\omega\mu_0}\sum_{n=0}^{\infty}\sum_{m=-n}^{n} E_{mn}\left[q^j_{mn}\mathbf{N}^{(1)}_{mn}(\rho,\theta,\phi) + p^j_{mn}\mathbf{M}^{(1)}_{mn}(\rho,\theta,\phi)\right],$$

$$\mathbf{E}^j_{\text{sca}} = i\sum_{n=1}^{\infty}\sum_{m=-n}^{n} E_{mn}\left[a^j_{mn}\mathbf{N}^{(3)}_{mn}(\rho,\theta,\phi) + b^j_{mn}\mathbf{M}^{(3)}_{mn}(\rho,\theta,\phi)\right],$$
$$\mathbf{H}^j_{\text{sca}} = \frac{k}{\omega\mu_0}\sum_{n=1}^{\infty}\sum_{m=-n}^{n} E_{mn}\left[b^j_{mn}\mathbf{N}^{(3)}_{mn}(\rho,\theta,\phi) + a^j_{mn}\mathbf{M}^{(3)}_{mn}(\rho,\theta,\phi)\right],$$

$$\mathbf{E}^j_{\text{int}} = -i\sum_{n=1}^{\infty}\sum_{m=-n}^{n} E_{mn}\left[d^j_{mn}\mathbf{N}^{(1)}_{mn}(\rho,\theta,\phi) + c^j_{mn}\mathbf{M}^{(1)}_{mn}(\rho,\theta,\phi)\right],$$
$$\mathbf{H}^j_{\text{int}} = -\frac{k^j}{\omega\mu_0}\sum_{n=1}^{\infty}\sum_{m=-n}^{n} E_{mn}\left[c^j_{mn}\mathbf{N}^{(1)}_{mn}(\rho,\theta,\phi) + d^j_{mn}\mathbf{M}^{(1)}_{mn}(\rho,\theta,\phi)\right],$$

$$\mathbf{E}^j_{\text{inc,tot}} = -i\sum_{n=1}^{N}\sum_{m=-n}^{n} E_{mn}\left[P^j_{mn}\mathbf{N}^{(1)}_{mn}(\rho,\theta,\phi) + Q^j_{mn}\mathbf{M}^{(1)}_{mn}(\rho,\theta,\phi)\right]$$
$$\mathbf{H}^j_{\text{inc,tot}} = -\frac{k}{\omega\mu_0}\sum_{n=1}^{N}\sum_{m=-n}^{n} E_{mn}\left[Q^j_{mn}\mathbf{N}^{(1)}_{mn}(\rho,\theta,\phi) + P^j_{mn}\mathbf{M}^{(1)}_{mn}(\rho,\theta,\phi)\right], \quad (1.5)$$

where $E_{mn} = E_0 i^n C_{mn}$ with

$$C_{mn} = \sqrt{\frac{(2n+1)(n-m)!}{n(n+1)(n+m)!}}. \quad (1.6)$$

The above fields are expanded in the reference frame of the $j$-th sphere: $(\mathbf{E}^j_{\text{inc},0}, \mathbf{H}^j_{\text{inc},0})$ are the initial incident fields, in most cases constituted by a linearly polarized plane wave, $(\mathbf{E}^j_{\text{sca}}, \mathbf{H}^j_{\text{sca}})$ are the fields scattered by the $j$-th sphere, $(\mathbf{E}^j_{\text{int}}, \mathbf{H}^j_{\text{int}})$ are the internal fields of the $j$-th sphere and $(\mathbf{E}^j_{\text{inc,tot}}, \mathbf{H}^j_{\text{inc,tot}})$ are the total fields incident on the $j$-th sphere, including the initial incident wave and the scattered fields of all the spheres in the cluster. As it follows from the field definitions, $(p^j_{mn}, q^j_{mn})$ are the expansion coefficients of the initial incident field, $(a^j_{mn}, b^j_{mn})$ are the scattering expansion coefficients of the $j$-th sphere, analogue to the $(a_n, b_n)$ single sphere Mie coefficients as they appear in Ref.[1], $(c^j_{mn}, d^j_{mn})$ are the internal field coefficients, corresponding to $(c_n, d_n)$, again as in [1], while $(P^j_{mn}, Q^j_{mn})$ are the expansion coefficients of the whole field striking the $j$-th

sphere. Concerning the internal fields we notice that $k^j$ is the wavenumber inside the $j$-th sphere while, as may be seen in Eq.(1.5), material magnetic permeability is always chosen to be the one of the vacuum. Harmonic time dependence is assumed for all the fields, and suppressed in the reported equations for simplicity.

The solution of the multisphere problem relies on the determination of the expansion coefficients. In order to do this standard boundary conditions are applied at the surface of each sphere, i.e. continuity of the parallel compontent of the fields is imposed. Taking the $j$-th sphere as an example we get

$$\left[\mathbf{E}^j_{\text{inc,tot}} + \mathbf{E}^j_{\text{sca}} - \mathbf{E}^j_{\text{int}}\right] \times \hat{\mathbf{e}}^j_r = \left[\mathbf{H}^j_{\text{inc,tot}}\mathbf{H}^j_{\text{sca}} - \mathbf{H}^j_{\text{int}}\right] \times \hat{\mathbf{e}}^j_r = 0, \tag{1.7}$$

which in component form at $r^j = a^j$ turns out to be

$$\begin{aligned} &E^{j\theta}_{\text{inc,tot}} + E^{j\theta}_{\text{sca}} = E^{j\theta}_{\text{int}}, \quad E^{j\phi}_{\text{inc,tot}} + E^{j\phi}_{\text{sca}} = E^{j\phi}_{\text{int}}, \\ &H^{j\theta}_{\text{inc,tot}} + H^{j\theta}_{\text{sca}} = H^{j\theta}_{\text{int}}, \quad H^{j\phi}_{\text{inc,tot}} + H^{j\phi}_{\text{sca}} = H^{j\phi}_{\text{int}}. \end{aligned} \tag{1.8}$$

The above boundary conditions, together with equations (1.2) and (1.5), give rise to a set of linear equations where interaction expansion coefficients appear as the unknown:

$$\begin{aligned} &j_n(m^j x^j)\, c^j_{mn} + h^{(1)}_n(x^j)\, b^j_{mn} = Q^j_{mn}\, j_n(x^j), \\ &[m^j x^j j_n(m^j x^j)]'\, c^j_{mn} + [x^j h^{(1)}_n(x^j)]' = Q^j_{mn}[x^j j_n(x^j)]', \\ &m^j j_n(m^j x^j)\, d^j_{mn} + h^{(1)}_n(x^j)\, a^j_{mn} = P^j_{mn}\, j_n(x^j), \\ &[m^j x^j j_n(m^j x^j)]'\, d^j_{mn} + m^j[x^j h^{(1)}_n(x^j)]'\, a^j_{mn} = P^j_{mn}\, m^j[x^j j_n(x^j)]. \end{aligned} \tag{1.9}$$

In Eqs.(1.9) the prime stands for a differentiation with respect to the function argument, with size parameter $x^j$ and relative refractive index $m^j$ of the $j$-th sphere defined as:

$$x^j = ka^j = \frac{2\pi n_m a^j}{\lambda}, \quad m^j = \sqrt{\frac{\epsilon^j}{\epsilon_m}} = \frac{n^j}{n_m}, \tag{1.10}$$

where $n^j$ is the complex refractive index of the $j$-th sphere and $\lambda$ the wavelength of the incident radiation. By introducing the classical Mie coefficients $a_n$,$b_n$, $c_n$ and $d_n$ it may be shown that is is possible to recast Eqs.(1.9) in the following compact form [17]:

$$\begin{aligned} &a^j_{mn} = a_n\, P^j_{mn}, \quad b^j_{mn} = b_n\, Q^j_{mn}, \\ &c^j_{mn} = c_n\, Q^j_{mn}, \quad d^j_{mn} = d_n\, P^j_{mn}. \end{aligned} \tag{1.11}$$

This result reveals that scattering properties of an isolated homogeneous sphere can be univocally related to its Mie scattering properties and to the profile of

the striking electromagnetic wave, no matter how complex the profile, provided that it can be expanded in spherical harmonics. This means that in order to determine the scattering properties of a sphere in a general beam the only additional task to perform is to determine the expansion coefficients of the incident field.

We are now left with the problem of explicitly determining the the expansion coefficients of the total incident field $(P^j_{mn}, Q^j_{mn})$ which is, as already noticed, constituted by the initial incident field plus the fields scattered by all the particles composing the cluster. Therefore, taking this time the $l$-th sphere as an example, the problem can be reduced to the determination of the expansion coefficients for the initial incident beam and the scattered fields by all the spheres, in the $l$-th reference frame. While the determination of the incident field coefficients is often trivial, as in the case of a monochromatic plane wave, the calculation of scattered field coefficients is of a more difficult nature. The basic idea is to translate the expansion coefficients of all the scattered fields from their initial reference frame (attached to the respective sphere) to the $l$-th reference frame. This can be done with the aid of vector translation theorems, thus obtaining the following equation [17; 37]:

$$\begin{aligned} a^{jl}_{mn} &= \sum_{\nu=1}^{\infty} \sum_{\mu=-\nu}^{\nu} \left[ A^{jl}_{mn\mu\nu}\, a^j_{\mu\nu} + B^{jl}_{mn\mu\nu}\, b^j_{\mu\nu} \right] \\ b^{jl}_{mn} &= \sum_{\nu=1}^{\infty} \sum_{\mu=-\nu}^{\nu} \left[ B^{jl}_{mn\mu\nu}\, a^j_{\mu\nu} + A^{jl}_{mn\mu\nu}\, b^j_{\mu\nu} \right]. \end{aligned} \tag{1.12}$$

Here $(A^{jl}_{mn\mu\nu}, B^{jl}_{mn\mu\nu})$ are the well-know vector translation coefficients, which characterize the transformation of scattered waves from the $j$-th sphere into incident waves for the $l$-th sphere [38–42]. Relevant numerical aspects of the vector translation coefficient computation are reported in the appendix at the end of the chapter. Finally, the total incident field coefficients are given by [17]:

$$\begin{aligned} P^l_{mn} &= p^l_{mn} - \sum_{j\neq l}^{N_S} a^{jl}_{mn}, \\ Q^l_{mn} &= q^l_{mn} - \sum_{j\neq l}^{N_S} b^{jl}_{mn}, \end{aligned} \tag{1.13}$$

which, by substituting Eq.(1.12) in Eq.(1.13) becomes

$$\begin{aligned} P^l_{mn} &= p^l_{mn} - \sum_{j\neq l}^{N_S} \sum_{\nu=1}^{\infty} \sum_{\mu=-\nu}^{\nu} \left[ A^{jl}_{mn\mu\nu}\, a^j_{\mu\nu} + B^{jl}_{mn\mu\nu}\, b^j_{\mu\nu} \right] \\ Q^l_{mn} &= q^l_{mn} - \sum_{j\neq l}^{N_S} \sum_{\nu=1}^{\infty} \sum_{\mu=-\nu}^{\nu} \left[ B^{jl}_{mn\mu\nu}\, a^j_{\mu\nu} + A^{jl}_{mn\mu\nu}\, b^j_{\mu\nu} \right]. \end{aligned} \tag{1.14}$$

At last, with the substitution of Eq.(1.14) in Eq.(1.11), a large scale linear system whose unknowns are the scattering expansion coefficients is obtained

[17]:

$$a^l_{mn}/a^l_n = p^l_{mn} - \sum_{j\neq l}^{N_S}\sum_{\nu=1}^{\infty}\sum_{\mu=-\nu}^{\nu}\left[A^{jl}_{mn\mu\nu}\,a^j_{\mu\nu} + B^{jl}_{mn\mu\nu}\,b^j_{\mu\nu}\right],$$

$$b^l_{mn}/b^l_n = q^l_{mn} - \sum_{j\neq l}^{N_S}\sum_{\nu=1}^{\infty}\sum_{\mu=-\nu}^{\nu}\left[B^{jl}_{mn\mu\nu}\,a^j_{\mu\nu} + A^{jl}_{mn\mu\nu}\,b^j_{\mu\nu}\right]. \qquad (1.15)$$

Once that the solution of the system is found all the fields in the electromagnetic problem are known, since internal field coefficients may be easily computed when the scattering one are determined [17; 43–45].

### 1.2.3. Solution of the linear system

Interaction scattering coefficients as described in Eq.(1.15) are determined by three principal physical factors:

1. the physical properties of each single sphere, included in the Mie scattering coefficients;
2. the profile of the incident beam, described by the $(p^j_{mn}, q^j_{mn})$ coefficients;
3. the topological configuration of the cluster whose description is stored in the vector translation coefficients $(A^{jl}_{mn\mu\nu}, B^{jl}_{mn\mu\nu})$.

It is clear that in order to solve the linear system a truncation in the spherical wave expansion must be included, i.e. order $n$ now must range between 1 and $N_M$, where $N_M$ is the the highest order included multipole. As will be subsequently discussed, in the case of interacting spheres there is no analogue to the single sphere truncation criterion of Wiscombe, introduced to determine the highest order $N_M$ required for solution convergence [1].

Therefore computation of Mie coefficients $(a^j_n, b^j_n)$, incident wave coefficients $(p^j_{mn}, q^j_{mn})$ and vector translation coefficients $(A^{jl}_{mn\mu\nu}, B^{jl}_{mn\mu\nu})$ up to $N_M$ is performed for the system (1.15), leading to an ensemble of $2N_SN_M(N_M+2)$ equations, which may be conveniently written in matrix from. For large values of $N_S$ and $N_M$, which is often the case in practical calculations, direct inversion of the coefficient matrix is unfeasible, and thus iterative methods are adopted in order to solve the linear system. Nevertheless these methods are know to be mostly efficient in the case of sparse matrices, while the one obtained in our solution is a dense one. In order to overcome these difficulties an efficient numerical scheme was adopted [37], which is able to evade computation of vector translation coefficients in a general case by their decomposition in translational and rotational parts, and finally only requiring the computation of "diagonal" terms of the form $(A^{jl}_{mnm\nu}, B^{jl}_{mnm\nu})$. It will be shown that in the framework of this numerical scheme iterative methods prove to be much more performing than traditional ones for the solution of our linear problem. Among the wealth of different iterative techniques adopted to solve large scale linear systems, the so-called BiCGstab(ell) method developed by Sleijpen and Fokkema is used [46], since it is especially conceived to solve large linear system characterized by unsymmetrical matrices with complex spectrum.

### 1.2.4. Extinction, scattering and absorption cross sections of a set of spheres

With the interaction scattering and absorption coefficients solved, it is now possible to deduce expressions for the extinction, scattering and absorption properties of the sphere aggregate in terms of these coefficients. Expressions for the cross sections of the cluster will be obtained in a way similar to the one used in the case of an isolated sphere, i.e. by calculating the net rate at which electromagnetic energy crosses an imaginary surface enclosing the whole cluster. When the scattering coefficients are at hand, internal end external electromagnetic fields are known at every point in the space, and accordingly the time averaged Poynting vector $\mathbf{S}$, which can be written as

$$\mathbf{S} = \mathbf{S}_{\mathrm{inc},0} + \mathbf{S}_{\mathrm{sca}} + \mathbf{S}_{\mathrm{ext}} \tag{1.16}$$

where

$$\begin{aligned}
\mathbf{S}_{\mathrm{inc},0} &= \frac{1}{2}\mathrm{Re}(\mathbf{E}_{\mathrm{inc},0} \times \mathbf{H}^{*}_{\mathrm{inc},0}),\\
\mathbf{S}_{\mathrm{sca}} &= \frac{1}{2}\mathrm{Re}(\mathbf{E}_{\mathrm{sca}} \times \mathbf{H}^{*}_{\mathrm{sca}}),\\
\mathbf{S}_{\mathrm{ext}} &= \frac{1}{2}\mathrm{Re}(\mathbf{E}_{\mathrm{inc},0} \times \mathbf{H}^{*}_{\mathrm{sca}} + \mathbf{E}_{\mathrm{sca}} \times \mathbf{H}^{*}_{\mathrm{inc},0}),
\end{aligned} \tag{1.17}$$

and the superscript $^{*}$ stands for the complex conjugate. $\mathbf{S}_{\mathrm{inc},0}$ is the complex Poynting vector associated with the initial incident field and is independent of position in the case of a nonabsorbing medium along with a plane wave incident beam. $\mathbf{S}_{\mathrm{sca}}$ is the Poynting vector associated to the total scattered field while $\mathbf{S}_{\mathrm{ext}}$ may be interpreted as the term that arises form the interaction between the incident and the scattered waves.

If we denote $W_{\mathrm{abs}}$ as the rate at which energy is dissipated inside the spheres and $W_{\mathrm{sca}}$ the rate at which energy is scattered across a given surface $\Omega$ then $W_{\mathrm{ext}}$ is the sum of the two, and we may write

$$W_{\mathrm{ext}} = W_{\mathrm{abs}} + W_{\mathrm{sca}}, \tag{1.18}$$

provided that

$$\begin{aligned}
W_{\mathrm{ext}} &= -\frac{1}{2}\mathrm{Re}\int_{\Omega} \mathbf{S}_{\mathrm{ext}} \cdot \hat{\mathbf{e}}_r \,\mathrm{d}\Omega,\\
W_{\mathrm{sca}} &= -\frac{1}{2}\mathrm{Re}\int_{\Omega} \mathbf{S}_{\mathrm{sca}} \cdot \hat{\mathbf{e}}_r \,\mathrm{d}\Omega,
\end{aligned} \tag{1.19}$$

and $\Omega$ is the surface of an imaginary sphere that enclose all the scatterers. The expression (1.19) for $W_{\mathrm{ext}}$ can be conveniently rearranged by expressing the involved fields in spherical component form, thus obtaining

$$\begin{aligned}
&W_{\mathrm{ext}} =\\
&\frac{1}{2}\mathrm{Re}\int_{0}^{2\pi}\int_{0}^{\pi} (E^{\phi}_{\mathrm{inc},0} H^{\theta *}_{\mathrm{sca}} - E^{\theta}_{\mathrm{inc},0} H^{\phi *}_{\mathrm{sca}} - E^{\theta}_{\mathrm{sca}} H^{\phi *}_{\mathrm{inc},0} + E^{\phi}_{\mathrm{sca}} H^{\theta *}_{\mathrm{inc},0}) r^2 \sin\theta \,\mathrm{d}\theta \,\mathrm{d}\phi
\end{aligned} \tag{1.20}$$

where $r$, the radius of the imaginary sphere, is arbitrary. By substituting the series expansions derived from equation (1.2) in (1.20), and integrating the resulting products term by term, we obtain the expression for the cluster extinction rate in terms of the initial incident field and scattered field expansion coefficients [17]:

$$W_{\text{ext}} = \frac{2\pi|E_0|}{k\omega\mu_0} \sum_{l=1}^{N_S} \sum_{n=1}^{N_M} \sum_{m=-n}^{n} \text{Re}\left[a_{mn}^l p_{mn}^{l*} + b_{mn}^l q_{mn}^{l*}\right]. \tag{1.21}$$

The extinction cross section is computed by simply dividing the extinction rate $W_{\text{ext}}$ by the initial incindent irradiance

$$I_{\text{inc},0} = \frac{k|E_0|}{2\omega\mu_0}, \tag{1.22}$$

obtaining finally

$$C_{\text{ext}} = \frac{4\pi}{k^2} \sum_{l=1}^{N_S} \sum_{n=1}^{N_M} \sum_{m=-n}^{n} \text{Re}\left[a_{mn}^l p_{mn}^{l*} + b_{mn}^l q_{mn}^{l*}\right]. \tag{1.23}$$

The calculation of the total absorption cross section can be carried out in a similar fashion, by integrating the radiant energy absorbed by each sphere and then dividing by the initial incident irradiance[37]:

$$C_{\text{abs}} = -\frac{4\pi}{k^2} \sum_{l=1}^{N_S} \sum_{n=1}^{N_M} \sum_{m=-n}^{n} \left[D_n^l |a_{mn}^l|^2 + C_n^l |b_{mn}^l|^2\right]. \tag{1.24}$$

where

$$C_n^l = \frac{\text{Re}[im^l \psi_n(y^l)\psi_n'^*(y^l)]}{|\psi_n(y^l)\psi_n'(x^l) - m^l \psi_n(x^l)\psi_n'(y^l)|^2}$$

$$D_n^l = \frac{\text{Re}[im^l \psi_n(y^l)\psi_n'^*(y^l)]}{|m^l \psi_n(y^l)\psi_n'(x^l) - \psi_n(x^l)\psi_n'(y^l)|^2} \tag{1.25}$$

and $\psi_n$ is a Riccati-Bessel function defined as

$$\psi_n(\rho) = \rho j_n(\rho) \tag{1.26}$$

with $y^l = m^l x^l$ and the size parameter $x^l$ as arguments.

When $C_{\text{ext}}$ and $C_{\text{abs}}$ are known $C_{\text{sca}}$ can be simply determined by $C_{\text{sca}} = C_{\text{ext}} - C_{\text{abs}}$. Nevertheless an explicit expression for the scattering cross section may be needed; While the above approaches are able to provide such an expression, it has been shown that a calculations relying on the computation of scattering matrix elements offer advantages from the numerical point of view, avoiding the necessity to represent the total scattered field in a single reference frame [47]. Without entering in the details of the calculation, the expression for $C_{\text{sca}}$ that is finally obtained is [47]:

$$C_{\text{sca}} = \frac{4\pi}{k^2} \sum_{l=1}^{N_S} \sum_{n=1}^{N_M} \sum_{m=-n}^{n} \text{Re}\left[a_{mn}^{l*} a_{mn}^{(l)} + b_{mn}^{l*} b_{mn}^{(l)}\right], \tag{1.27}$$

where

$$a_{mn}^{(l)} = \sum_{\nu=1}^{N_M} \left[ \tilde{A}_{mn\mu\nu}^{jl} a_{\mu\nu}^{j} + \tilde{B}_{mn\mu\nu}^{jl} b_{\mu\nu}^{j} \right],$$
$$b_{mn}^{(l)} = \sum_{\nu=1}^{N_M} \left[ \tilde{B}_{mn\mu\nu}^{jl} a_{\mu\nu}^{j} + \tilde{A}_{mn\mu\nu}^{jl} b_{\mu\nu}^{j} \right], \tag{1.28}$$

with $\tilde{A}_{mn\mu\nu}^{ll} = \delta_{m\mu}\delta_{n\nu}$ and $\tilde{B}_{mn\mu\nu}^{ll} \equiv 0$. $\tilde{A}_{mn\mu\nu}^{jl}$ and $\tilde{B}_{mn\mu\nu}^{jl}$ are equal to the traditional vector translation coefficients with the exception of the spherical Bessel function employed for their calculation: $j_n$ is used for $\tilde{A}$ and $\tilde{B}$ while $h_n^{(1)}$ is adopted in the case of the original vector translation coefficients.

As a final remark we notice that the independent computation of all the cross sections is a useful tool in order to check the numerical accuracy of the obtained solutions.

## 1.3. Appendix: relevant numerical aspects of GMM theory

With the vector translation theorems at hand the derivation of the multisphere problem solution is relatively straightforward. Nevertheless some aspects of the theory exist that must be discussed in detail, in order to successfully implement the GMM approach in a working code. They are mostly numerical problems concerning the efficient and reliable computation of some special functions, or the efficient solution of the large scale linear system obtained from the application of the vector translation theorems. The main problems to tackle are:

- Computation of traditional Mie coefficients ($a_n^l, b_n^l$): Wiscombe criterion allows to safely and efficiently calculate the scattering coefficients in the case of the isolated sphere [1]. Since this criterion does not hold true in the GMM approach, a method must be devised in order to compute high order scattering coefficients even when the cluster is composed by small spheres, i.e. when a simple dipolar approach would be sufficient if the spheres were isolated. A scheme for a stable computation of Riccati-Bessel functions is therefore necessary [1; 48];

- Computation of vector translation coefficients ($A_{mn\mu\nu}^{jl}, B_{mn\mu\nu}^{jl}$): in order to solve the GMM problem a large number of vector translation coefficients needs to be evaluated. This in turn implies the calculation of a wide spectrum of special functions, including associated Legendre polynomials, spherical Bessel and Riccati-Bessel functions [42; 44; 45] and Gaunt coefficients [41];

- Matrix Vector Multiplication in BiCGstab(ell): the most time consuming task in the resolution of the GMM linear system is the multiplication of the coefficient matrix by the vector of the unknowns, required in the adopted iterative method; it is advisable to carry on this multiplication

in the rotation-translation-rotation framework described by Mackowski [37], requiring thus the additional computation of reduced rotation matrix element;

- Local-field computation: electromagnetic fields as described in Eq.(1.5) are cast in a form which is in most cases unsuitable for numerical calculation, especially in the case of internal fields. Therefore electric fields, which are the ones of interest in the present case, need to be rewritten in a form which is appropriate for numerical computation. Reliable evaluation of $\tau_{mn}$, $\pi_{mn}$, spherical Bessel and Riccati-Bessel functions is needed.

We first report numerical details for the computation of all the involved special functions, and in a second time the explicit expressions of the dependent quantities such as classical Mie or vector translation coefficients.

### 1.3.1. Computation of radial functions: spherical Bessel and Riccati-Bessel functions

Spherical Bessel functions $j_n(\rho)$, $y_n(\rho)$ and $h_n^{(1)}(\rho) = j_n(\rho) + iy_n(\rho)$ are best evaluated via the recurrence relation

$$z_n(\rho) = \frac{2n-1}{\rho} z_{n-1}(\rho) - z_{n-2}, \tag{1.29}$$

where $z_n$ is either $j_n$ or $y_n$ and of course $h_n^{(1)}$ comes from a combination of the former two. Riccati-Bessel functions are defined as

$$\begin{aligned} \psi_n(\rho) &= \rho\, j_n(\rho) \\ \chi_n(\rho) &= -\rho\, y_n(\rho) \\ \xi_n(\rho) &= \rho\,(j_n(\rho) + iy_n(\rho)) = \psi_n(\rho) - i\chi_n(\rho) \end{aligned} \tag{1.30}$$

and their computation, along with the additional function $\eta_n(\rho) = j_n(\rho)/\rho$ is based on Eq.(1.29). Calculation of $y_n(\rho)$ and $\chi_n(\rho)$ is required only for real argument, and is relatively straightforward since in this case recurrence relation (1.29) is stable in the upward direction. Therefore only the two starting values are needed

$$\begin{aligned} y_0(\rho) &= -\frac{\cos\rho}{\rho}, \quad y_1(\rho) = -\frac{\cos\rho}{\rho^2} - \frac{\sin\rho}{\rho}, \\ \chi_0(\rho) &= \cos\rho, \quad \chi_1(\rho) = \frac{\cos\rho}{\rho} + \sin\rho, \end{aligned} \tag{1.31}$$

and the evaluation is performed without incurring in any additional roundoff error.

Computation of $\eta_n(\rho)$, $j_n(\rho)$ and $\psi_n(\rho)$ is of a more difficult nature since it must be done for both real and complex arguments, it is unstable against recurrence (1.29) in the upward direction and functions are subject to overflow when their argument is complex and has a large imaginary part [44; 45]. Functions

$\eta_n(\rho)$, $j_n(\rho)$ and $\psi_n(\rho)$ monotonically decrease as index $n$ increases, therefore the relation (1.29) is unstable in the upward direction because, whenever $\eta_n(\rho)$, $j_n(\rho)$ or $\psi_n(\rho)$ become an order of magnitude smaller, a significative digit is lost. It is possible, with the aid of Kapteyn inequality [48], to estimate the orders of magnitude between the moduli of $j_0(\rho)$ and $j_n(\rho)$ (and therefore of the other two functions), obtaining the expression

$$l_n(\rho) = \frac{\left\{|\mathrm{Im}(\rho)| - \ln 2 - n\left[\mathrm{Re}\left(\ln\left(\frac{\rho}{n}\right) + \left[1 - \left(\frac{\rho}{n}\right)^2\right]^{1/2} - \ln\left\{1 + \left[1 - \left(\frac{\rho}{n}\right)^2\right]^{1/2}\right\}\right)\right]\right\}}{\ln 10}. \tag{1.32}$$

which is approximately also the number of significative digits lost in the upward recurrence or gained in the downward one. In order to overcome stability and overflow problems a ratio of Bessel functions which is always well behaved is introduced [48]

$$r_n(\rho) = \frac{j_{n-1}(\rho)}{j_n(\rho)} = \frac{\psi_{n-1}(\rho)}{\psi_n(\rho)}, \tag{1.33}$$

and its evaluation is done in the downward direction, so exploiting the inherited stability properties of the parent functions. It is easy to show that the recurrence relation can be initiated with $r_{N^*}(\rho) = (2N^* + 1)/\rho$ [48], where $N^*$ is larger than the higher order $N_M$ required in the computation. $N^*$ is chosen with the aid of expression (1.32) so as to obtain all the required significative digits when downward recurrence reaches the highest needed order $N_M$. Finally, when needed, $\eta_n(\rho)$, $j_n(\rho)$ and $\psi_n(\rho)$ may be computed by the recurrence relations

$$\eta_n(\rho) = \eta_{n-1}(\rho)/r_n(\rho), \quad j_n(\rho) = j_{n-1}(\rho)/r_n(\rho), \quad \psi_n(\rho) = \psi_{n-1}(\rho)/r_n(\rho), \tag{1.34}$$

with

$$\eta_1(\rho) = \frac{\sin\rho}{\rho^3} - \frac{\cos\rho}{\rho^2}, \quad j_0(\rho) = \frac{\sin\rho}{\rho}, \quad \psi_0 = \sin\rho, \tag{1.35}$$

as starting values.

### 1.3.2. Computation of angular functions: $\tau_{mn}$, $\pi_{mn}$, associated Legendre polynomials and rotation matrix elements

Angular functions employed in GMM theory do not present any particular problem from the point of view of numerical computation, and are always real valued. Nevertheless reliable recurrence schemes help to speed up the solution of the electromagnetic problem. Associated Legendre polynomials $P_n^m(\cos\theta)$, which are here adopted without the $(-1)^m$ modulus convention accordingly to the theoretical framework of Xu[17], are efficiently computed by the stable upward recurrence relation

$$(n-m)P_n^m(\cos\theta) = \cos\theta\,(2n-1)P_{n-1}^m(\cos\theta) - (n+m-1)P_{n-2}^m(\cos\theta), \tag{1.36}$$

where the starting values are

$$P_m^m(\cos\theta) = (-1)^m(2m-1)!!|\sin\theta|^m,$$

$$P_{m+1}^m(\cos\theta) = \cos\theta\,(2m+1)P_m^m(\cos\theta), \tag{1.37}$$

and the double exclamation mark stands for a double factorial. Values for negative $m$ are finally defined by

$$P_n^{-m}(\cos\theta) = (-1)^m\frac{(n-m)!}{(n+m)!}P_n^m(\cos\theta). \tag{1.38}$$

Angular functions $\tau_{mn}(\cos\theta)$ and $\pi_{mn}(\cos\theta)$ as defined in (1.4), are evaluated through an upward recurrence scheme, which is similar to the one adopted for the associated Legendre functions, as it might be expected. We first proceed to the computation of $\pi_{mn}(\cos\theta)$ and then $\tau_{mn}(\cos\theta)$ will be consequently calculated. The main recurrence relation for $\pi_{mn}(\cos\theta)$ may be written as

$$(n-m)\pi_{mn}(\cos\theta) = \cos\theta\,(2n-1)\pi_{m(n-1)}(\cos\theta) - (n+m-1)\pi_{m(n-2)}(\cos\theta), \tag{1.39}$$

where the starting values are

$$\pi_{mm}(\cos\theta) = m\,(2m-1)!!(\sin\theta)^{m-1},$$

$$\pi_{m(m-1)}(\cos\theta) = \cos\theta\,(2m+1)\pi_{mm}(\cos\theta), \tag{1.40}$$

and values for negative $m$ are found by

$$\pi_{-mn}(\cos\theta) = (-1)^{m+1}\frac{(n-m)!}{(n+m)!}\pi_{mn}(\cos\theta). \tag{1.41}$$

Finally, for some special values of the argument, i.e. when $\theta = 0, \pi$, $\pi_{mn}(\cos\theta)$ assumes the following simplified values:

$$\pi_{mn}(0,\pi) = \begin{cases} (\pm)^{n+1}\left(\frac{1}{2}\right) & \text{if} \quad m=-1, \\ (\pm)^{n+1}\left(\frac{n(n+1)}{2}\right) & \text{if} \quad m=1, \\ 0 & \text{otherwise.} \end{cases} \tag{1.42}$$

Function $\tau_{mn}(\cos\theta)$ is derived from $\pi_{mn}(\cos\theta)$ by the relations

$$m\,\tau_{mn}(\cos\theta) = n\cos\theta\,\pi_{mn}(\cos\theta) - (n+m)\pi_{m(n-1)}(\cos\theta), \qquad m \neq 0, \tag{1.43}$$

and, for the special case $m = 0$,

$$\tau_{0n}(\cos\theta) = \frac{2n-1}{n-1}\cos\theta\,\tau_{0(n-1)}(\cos\theta) - \frac{n-1}{n}\cos\theta\,\tau_{0(n-2)}(\cos\theta), \tag{1.44}$$

where the starting values are

$$\tau_{00} = 0, \qquad \tau_{01} = \sin\theta. \tag{1.45}$$

Finally expressions for negative $m$ and special values of the argument are

$$\tau_{-mn}(\cos\theta) = (-1)^m \frac{(n-m)!}{(n+m)!}\tau_{mn}(\cos\theta), \tag{1.46}$$

and

$$\tau_{mn}(0,\pi) = \begin{cases} -(\pm)^n \left(\frac{1}{2}\right) & \text{if} \quad m=-1, \\ (\pm)^n \left(\frac{n(n+1)}{2}\right) & \text{if} \quad m=1, \\ 0 & \text{otherwise.} \end{cases} \tag{1.47}$$

Reduced rotation matrix elements $d_{mk}^{(n)}$ are special angular functions employed in the solution of the large scale linear system arising from the GMM electromagnetic problem, and are thoroughly described in Ref.[49]. Their evaluation is performed through the standard upward recurrence scheme

$$c^0 d_{mk}^{(n)} = c_1 d_{mk}^{(n-1)} - c_2 d_{mk}^{(n-2)}, \tag{1.48}$$

where

$$\begin{aligned} c_0 &= (n-1)\sqrt{n^2-m^2}\sqrt{n^2-k_2}, \\ c_1 &= (2n-1)(n(n-1)-\cos\beta - mk), \\ c_2 &= n\sqrt{(n-1)^2-m^2}\sqrt{(n-1)^2-k^2}, \end{aligned} \tag{1.49}$$

with $\beta$ coming from the rotation of the coordinate system described by the Euler angles $(\alpha, \beta, \gamma)$. Recurrence relation begins with the single starting value

$$\begin{aligned} &d_{mk}^{(n_{\min})} = \\ &(-1)^{m+k}\, e_{mk}\, 2^{-n_{\min}} \left(\frac{(2n_{\min})!}{|m-k|!\,|m+k|!}\right)^{1/2} (1-\cos\beta)^{\frac{|m-k|}{2}} (1+\cos\beta)^{\frac{|m+k|}{2}}, \end{aligned} \tag{1.50}$$

where

$$n_{\min} = \mathrm{Max}(|m|,\, |k|),$$

$$e_{mk} = \begin{cases} 1 & \text{if} \quad k \geq m \\ (-1)^{m-k} & \text{otherwise.} \end{cases} \tag{1.51}$$

The $m = k = 0$ case is handled with the special recurrence relation

$$d_{00}^{(n)} = (2n-1)\cos\beta\, d_{00}^{(n-1)} - \frac{n-1}{n} d_{00}^{(n-2)}, \tag{1.52}$$

with the two starting values

$$\begin{aligned} d_{00}^{(0)} &= 1, \\ d_{00}^{(1)} &= \cos\beta. \end{aligned} \tag{1.53}$$

### 1.3.3. Computation of Gaunt coefficients

A rapid evaluation of vector translation coefficients $A_{mn\mu\nu}$ and $B_{mn\mu\nu}$ relies on an expeditious computation of Gaunt coefficients, which are defined by

$$a(m,n,\mu,\nu,p) = \frac{2p+1}{2}\frac{(p-m-\mu)!}{(p+m+\mu)!}\int_{-1}^{1} P_n^m(x)\,P_\nu^\mu(x)\,P_p^{m+\mu}(x)\,\mathrm{d}x, \quad (1.54)$$

or alternatively as

$$P_n^m(x)\,P_\nu^\mu(x) = \sum_{q=0}^{q_{\max}} a_q P_q^{m+\mu}(x), \quad (1.55)$$

where $p = n+\nu-2q$, $a_q = a(m,n,\mu,\nu,p)$ and

$$q_{\max} = min\left[m, \nu, \frac{n+\nu-|m+\mu|}{2}\right]. \quad (1.56)$$

As for the other special functions involved in the GMM theory, Gaunt coefficients are most efficiently computed by mean of recurrence relations, i.e. [41; 42]

$$c_0 a_q = c_1 a_{q-1} + c_2 a_{q-2}, \quad (1.57)$$

where

$$\begin{aligned} c_0 =&(p+2)(p+3)(p_1+1)(p_1+2)A_{p+4}\alpha_{p+1},\\ c_1 =&A_{p+2}A_{p+3}A_{p+4} + (p+1)(p+3)(p_1+2)(p_2+2)A_{p+4}\alpha_{p+2},\\ &+(p+2)(p+4)(p_1+3)(p_2+3)A_{p+2}\alpha_{p+3},\\ c_2 =&-(p+2)(p+3)(p_2+3)(p_2+4)A_{p+2}\alpha_{p+4}, \end{aligned} \quad (1.58)$$

and

$$\begin{aligned} A_p &= -p(p-1)(\mu-m) - (\mu+m)(n-\nu)(n+\nu+1),\\ p_1 &= p-m-\mu,\\ p_2 &= p+m+\mu,\\ \alpha_p &= \frac{\left[p^2-(n-\nu)^2\right]\left[p^2-(n+\nu+1)^2\right]}{4p^2-1}. \end{aligned} \quad (1.59)$$

For the special case $\mu = m$ and $\nu = n$ $A_p$ vanishes independently of $p$ and the three term recurrence relation (1.57) is reduced to

$$(p+2)(p_1+1)\alpha_{p+1}a_q = (p+1)(p_2+2)\alpha_{p+2}a_{q-1}, \quad (1.60)$$

and in particular for $\mu = m = 0$ we have

$$\alpha_{p+1}a_q = \alpha_{p+2}a_{q-1}. \quad (1.61)$$

The case of $A_{p+4} = 0$ but $A_{p+4} \neq 0$ requires a different handling and the introduction of a four term recurrence relation:

$$c_0 a_q = c_1 a_{q-1} + c_2 a_{q-2} + c_3 a_{q-3}, \quad (1.62)$$

where

$$\begin{aligned}
c_0 =&(p+2)(p+3)(p+5)(p_1+1)(p_1+2)(p_1+4)A_{p+6}\alpha_{p+1}\\
c_1 =&(p+5)(p_1+4)A_{p+6}[A_{p+2}A_{p+3}+(p+1)(p+3)(p_1+2)(p_2+2)]\alpha_{p+2}\\
c_2 =&(p+2)(p_2+3)A_{p+2}[A_{p+5}A_{p+6}+(p+4)(p+6)(p_1+5)(p_2+5)]\alpha_{p+5}\\
c_3 =&-(p+2)(p+4)(p+5)(p_2+3)(p_2+5)(p_2+6)A_{p+2}\alpha_{p+6}.
\end{aligned} \tag{1.63}$$

These recursive schemes are adopted in either upward and downward direction in order to increase the numerical accuracy of the computation, with only one coefficient $a_{q_{\max}}$ or $a_0$ needed to start the recurrence, since coefficients outside the allowed range are set to be zero [38; 41].

Finally we note that in the numerical framework proposed by Mackowski only coefficients of the form $A_{mnm\nu}$ and $B_{mnm\nu}$ need to be computed, thus allowing the adoption of the following three terms recurrence relation [41]:

$$\alpha_{p+1}a_q-(4m^2+\alpha_{p+2}+\alpha_{p+3})a_{q-1}+\alpha_{p+4}a_{q-2}=0. \tag{1.64}$$

### 1.3.4. Computation of classical Mie coefficients

Since the work of Wiscombe, computation of Mie scattering coefficients is a well known and established matter [1]. While the recursive computation of Riccati-Bessel functions $\psi_n$ is known to be unstable in the upward direction, only a few significative digits are lost if the truncation criterion

$$N_M=x+4x^{1/3}+2 \tag{1.65}$$

is applied and the expansion is stopped at the $N_M$ multipole, where $x$ is the size parameter. Nevertheless in multisphere calculations the above criterion is no more valid, and a large number of multipole might be necessary even if a quasi-static approximation is applied [50].

Numerical techniques devised in Sec.(1.3.1) are able to overcome these computational problem. Once that classical Mie coefficients are recast in the form

$$\begin{aligned}
a_n^l &= \frac{\left[r_n(m^lx^l)/m^l+n(1-(m^l)^{-2})/x^l\right]\psi_n(x^l)-\psi_{n-1}(x^l)}{\left[r_n(m^lx^l)/m^l+n(1-(m^l)^{-2})/x^l\right]\xi_n(x^l)-\xi_{n-1}(x^l)},\\
b_n^l &= \frac{r_n(m^lx^l)m^l\psi_n(x^l)-\psi_{n-1}(x^l)}{r_n(m^lx^l)m^l\xi_n(x^l)-\xi_{n-1}(x^l)},
\end{aligned} \tag{1.66}$$

where $r_n$ is as in (1.33), the computation is straightforward.

### 1.3.5. Computation of vector translation coefficients

Vector translation coefficients as formulated in Ref.[42] may be expressed in term of Gaunt coefficients:

$$\begin{aligned}
A_{mn\mu\nu}^{jl} &= C_0e^{i(\mu-m)\phi^{jl}}\sum_{q=0}^{q_{\max}}i^pC_pa_qh_p^{(1)}(kd^{jl})P_p^{\mu-m}(\cos\theta^{jl}),\\
B_{mn\mu\nu}^{jl} &= C_0e^{i(\mu-m)\phi^{jl}}\sum_{q=1}^{Q_{\max}}i^{p+1}b_qh_{p+1}^{(1)}(kd^{jl})P_{p+1}^{\mu-m}(\cos\theta^{jl}),
\end{aligned} \tag{1.67}$$

where

$$
\begin{aligned}
Q_{\max} &= \mathrm{Min}\left[n, \nu, \frac{n+\nu+1-|\mu-m|}{2}\right], \\
C_0 &= \frac{(-1)^m}{2}\left[\frac{(2n+1)(2\nu+1)(n+m)!(\nu-\mu)!}{n(n+1)\nu(\nu+1)(n-m)!(\nu+\mu)!}\right]^{1/2}, \\
C_p &= n(n+1)+\nu(\nu+1)-p(p+1),
\end{aligned}
\tag{1.68}
$$

and $a_q = a(-m, n, \mu, \nu, q)$. Therefore index $m$ must me substituted with $-m$ in all the expressions (1.56) and (1.59). Here $(d^{jl}, \theta^{jl}, \phi^{jl})$ are the spherical coordinates of the origin of the $l$-th coordinate system (i.e. the $l$-th sphere center) in the $j$-th coordinate system, and

$$
\begin{aligned}
b_q =& \frac{2p+3}{A_{p+2}}[(p+2)(p_1+1)\alpha_{p+1}a_q - (p+1)(p_2+2)\alpha_{p+2}a_{q-1}], \qquad A_{p+2} \neq 0 \\
b_q =& \frac{2p+3}{(p+3)(p_1+2)A_{p+4}} \\
& \{[A_{p+3}A_{p+4} + (p+2)(p+4)(p_1+3)(p_2+3)\alpha_{p+3}]a_{q-1} \qquad A_{p+2} = 0 \\
& - (p+2)(p+3)(p_2+3)(p_2+4)\alpha_{p+4}a_{q-2}\}.
\end{aligned}
\tag{1.69}
$$

When $A_{p+2} = A_{p+4} = 0$, i.e. $A_p$ vanishes independently of the value of $p$, $B^{jl}_{mn\mu\nu} = 0$. This includes the cases: (i) $\mu = m = 0$ and (ii) $\mu = -m$ and $\nu = n$. In addition $B^{jl}_{mn\mu\nu} = 0$ when (i) $m = n$ and $\mu = -\nu$ and (ii) $m = -n$ and $\mu = \nu$.

Of course recursive relation of section (1.3.3) are of central importance and widely used in the computation of vector translation coefficients. As mentioned before Mackowski introduced a very efficient numerical scheme for translating multipole expansions between displaced coordinate systems [37]. Its rotation-translation-rotation technique performs the computation of general translation coefficients by decomposition in translational and rotational parts. The procedure is applied in such a way that translations are only carried along the $z$ axis of the reference system. In this peculiar case translation coefficients $A^{jl}_{mn\mu\nu}$ and $B^{jl}_{mn\mu\nu}$ exists only if $m = \mu$ and for $\cos\theta^{jl} = 1$ take the rather simple form

$$
\begin{aligned}
A^{jl}_{mnm\nu} &= C_0 \sum_{q=0}^{\min(n,\nu)} i^p C_p a_q h^{(1)}_p(kd^{jl}), \\
B^{jl}_{mnm\nu} &= C_0 \sum_{q=1}^{\min(n,\nu)} i^{p+1} b_q h^{(1)}_{p+1}(kd^{jl}).
\end{aligned}
\tag{1.70}
$$

### 1.3.6. Matrix vector multiplication

As already stated the large scale linear system which arises from the solution of GMM problem may be conveniently recast in matrix form. Given that for an ensemble of $N_S$ spheres there will be $N_S(N_S-1)$ pair of interactions, and that $N_M^2$ interaction scattering coefficients are needed to describe the electromagnetic fields [37], the number of computed matrix elements will be of the order

of $O(N_S^2 N_M^4)$, where the elements are represented as double complex numbers in practical calculations. It is clear that when the number of spheres $N_S$ in the cluster is high and high order multipoles $N_M$ are included, the computational burned may become considerable. Mackowski computational approach allows to factor the original dense matrix in a product of three sparse matrices, by exploiting the symmetry properties of vector translation coefficients in the case of purely axial translations (1.70). In fact the general translation is performed as sequence of rotations and axial translations, which ends up in the matrix factorization addressed above, implying the computation of $O(N_S^2 N_M^3)$ terms.

Iterative approaches to the numerical solution of a linear system are particularly appealing when sparse matrices are involved, which is now our case. Therefore BiCGstab(ell) method, which is conceived for the solution of complex unsymmetrical systems, is employed [46]. The linear solver is independent of the data structure used to store the matrix coefficients as far as routines for matrix-vector multiplication and preconditioning are provided.

The multiplication between the coefficient matrix and the vector of the unknowns is the most computationally intensive task. Without the Mackowski formalism $O(N_S^2 N_M^4)$ operations are required [17]:

$$a_{mn}^{jl} = \sum_{\nu=1}^{N_M} \sum_{\mu=-\nu}^{\nu} (A_{mn\mu\nu}^{jl}\, a_{\mu\nu}^{j} + B_{mn\mu\nu}^{jl}\, b_{\mu\nu}^{j}),$$

$$b_{mn}^{jl} = \sum_{\nu=1}^{N_M} \sum_{\mu=-\nu}^{\nu} (B_{mn\mu\nu}^{jl}\, a_{\mu\nu}^{j} + A_{mn\mu\nu}^{jl}\, b_{\mu\nu}^{j}), \tag{1.71}$$

where $j$ runs from 1 to $N_M$ with $j \neq l$. However, through a rotation of coordinates, the numerical advantages of a common axis can be exploited. Finally a transformation from $j$ to $l$ like the one in (1.71) can be accomplished in three steps:

1. The coordinate system of $j$ is rotated so as its $z$-axis points towards the origin of $l$. The Euler angles for the rotation are $\alpha = \phi^{jl}$, $\beta = \theta^{jl}$ and $\gamma = 0$, and the transformation yields:

$$a_{mn}^{j\prime} = \sum_{k=-n}^{n} e^{ik\phi^{jl}}\, d_{km}^{(n)} a_{kn}^{j},$$

$$b_{mn}^{j\prime} = \sum_{k=-n}^{n} e^{ik\phi^{jl}}\, d_{km}^{(n)} b_{kn}^{j}. \tag{1.72}$$

2. The rotated coefficients at $j$ are the axially translated at $l$. This procedure involves only vector translation coefficients of the form $A_{mnm\nu}^{jl}$ and

$B^{jl}_{mnm\nu}$:

$$a^{jl\prime}_{mn} = \sum_{\nu=1}^{N_M} (A^{jl}_{mnm\nu} a^{j\prime}_{m\nu} + B^{jl}_{mnm\nu} b^{j\prime}_{m\nu}),$$

$$b^{jl\prime}_{mn} = \sum_{\nu=1}^{N_M} (B^{jl}_{mnm\nu} a^{j\prime}_{m\nu} + A^{jl}_{mnm\nu} b^{j\prime}_{m\nu}). \tag{1.73}$$

3. The coefficients are rotated back to the original orientation. Euler angles now are $\alpha = \pi$, $\beta = \theta^{jl}$ and $\gamma = \pi - \phi^{jl}$ with the final transformation taking the form:

$$a^{jl}_{mn} = (-1)^m \, e^{im\phi^{jl}} \sum_{k=-n}^{n} (-1)^k \, d^{(n)}_{km} a^{jl\prime}_{kn},$$

$$b^{jl}_{mn} = (-1)^m \, e^{im\phi^{jl}} \sum_{k=-n}^{n} (-1)^k \, d^{(n)}_{km} b^{jl\prime}_{kn}. \tag{1.74}$$

Here ($r^{jl}$,$\theta^{jl}$,$\phi^{jl}$) are the spherical coordinates of the origin of the $l$-th coordinate system in the $j$-th coordinate system. We finally note that each of the three steps involve $O(N_M^3)$ operations and therefore a considerable computational advantage is obtained from the application of this scheme, especially when high order multipole are included in the modeling.

### 1.3.7. Computation of local field

Computation of internal local-field. i.e computation of the electric field internal to the $l$-th sphere, is a trivial matter when $c^l_{mn}$ and $d^l_{mn}$ coefficients are know and computational issues of spherical Bessel functions are solved. $\mathbf{E}^l_{\text{int}}$ is computed in the the reference frame of the $l$-th sphere an its componet are expressed in polar spherical coordinates

$$E^{r,l}_{\text{int}} = \sum_{n=1}^{N_M} \sum_{m=-n}^{n} -i \, E_{mn} \, n(n+1) \, d^l_{mn} \, P^m_n \, \eta_n \, e^{im\phi^l}$$

$$E^{\theta,l}_{\text{int}} = \sum_{n=1}^{N_M} \sum_{m=-n}^{n} E_{mn}(-i \, d^l_{mn} \, (q_n - n) \, \tau_{mn} + \rho^l \, c^l_{mn} \, \pi^l_{mn}) \, \eta_n \, e^{im\phi^l}$$

$$E^{\phi,l}_{\text{int}} = \sum_{n=1}^{N_M} \sum_{m=-n}^{n} E_{mn}(i \, \rho^l \, c^l_{mn} \, \tau_{mn} + d^l_{mn} \, (q_n - n) \, \pi_{mn}) \, \eta_n \, e^{im\phi^l} \tag{1.75}$$

where the argument of $q_n$ and $\eta_n$ is $\rho^l = k^l r^l$ and $q_n = \rho^l r_n(\rho^l)$.

The computation of the total scattered field is a more difficult task, since the total field consists in the superposition of all the field scattered by each sphere. Individual scattered fields are represented in the respective reference frame, when in order to perform the overall evaluation a unitary description is needed. A viable solution is to obtain a single field representation by re-expanding all the fields in a common reference frame, with the aid of vector translation theorems. This allows to obtain the following expression for the total scattered field

$$\mathbf{E}_{\text{sca}} = i \sum_{n=1}^{N} \sum_{m=-n}^{n} E_{mn} [a_{mn} \mathbf{N}_{mn}^{(3)}(\rho, \theta, \phi) + b_{mn} \mathbf{M}_{mn}^{(3)}(\rho, \theta, \phi)]. \tag{1.76}$$

Nevertheless this kind of approach is problematic from the numerical point of view, and therefore is not adopted here [43].

The following sequential procedure, proposed by Quinten [14], is used for the computation of the total scattered field:

1. A point $\mathbf{r} = (x, y, z)$ is chosen in the common cluster reference frame;
2. The point $\mathbf{r}$ is translated in the reference frame of the $l$-th sphere, first in Cartesian components, as $\mathbf{r}^l = (x^l, y^l, z^l)$, and then in local polar spherical coordinates as $\mathbf{r}^l = (r^l, \theta^l, \phi^l)$;
3. $\mathbf{E}_{\text{sca}}^l$ components are evaluated in local spherical coordinates as $(E_{\text{sca}}^{r,l}, E_{\text{sca}}^{\theta,l}, E_{\text{sca}}^{\phi,l})$ and then converted in Cartesian coordinates $(E_{\text{sca}}^{x,l}, E_{\text{sca}}^{y,l}, E_{\text{sca}}^{z,l})$;
4. Procedure from point 1 to 3 is repeated for all the spheres in the cluster, and the total scattered field at the common point $\mathbf{r} = (x, y, z)$ is obtained as a sum of the fields computed at the third step of the procedure.

The above strategy is applied for all the $\mathbf{r}$ point where the computation of the local field is required. The field scattered from the $l$-th sphere, in local spherical coordinates, is written as

$$E_{\text{sca}}^{r,l} = \sum_{n=1}^{N_M} \sum_{m=-n}^{n} i\, E_{mn}\, n(n+1)\, a_{mn}^l\, P_n^m\, \frac{h_n^{(1)}}{\rho}\, e^{im\phi^l}$$

$$E_{\text{sca}}^{\theta,l} = \sum_{n=1}^{N_M} \sum_{m=-n}^{n} E_{mn}\, (i\, a_{mn}^l\, \tau_{mn}\, \frac{\mathrm{d}h_n^{(1)}}{\mathrm{d}\rho} - b_{mn}^l\, \pi_{mn}\, h_n^{(1)}) e^{im\phi^l}$$

$$E_{\text{sca}}^{\phi,l} = -\sum_{n=1}^{N_M} \sum_{m=-n}^{n} E_{mn} (a_{mn}^l\, \pi_{mn}\, \frac{\mathrm{d}h_n^{(1)}}{\mathrm{d}\rho^l} + b_{mn}^l\, \tau_{mn}\, h_n^{(1)}) e^{im\phi^l} \tag{1.77}$$

where

$$\frac{\mathrm{d}h_n^{(1)}}{\mathrm{d}\rho} = h_{n-1}^{(1)} - n\frac{h_n^{(1)}}{\rho} \tag{1.78}$$

and $\rho = kr^l$. Conversion from local spherical to local Cartesian representation, for both internal and scattered fields, is finally performed by

$$\begin{aligned} E_x^l &= E_r^l \sin\theta^l \cos\phi^l + E_\theta^l \cos\theta^l \cos\phi^l - E_\phi^l \sin\phi^l \\ E_y^l &= E_r^l \sin\theta^l \sin\phi^l + E_\theta^l \cos\theta^l \sin\phi^l - E_\phi^l \cos\phi^l \\ E_x^l &= E_r^l \cos\theta^l - E_\theta^l \sin\theta^l \end{aligned} \tag{1.79}$$

As a final remark we note that, when needed, initial incident field can be computed in a similar fashion.

# 2. Generalized Multiparticle Mie: far-field

## 2.1. Introduction

Generalized Multiparticle Mie theory offers a natural theoretical framework when optical properties of sphere ensembles are to be modeled, and even if less general than many other approaches such as MMP or FDTD methods [28; 35], many plasmonic structures of great practical and theoretical interest may be successfully investigated. In our case a Fortran code was implemented from scratch, following the guidelines given by Xu [17; 41; 42]; this software is now applied to the analysis of basic sphere ensembles which, though apparently simple, unveil fundamental physical aspects of these coupled systems. As a natural consequence these kind of studies allow the understanding of more complex interacting structures which will be tackled in the following chapters. As a first step we proceed to the far-field property modeling of the structures enumerated below:

- Nanoparticle dimers: extinction properties of nanoparticle dimers are investigated as a function of included multipole orders $N_M$, interparticle gap $g$, incident light polarization state and composition;
- Nanoparticle linear chains: extinction properties of nanoparticle linear chains are investigated as a function of interparticle spacing, chain length and composition. Particular attention is given to the role of metal $d$ electrons in determining the plasmonic properties of a given material;
- Nanoparticle linear chains supporting photonic-plasmonic modes: Extinction properties of long ($N_S = 500$) nanoparticle chains supporting collective photonic modes are investigated as a possibly interesting system to be applied in active plasmonic devices (see Ch.8) [5; 51].

We remark that the extinction properties of the above described structures are well described in literature, so as to additionally provide a good benchmark for the reliability and accuracy of our GMM theory implementation.

## 2.2. Extinction properties of nanoparticle dimers

Nanoparticle dimers are known for their peculiar far- and local-field properties, which strongly depend on the interparticle gap and on the polarization state of the incident field $\mathbf{E}_{\mathrm{inc},0}$ [52]. Moreover it has been observed that high multipolar orders have to be included in order to bring extinction spectra to

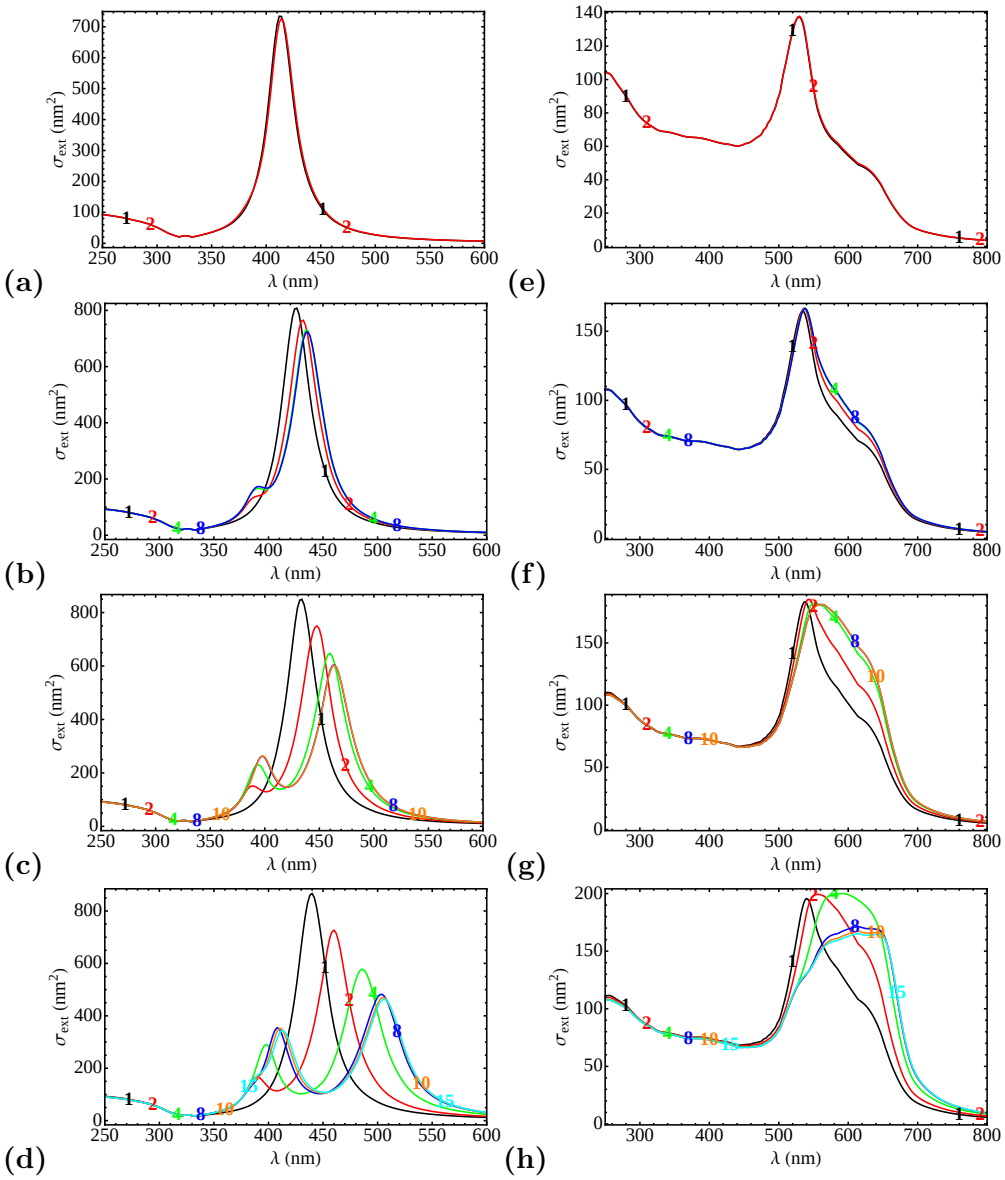


Figure 2.1.: Multipole dependence of optical extinction spectra for Ag and Au $D = 10$ nm dimers with varying interparticle spacings.(a) to (d): silver dimers with $g = 5$ nm, $g = 2$ nm, $g = 1$ nm, and $g = 0.5$ nm interparticle spacings respectively. (e) to (h):gold dimers with identical characteristics to the silver ones. Numerical labels stand for the number of multipoles included in the extinction spectrum computation. Incident field: unitary amplitude plane wave with polarization parallel to the dimer principal axis.

convergence, when interparticle gaps are small if compared with the particle size, and when the incident plane wave polarization is parallel to the dimer principal axis ($\mathbf{E}^{\parallel}_{\mathrm{inc},0}$) [50]. This is true even when only dipolar approximation would be enough to accurately solve the problem in the case of isolated spheres.

In our test cases silver and gold dimers have been investigated: optical con-

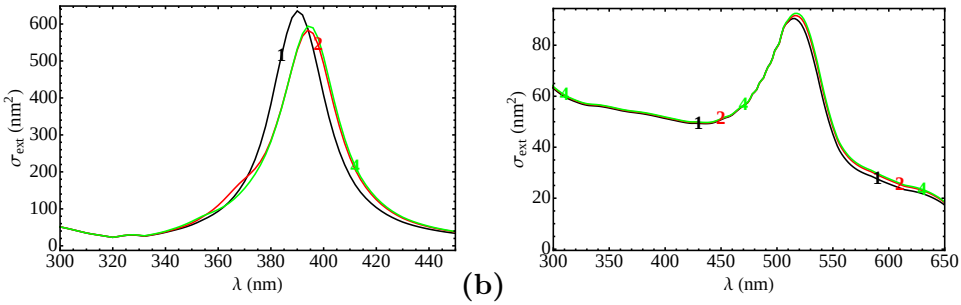


Figure 2.2.: Multipole dependence of optical extinction spectra for Ag (a) and Au (b) $D = 10$ nm dimers with $g = 0.5$ nm interparticle spacings. Numerical labels stand for the number of multipoles included in the extinction spectrum computation. Incident field: unitary amplitude plane wave with polarization normal to the dimer principal axis.

stants are obtained from the literature [53], and corrected for the electron reduced mean free path with a standard procedure which is described in detail elsewhere [54]. The size of the adopted cluster is $d = 10$ nm and all the clusters are taken to be embedded in a $n_m = 1.5$ nonabsorbing dielectric matrix, where $n_m$ is the matrix refractive index. This value has been chosen in order to describe the dimer behavior in a typical glassy host medium. The incident field is constituted by a linearly polarized plane wave propagating along the positive direction of the cluster reference frame $z$ axis. Finally the electric vector of the parallel polarization state is along the cluster reference frame $x$ axis, while the normal polarization state is along the $y$ one.

Fig.2.1 reports sets of extinction spectra for silver and gold dimers illuminated by a plane wave whose polarization state is parallel to the dimer principal axis. It may be clearly seen that for the closely spaced dimers of Fig.2.1(d) and Fig.2.1(h) high order multipoles have to be included in order to reach convergence, where a mere $N_M = 1$ would be enough in the isolated sphere case. As the interparticle gap increases less multipoles are needed in order to obtain full converge: in the $g = 5$ nm gap case a good convergence is reached even in dipolar approximation, with a final spectral profile closely related to the isolated sphere one (Fig.2.1(a)(e)). High order multipoles need to be included in the calculation because strongly focused local-fields appear at the nanoparticle junction in the case of incident parallel polarization [50]. Dimers behave essentially as small capacitors, with facing charges of opposite signs at the junctions, therefore building up strong fields with large spatial variability at the particle gap, which of course need the adoption of high order spherical harmonics in order to be correctly modeled.

From the above discussion it is natural to expect that in the case of a normal polarization incident plane wave spectral convergence properties are much less critical. Fig.2.2 reports extinction spectra for closely spaced ($g = 0.5$ nm) silver and gold dimers in the normal polarization case. Given the lack of strongly focused local fields at the dimers junction, at most 4 multipoles are included in order to bring spectra to convergence.

A typical fingerprint of interparticle coupling, in condition of parallel polar-

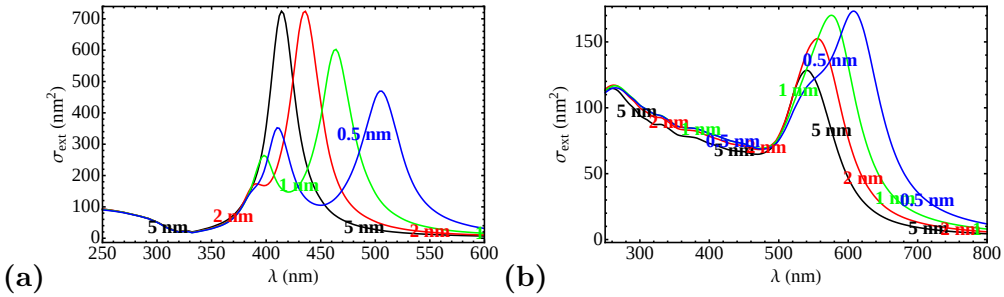


Figure 2.3.: Gap dependence of optical extinction spectra for Ag (a) and Au (b) $D = 10$ nm dimers. Incident field: unitary amplitude plane wave with polarization parallel to the dimer principal axis.

ization illumination, is the marked redshift of the collective dipolar resonances. Figure 2.3 reports extinction spectra for $D = 10$ nm Au and Ag nanoparticle dimers characterized by different interparticle gaps. Dipolar peaks redshift as the interparticle spacing decreases, since the interaction between charges of opposite sign, which are present at the junctions, lowers the energy needed to excite the collective mode. For the $g = 1$ nm and $g = 0.5$ nm gaps a peak attributed to higher order modes appears at lower wavelengths in the case of silver(Fig.2.3(a)): this is in agreement with the fact that higher order modes are characterized by shorter interaction lengths with respect to the dipolar one. Multipolar resonance for gold dimers are barely observable at $\lambda \simeq 500$ nm, since these modes suffer a damping caused by gold $d$ electrons.

If normal polarization is given, increasing blueshift as a function of interparticle separation is observed in Fig.2.4. This behaviour is again explained by the presence of facing charges at the nanoparticle junction. In the present situation charges of the same sign exert reciprocal repulsion at the gap, therefore increasing the energy needed to drive the collective resonance: in any situation smaller shifts are observed if compared to the parallel polarization illumination case. We note that all these findings are in excellent agreement with previously published calculations and experimental results [10; 28; 50; 55]. This finally gives a good validation of the employed code.

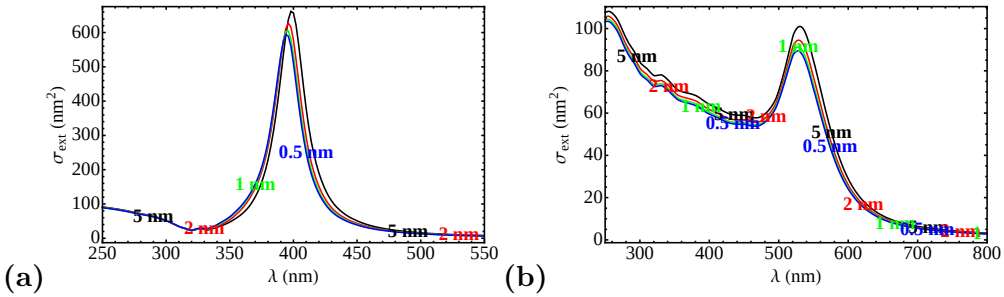


Figure 2.4.: Gap dependence of optical extinction spectra for Ag (a) and Au (b) $D = 10$ nm dimers. Incident field: unitary amplitude plane wave with polarization normal to the dimer principal axis.

## 2.3. Extinction properties of nanoparticle chains

### 2.3.1. Nanoparticle chains

Extinction properties of nanoparticle linear chains are, as might been expected, mostly similar to the dimer ones. Nevertheless chains offer the possibility to control one additional free parameter, i.e. chain lenght, in order to further tailor the optical properties of the sphere ensemble. Since in the dimer case normal polarization optical properties demonstrated to be relatively unsensitive to the ensemble topology, this behavior is expected also for linear chains and only parallel polarization illumination is assumed.The effects of interparticle spacing and chain length are investigated, while single cluster and matrix parameters are taken as before, i.e cluster size is chosen to be $D = 10$ nm, with a $n_m = 1.5$ dielectric host. We finally note that spectral convergence is always tested against the number of included multipoles.

Figure 2.5 and 2.6 report extinction spectra normalized to chain length for a set of different gaps and chain lengths. A large redshift of the collective dipolar resonance, being an increasing function of the chain length, is easily noted. Peak displacement tends to saturate as the chain length increases, stabilizing its position more quickly for larger interparticle separations. While for $g = 0.5$ nm the peak redshift has not reached saturation even for the $N_S = 32$ particle chain, as may be seen in Fig.2.5, $N_S = 16$ nanoparticles are nearly enough for the full convergence with a $g = 5$ nm interparticle distance (Fig.2.6(b)(d)). This behavior is simply explained in terms of weaker interparticle coupling when larger gaps are involved. It is interesting to observe that the intensity of the collective mode strongly increases as nanoparticles are added to the chain. This happens because the dipolar resonance moves aways from the $d$ electron threshold as the chain length grows. The described effect, even if present in both cases, is much stronger for gold chains, since the damping caused by $d$ electrons on the plasmon resonance is much more pronounced: once the resonance falls outside of the $d$ electron effect, its intensity is allowed to rapidly rise. Finally we note that multipolar resonances are only present in the silver chains, with intensity decreasing as the chain length grows and

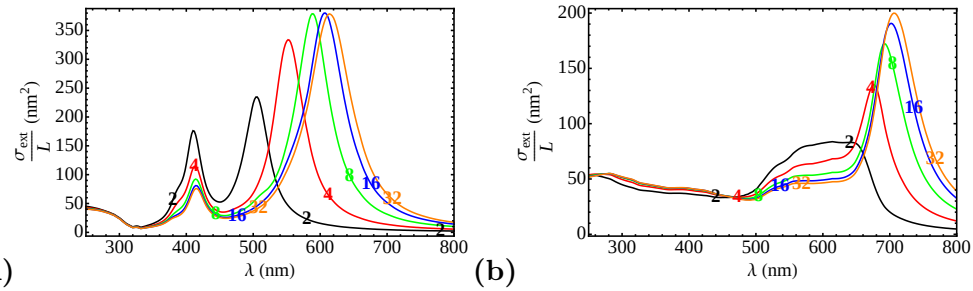


Figure 2.5.: Length dependence of optical extinction spectra for Ag (a) and Au (b) $D = 10$ nm nanoparticle chains with $g = 0.5$ nm interparticle gap. Labels stand for the number of spheres in the chains. Incident field: unitary amplitude plane wave with polarization parallel to the chain principal axis.

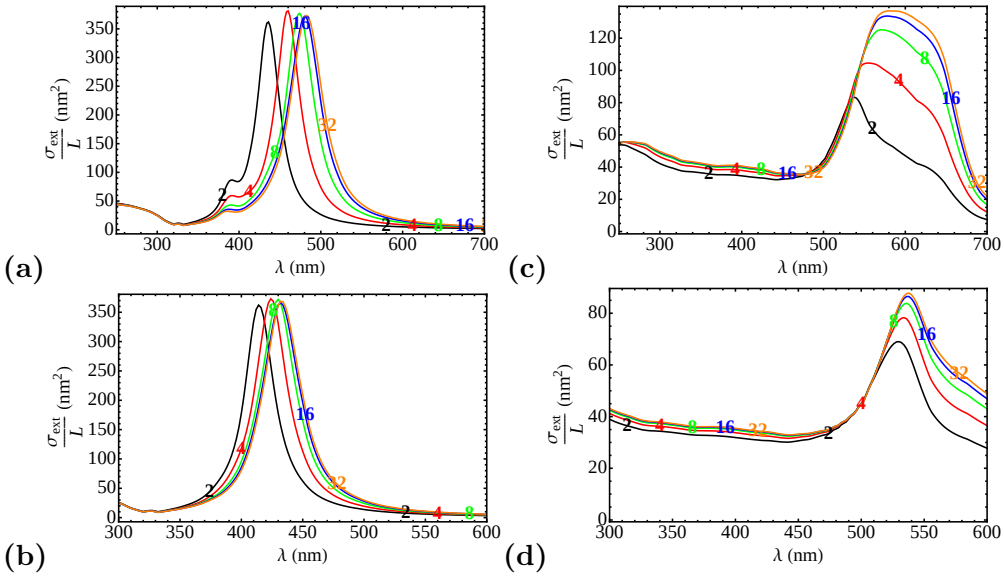


Figure 2.6.: Length dependence of optical extinction spectra for Ag (a)(b) and Au (c)(d) $D = 10$ nm nanoparticle chains with $g = 2$ nm and $g = 5$ nm interparticle spacings respectively. Labels stand for the number of spheres in the chains. Incident field: unitary amplitude plane wave with polarization parallel to the chain principal axis.

the dipolar intensity rises, and position remaining substantially unchanged. All these findings are in excellent agreement with previously published FDTD results [4].

### 2.3.2. Nanoparticle chains supporting photonic modes

Our GMM implementation extinction properties of long ($N_S = 500$) nanoparticle chains supporting mixed plasmonic-photonic modes are investigated. These peculiar structures, which are interesting for the fabrication of active plasmonic devices, are made of large $D = 100$ Au and Ag nanoparticles characterized by large scattering contributions to the total extinction cross section. Without discussing the physical details of these resonances, which are throughly treated elsewhere [5; 51; 56; 57], we simply remark that these modes arise from the diffractive coupling of the radiation scattered by each single sphere, and that in order to manifest themselves a normal polarization illumination is needed. Resonance peaks appear roughly at $\lambda = g \cdot n_m$, where $g$ is the interparticle separation and $n_m$ the matrix refractive index, and may show up in the spectrum as a peak or a dip, depending on the electromagnetic response of the single sphere and on the resonance position itself, being larger for wavelengths around the maximum scattering efficiency of the isolated particle. Extinction spectra for chains in vacuum ($n_m = 1.0$), with $g = 400, 450$ and $500$ nm in the case of silver, and $g = 450, 500$ and $550$ nm in the case of gold, are reported in Fig.2.7(a)(b). Sharp photonic modes arising from the coherent interaction of the spheres in the chain are present at the expected wavelengths for both Au and Ag chains, with larger peak intensities when superposition with the

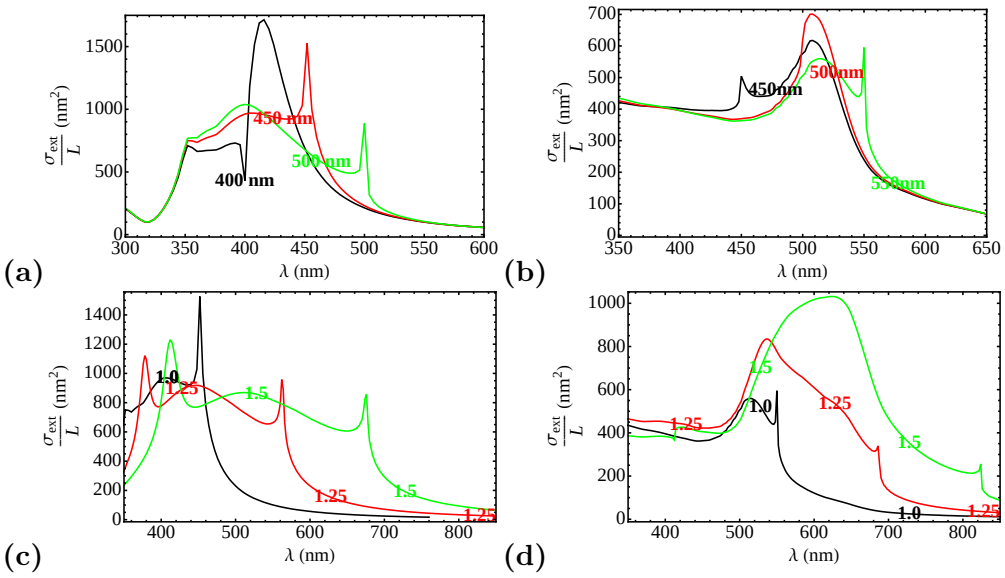


Figure 2.7.: Extinction spectra of $N_S = 500$ $D = 100$ nm nanoparticles chains supporting mixed plasmonic-photonic modes. (a)(b) Spectral dependence on interparticle spacing for Ag and Au chains respectively. (c)(d) Spectral dependence on host matrix refractive index for Ag and Au chains respectively. (a)(b): labels stand for chain interparticle spacings. (c)(d): labels stand for host matrix refractive index. Incident field: unitary amplitude plane wave with polarization normal to the chain principal axis.

single particle plasmon resonance occurs. Tuning of the diffractive peak may also be obtained by changing the refractive index of the embedding matrix, as it is shown in Fig.2.7(c)(d) for chains characterized by $g = 450$ nm and $g = 550$ nm interparticle separations, for Ag and Au respectively. Chosen refractive index are $n_m = 1.0$, $n_m = 1.25$ and $n_m = 1.5$. All the computed spectra are in quantitative agreement with the one previously published in the literature, and therefore also provide a further convincing test for the reliability of our code [5; 58].

## 2.4. Conclusion

A Fortran code was implemented in the framework of the Generalized Multiparticle Mie theory. Many different basic cluster configurations, each one involving peculiar peculiar physical aspects, have been modeled: this is an interesting starting ground in order to model more complex structures in the following chapter. Extinction spectra were also computed for limiting cases where high order multipolar expansions or large number of spheres had to be included in the calculation thus also proving the stability of the software implementation.

# 3. Generalized Multiparticle Mie: local-field

## 3.1. Introduction

Interacting metal nanoclusters are interesting for their peculiar local-field properties. Strong electrodynamic coupling leading to great field enhancement and focusing is in fact promising for molecular sensors and non-linear optical elements. Three dimensional subwavelength confinement along with plasmon waveguiding, and programmable plasmon nanolithography are envised applications as well [13; 31; 33; 59; 60].

Local-field computations are a relatively straightforward task in the context of GMM theory, once that the expansion coefficients for the internal and scattered fields are known, and the numerical problems arising from the computation of spherical Bessel Functions are solved. Nevertheless abrupt spatial variations of the local-field may appear especially when strongly coupled clusters are involved in the computation. In order to better understand the physical mechanisms which are at the base of strong local-field enhancement and focusing we perform field computations for basic systems strongly related to the ones studied in chapter 2:

- Nanoparticle dimers: local-field enhancement and focusing properties of nanoparticle dimers are investigated as a function of interparticle gap $g$, incident light polarization state and composition;

- Nanoparticle linear chains: local-field enhancement and focusing properties are investigated as a function of chain length and composition. In particular the correlation between the intensity of the collective dipolar peak and the local-field enhancement is pointed out, along with the role of metal $d$ electrons in determining this feature;

- Nanoparticle self-similar chains: self-similar chains are peculiar plasmonic structures which are described in Ref. [9], and believed to be extremely efficient nanolenses. Their field enhancement properties are discussed and analyzed using the approximation introduced in the original paper, and then adopting the full GMM approach in a second time.

As for the nanocluster extinction properties, the sphere ensembles described above are widely treated in literature, in order to provide good test cases for the reliability of our Fortran code [9; 28; 61–63].

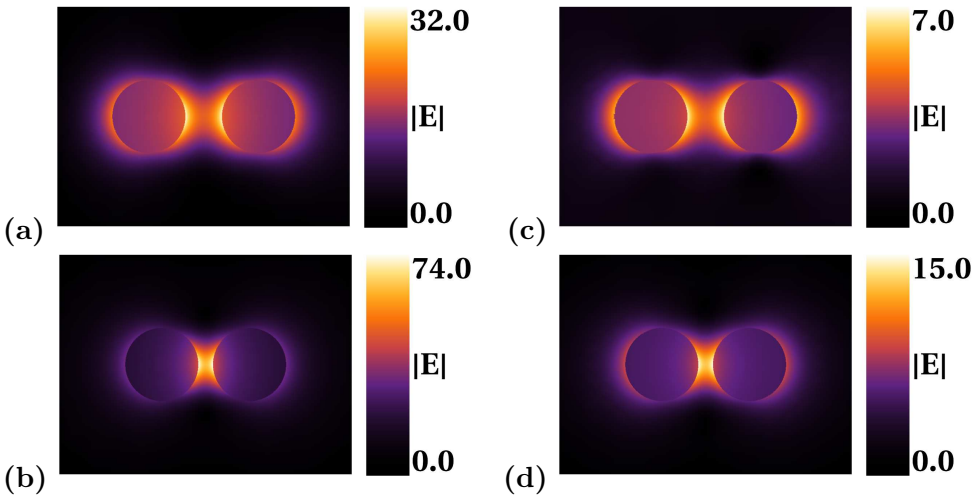


Figure 3.1.: Local-field maps on the $z = 0$ dimer equatorial plane: (a), (b) $D = 10$ nm Ag dimer with $g = 5$ nm and $g = 2$ nm interparticle spacing respectively; (c), (d) $D = 10$ nm Au dimer with same spacings as the Ag case. Incident field: unitary amplitude plane wave with polarization parallel to the dimer principal axis. Fields are always computer at the respective plasmon resonance wavelength (see Ch.2).

## 3.2. Local-field enhancement properties of nanoparticle dimers

As noted in chapter 2, the large plasmon redshift related to strong coupled dimers suggests the presence of highly enhanced local-fields at the pair junctions. The high multipolar orders needed to bring to convergence dimer spectra are also an indication of focused local-fields. On the contrary the stable plasmon shapes in the case of normally illuminated dimers put forward the hypothesis of a nearly unmodified field distribution.

In order to directly investigate local-field properties of noble metal nanoparticle dimers, the same sphere pairs studied in chapter 2 were adopted as model systems, using an identical nonabsorbing matrix as well ($d = 10$ nm, $n_m = 1.5$). The incident field is a unitary amplitude plane wave whose propagation direction and polarization states are taken as before. Up to 20 multipolar expansion are included in the computation in order to assure the convergence of the evaluated fields.

Figure 3.1 reports plots of the local-field modulus ($|\mathbf{E}|$) for $D = 10$ nm silver (Fig.3.1(a)(b)) and gold (Fig.3.1(c)(d)) dimers, illuminated by a parallel polarization plane wave, in the case of $g = 5$ nm and $g = 2$ nm interparticle spacings. Field is computed on the $z = 0$ plane in the cluster reference frame, i.e. on the dimer equatorial plane. Local-field enhancement caused by the electromagnetic coupling is already present in the case of largest gap, though the field distribution is roughly similar to the single cluster case. For the closer spacing ($g = 2$ nm) a significant modification of the field can be noticed, with higher field intensity building up at the nanoparticles junction: field enhancements as

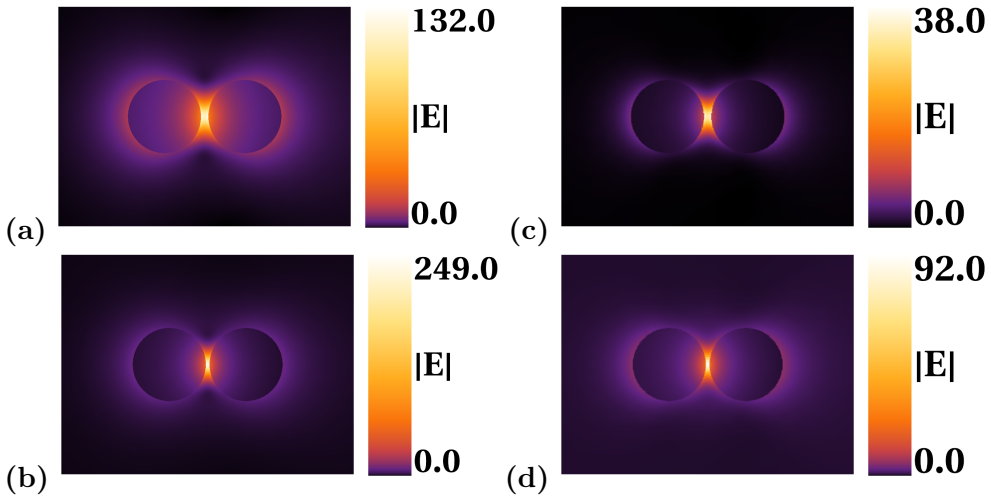


Figure 3.2.: Local-field maps on the $z = 0$ dimer equatorial plane: (a), (b) $D = 10$ nm Ag dimer with $g = 1$ nm and $g = 0.5$ nm interparticle spacing respectively; (c), (d) $D = 10$ nm Au dimer with same spacings as the Ag case. Incident field: unitary amplitude plane wave with polarization parallel to the dimer principal axis. Fields are always computer at the respective plasmon resonance wavelength (see Ch.2).

high as $|\mathbf{E}| \sim 70$ are found in the case of silver. Figure 3.2 is the same as Fig.3.1 except for the fact that $g = 1$ nm and $g = 0.5$ nm interparticle spacings are represented. Even larger field enhancement are obtained at the gap with $|\mathbf{E}| \sim 250$ for the silver dimer characterized by the narrower junction. While it is clear that silver is a much more performing material it terms of field enhancement, it is interesting to observe the behavior of relative field intensity increase. In the case of silver an amplification factor of about $|\mathbf{E}_{g=0.5}|/|\mathbf{E}_{g=5}| \sim 8$ is observed going from the wider gap dimer to the narrower one. For the gold dimers an approximate factor of $|\mathbf{E}_{g=0.5}|/|\mathbf{E}_{g=5}| \sim 12$ is obtained instead. This difference may again be explained with the strongest damping exerted on the Au plasmon by the $d$ electrons: as soon as the dipolar resonance peak redshifts outside their influence, plasmonic properties as well as field enhancement features are greatly enhanced. Figure 3.3 reports local-field modulus ($|\mathbf{E}|$) plots for silver and gold dimers illuminated by a normally polarized plane wave in the case of closest spacing $g = 0.5$ nm. It clearly stems from the plot that the field distribution is roughly similar to the isolated particle situation, even in this limiting case. No local-field enhancement beyond the one that should be expected for an isolated sphere is observed, in agreement with what was argued from the observation of the extinction spectra calculated in Ch.2. It is evident that plasmonic properties of such a structure are expected to be closely related to the single sphere one, and therefore they are not of much interest for practical application where large local-fields are necessary.

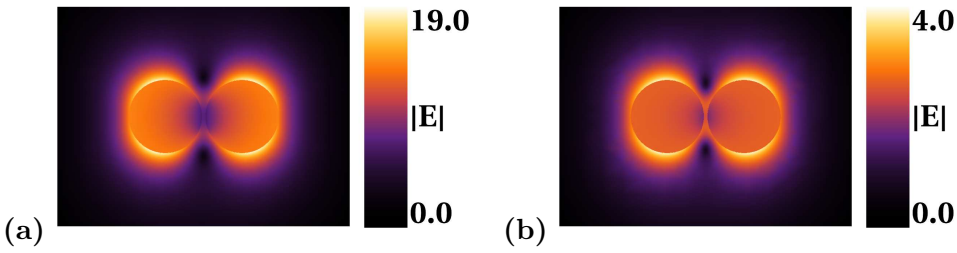


Figure 3.3.: Local-field maps on the $z = 0$ dimer equatorial plane: (a) $D = 10$ nm Ag dimer with $g = 0.5$ nm interparticle spacing; (b) $D = 10$ nm Au dimer with same spacings as the Ag case. Incident field: unitary amplitude plane wave with polarization normal to the dimer principal axis. Fields are always computer at the respective plasmon resonance wavelength (see Ch.2).

## 3.3. Local-field enhancement properties of nanoparticle chains

### 3.3.1. Nanoparticle chains

Investigations done so far have shown that when strongly coupled particle are concerned interesting optical properties principally arise when the incident field polarization is parallel to the structure principal axis, where a notable exception is represented by the chains of nanoparticles supporting mixed plasmonic-photonic modes. Near field optical features of linear chains are no exception, therefore their field enhancement properties are investigated as a function of chain length only for a parallel polarization incident plane wave and in the case of $g = 0.5$ nm spacing. Figure 3.4 reports local-field modulus ($|\mathbf{E}|$) plots for silver (left column) and gold (right column) nanoparticle chains, again computed on the $z = 0$ equatorial plane. In the case on the $N_S = 8$ (Fig.3.4(b)(e)) and $N_S = 16$ (Fig.3.4(c)(f)) nanoparticle chains only the four central spheres are represented in order to highlight the fields hot-spots. In all the modeled cases field enhancement and distribution are similar to the ones observed in nanoparticle dimers. For the Ag structures light intensity amplification is weakly dependent on the chain length, as can also be clearly noted in Fig.3.5, though slightly larger enhancements are observed especially for the $N_S = 8$ nanoparticle chain, which shows indeed the stronger extinction resonance (Fig.2.5). Length dependence is instead much more evident in the case of gold, where the role of $d$ electrons in the plasmon damping is mitigated by the progressive redshift of the dipolar resonance. All these findings are again in excellent agreement with previously published results [4].

### 3.3.2. Self similar chains

Self-similar nanoparticle chains are a peculiar family of nanosphere ensembles, where nanoclusters are linearly aligned, and progressively decreasing in size and separation [9]. Self similarity is assumed through the following equation:

$$D^{i+1} = \kappa D^i, \quad g^{i+1,i+2} = \kappa g^{i,i+1}, \tag{3.1}$$

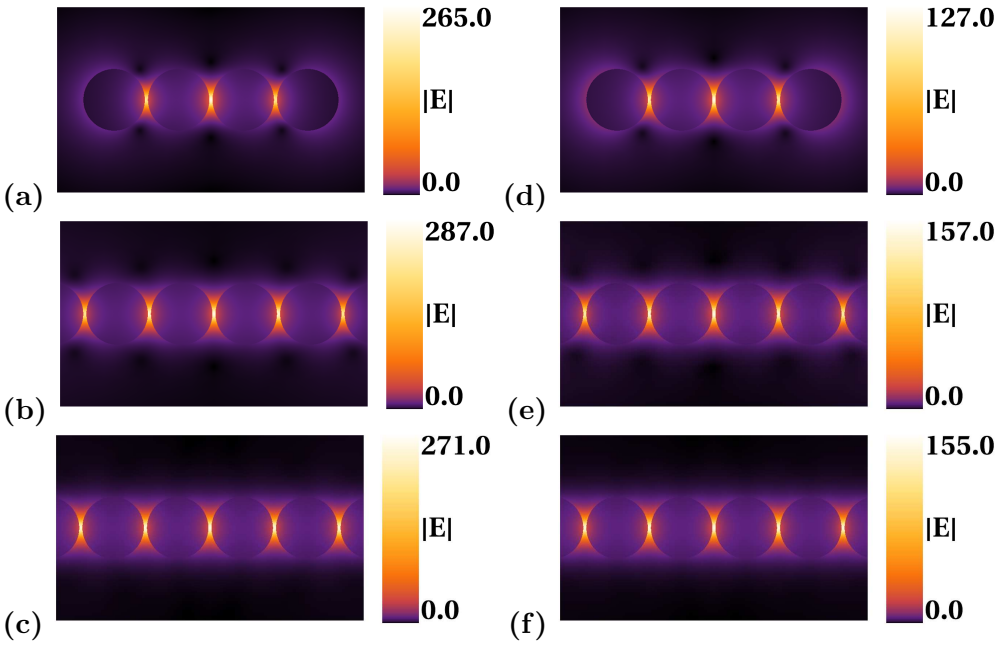


Figure 3.4.: Local-field maps on the $z = 0$ chain equatorial plane. (a), (b) and (c): $D = 10$ nm Ag chains $N_S = 4$ , $N_S = 8$ and $N_S = 16$ particle long, with $g = 0.5$ nm interparticle spacing. (d), (e) and (f) $D = 10$ nm Au chains with same lengths and spacing as in the Ag case. Incident field: unitary amplitude plane wave with polarization parallel to the dimer principal axis. Fields are always computer at the respective plasmon resonance wavelength (see Ch.2) and only the 4 central sphere of the chain are represented.

where $D^i$ is the diameter of the $i$-th sphere in the chain, $g^{i,i+1}$ is the separation between the $i$-th and $(i+1)$-th spheres and $\kappa$ is a constant. If $\kappa \ll 1$ is assumed then it is clear that the field distribution of a given particle will be only weakly disturbed by the presence of the next one. If close enough spheres are assumed, it appears evident that some sort of cascade enhancement can be obtained if the incident light polarization is parallel to the chain principal axis, with each sphere excited by the enhanced local-field of the former one. In principle such a mechanism seems to be able to provide giant local-field enhancement, as indeed it appears to be demonstrated in Ref.[9]. This kind of plasmonic structures seem particularly suitable for the testing of our code, given their extreme field focusing properties, therefore our GMM implementation was applied to this problem as follows:

1. The problem is solved by full GMM approach: the exact dielectric function used in Ref.[9] is adopted and free electron damping is included in the calculation. Spheres are supposed to be embedded in vacuum. Field enhancements are compared with results obtained with a GMM like approach and FDTD calculations published in a recent comment to the original paper [64];

2. The problem is solved in quasi-static approximation, choosing the exact

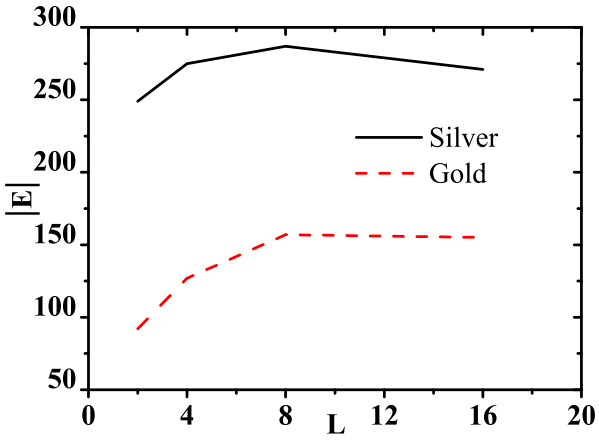


Figure 3.5.: Maximum field enhancement vs. chain length for $D = 10$ nm Au and Ag nanoparticle chains.

dielectric function used in Ref.[9], without applying any correction for the reduced electron mean free-path and embedding the spheres in vacuum. In practice this means that the problem is solved with the identical physical approximations adopted in Ref.[9]. We remark that in a practical calculation, quasi-static approximation is implemented in GMM theory by finding the non-trivial solution of the homogeneous analogue of the linear system (1.15);

Figure 3.6 reports field modulus plots for an asymmetric self-similar chain as in reference [9], both for the full solution (a) and the quasi-static approch (b). The diameter of the initial particle is taken to be $D^1 = 90$ nm, interparticle separation is defined as $g^{i,i+1} = \kappa(D/2)^{i+1}$ with $\kappa = 0.3$. The full GMM solution results, along with free electron damping, shows enhancements of the order of $|\mathbf{E}| \sim 280$ at $\lambda = 382$ nm, which are comparable with the one observed in classical chains. Therefore, even if these kind of structures are of great theoretical interest, their introduction appears unjustified from the practical point of view, since comparable enhancements may be obtained with structures which are much more readily synthesizable. These results were indeed already pointed out by Xu in a recent comment to the original paper [64]: GMM like

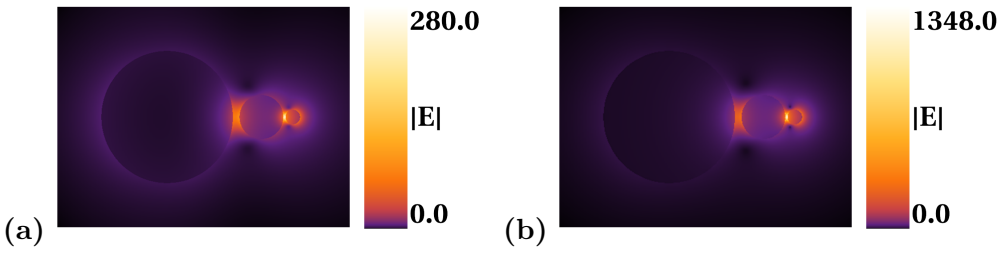


Figure 3.6.: (a) Local field map computed following the system of Ref.[9]: (a) full-solution including free electron damping; (b) Field computed in quasi-static approximation.

and FDTD methods are applied in the comment, with results in quantitative agreement with the ones reported above. Nevertheless Stockman *et al.* claimed in a response to the comment that the results proposed by Xu are unreliable, and that indeed in resonance conditions a superposition theory like the GMM approach should diverge [9].

In order to verify Stockman *et al.* claims, we finally perform a calculation in quasi-static approach explicitly excluding the free electron damping, i.e. in conditions that are identical to the ones adopted in the original paper. To our deligth we find field enhancement factors at $\lambda = 382$ nm which match quantitatively the ones obtained by Stockman *et al.* with their Multipole Spectral Expansion (MSE) method [9], reaching values as high as $|\mathbf{E}| \sim 1300$. Along with the peak enhancement values, field distributions are also identical to the one reported by the original authors. Therefore their claims may appear to be unmotivated.

## 3.4. Conclusion

The obtained results clearly show that GMM theory is applicable to local-field computation problems and that our implementation of this method is finally extremely reliable and stable. Obtained results give a good insight in local-field properties of relevant structures such as nanoparticle dimers and chains. We remark that these structures may be hardly investigated with an high degree of accuracy within other theoretical frameworks such as the FDTD one.

# Part II.

# Optical properties of metallic nanoplanets

# 4. Synthesis and characterization of bimetallic nanoplanets

## 4.1. Introduction

Silica based composites embedding metallic nanoclusters are intensively investigated due to the peculiar optical, magnetic and catalytic properties that they exhibit. Among different possible synthesis techniques, single or sequential ion implantation is currently used as a suitable technique for synthesizing NCs embedded in silica [65–67], in particular for controlling the composition and the local environment of bimetallic nanoclusters [68; 69]. This is of paramount importance for instance to control the peculiar properties of the composite which are function of the cluster size and density [69–73]. Therefore, with respect to the monoelemental case, alloy-based NCs can add a further degree of freedom, i.e. the composition, to the engineering of new materials properties. Of course, before this tunability in the nanocluster properties can be used for actual devices, a careful control over alloy cluster synthesis and stability has to be performed. For instance, ion implantation is usually coupled to post-implantation thermal treatments in different (inert, oxidizing or reducing) atmospheres for different times, depending on the needed final cluster arrangements [68]. Furthermore it has been demonstrated that it is possible to change and control composition and morphology of such nanoclusters by ion beam irradiation. In literature many works are present regarding the use of ion-beam-mixing of metal thin layers embedded in $SiO_2$ to obtain mixing of metal and silica atoms: if collisional mixing at interfaces exceeds a certain intensity metallic NCs can nucleate during ion irradiation [74–77]. More recently, nanometric size gold inclusions in silica matrix have been irradiated with MeV gold ions and a ring of nanometer-size clusters has been obtained in their vicinity [78]. Analytical studies have shown that this new cluster population tends to become monodisperse with the increase of the irradiation dose [79] .

We use an ion beam-based multi-step approach for modifying either composition of the alloy cluster or the dielectric matrix around them. In the first step, noble metal alloy nanoclusters are synthesized by sequential ion implantation and post-thermal treatments. The second step is ion irradiation with different light ions to create a halo of satellite clusters around the original ones: these kind of structures will be addressed as nanoplanets from now on.

It is clear that these structures are of great interest for the thematic developed throughout this thesis, i.e. plasmonic properties of electrodynamically coupled systems. Strong electrodynamic coupling among satellites and central cluster is indeed very likely to be present. Moreover the inherent flexibility of ion beam sinthesis allows to tailor the coupling as a function of structure topology and

composition.

In these sections the synthesis of $Au_xAg_{1-x}$ nanoclusters embedded in silica matrix and successively irradiated is described, along with their structural and optical characterization. Sequential ion implantation and post-irradiation treatments were performed with a 200 keV high-current Danfysik 1090 implanter at the INFN-INFM Ion Implantation Laboratory of INFN-LNL (Legnaro,Italy). Structural and compositional characterization was performed at CNR-IMM(Bologna, Italy) with a field-emission gun (FEG) FEI TECNAI F20 microscope operating at 200 kV equipped with an EDAX energy-dispersive x-ray spectrometer (EDS). Optical extinction spectra were collected with a CARY 5E UV-VIS-NIR dual beam spectrophotometer in the 200-800 nm wavelength range.

## 4.2. Synthesis and characterization of Au-Ag alloy nanoclusters

Fused silica slides were implanted with $Au^+$ and $Ag^+$ ions with energies of 190 keV and 130 keV respectively, to obtain a good overlap of the implantation profiles: simulation with SRIM code indicate that the projected range $R_p$ is of about 70 nm for the two species and the full width at half maximum is around 45 nm for Ag implantation and 25 nm for Au. Since silver is known to have a higher mobility than gold in silica, gold implantation was performed first, otherwise possible out-diffusion of silver could take place. Implantations were performed at room temperature and the current densities were maintained at 2 $\mu A/cm^2$ to reduce sample heating, while the used $3x10^{16}$ ions/$cm^2$ fluence produces a peak of dopant which is above the threshold for spontaneous colloid precipitation. Then, in order to promote further aggregation of dopant atoms in clusters and to obtain large (10-20 nm) and well separated AuAg alloy clusters [68], the implanted slides were heat-treated in a conventional furnace in air at 800°C for 1h. This is the reference sample labeled as *AuAg*. The size distribution is bimodal with two gaussian distributions centered at $\langle D_{Surf} \rangle = 7.1$ nm and $\langle D_{R_p} \rangle = 24$ nm for the clusters at the surface and at the $R_p$ respectively. A TEM Bright-Field image of this sample is reported in Fig.4.2.

## 4.3. Synthesis and characterization of Au-Ag alloy nanoplanets

In order to obtain the desired nanoplanetary structures the *AuAg* reference sample was irradiated with ions characterized by different atomic numbers ($He^+$, $Ne^+$, $Kr^{++}$), so as to get different amounts of nuclear energy loss $S_n$, and therefore trigger the amount of ejected material from the original clusters [7]. Irradiation parameters are reported in Tab.4.1 where it is possible to see that increasing the atomic number Z of the incident ion, nuclear energy loss clearly predominates. Moreover parameters are chosen according to the following guidelines:

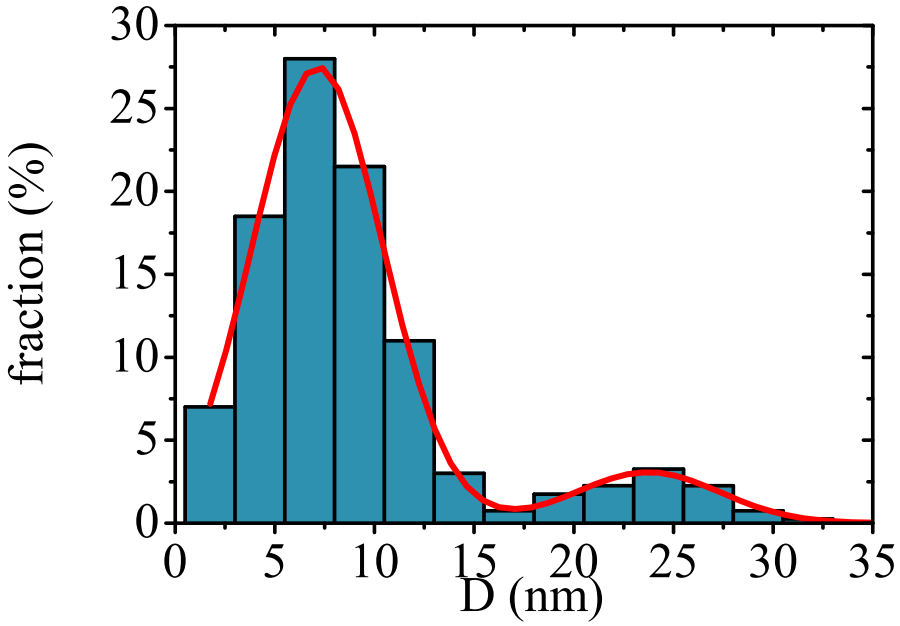


Figure 4.1.: Histogram of the size distribution of $Au_xAg_{1-x}$ cluster in the *AuAg* reference sample.

| Ion | Energy (keV) | Current Density ($\mu$A/cm$^2$) | Fluences (ions/cm$^2$) | $S_n$=$E_n$/Etot (% ) |
|---|---|---|---|---|
| $He^+$ | 25 | 6.3 | 32x $10^{16}$ | 10 |
| $Ne^+$ | 100 | 1.6 | 5.2x $10^{16}$ | 43 |
| $Kr^{++}$ | 380 | 0.42 | 1.2x $10^{16}$ | 67 |

Table 4.1.: *Irradiation conditions used to obtain nanoplanet structures starting from the $Au_xAg_{1-x}$ sample: irradiation energies, fluences and nuclear ($S_n$) fraction of the ions energy loss are reported*

- irradiation energies are chosen so that ions have a projected ranges of about 200-250nm, i.e about 3 times the projected range of the implanted metallic species ( about 70 nm for both Au and Ag);
- fluences of the different ions are chosen so as to release the same energy density over the whole ion range (190keV/nm$^3$);
- different current densities for each ion are taken in order to have the same power density ($2.5\times10^8$ W/cm$^2$) released on the sample.

In Figure 4.3 the bright-field TEM cross-sectional images of the *AuAg* reference sample irradiated with $He^+$, $Ne^+$ and $Kr^{++}$ ions are shown. Ion irradiation promotes the formation of satellite clusters around each original clusters, similarly to what reported in a ion bean mixing experiment of Au islands irradiated by Au MeV-ions [75; 78; 80]. Moreover, comparing Figure 1(a) and (d) we note that Kr-irradiated *AuAg* sample has a greater volumetric density of satellite clusters than the He-irradiated *AuAg* sample. In order to have a more quanti-

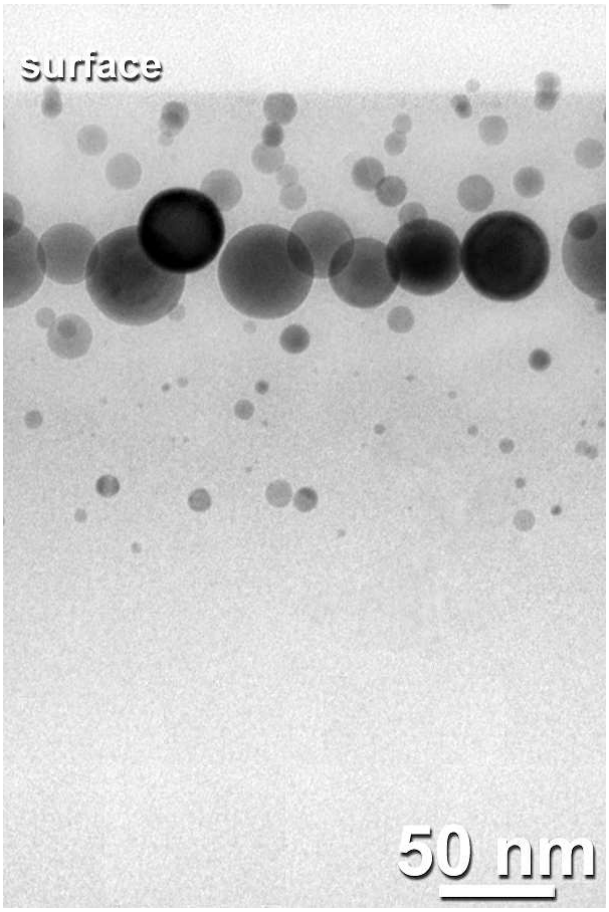


Figure 4.2.: Bright-field TEM cross-sectional micrograph of the reference sample AuAg

tative analysis, we analyze images collected during TEM measurements, getting different data as:

- satellite diameter: mean satellite size and size distribution (independent from the original mother cluster dimensions). We measure this quantity directly from Bright-field TEM images, even if it often difficult to distinguish satellite particles having size less than 1 nm;
- maximum satellite distance ($d_{max}$): Maximum satellite distance from the mother cluster surface (independent from the original mother cluster dimensions). An annular region around the original NCs, in which most of the satellite particles are present, is identified. Then the radius of this region is measured and, subtracting the mother cluster radius, $d_{max}$ is obtained. Of course, it happens that the original alloy cluster are not well separated and so it can be difficult to distinguish satellite annular regions belonging to different mother cluster.
- $n_{sat}$ the total number of satellite clusters: obviously, it may be very difficult to measure all the satellite particles, since some of them are not

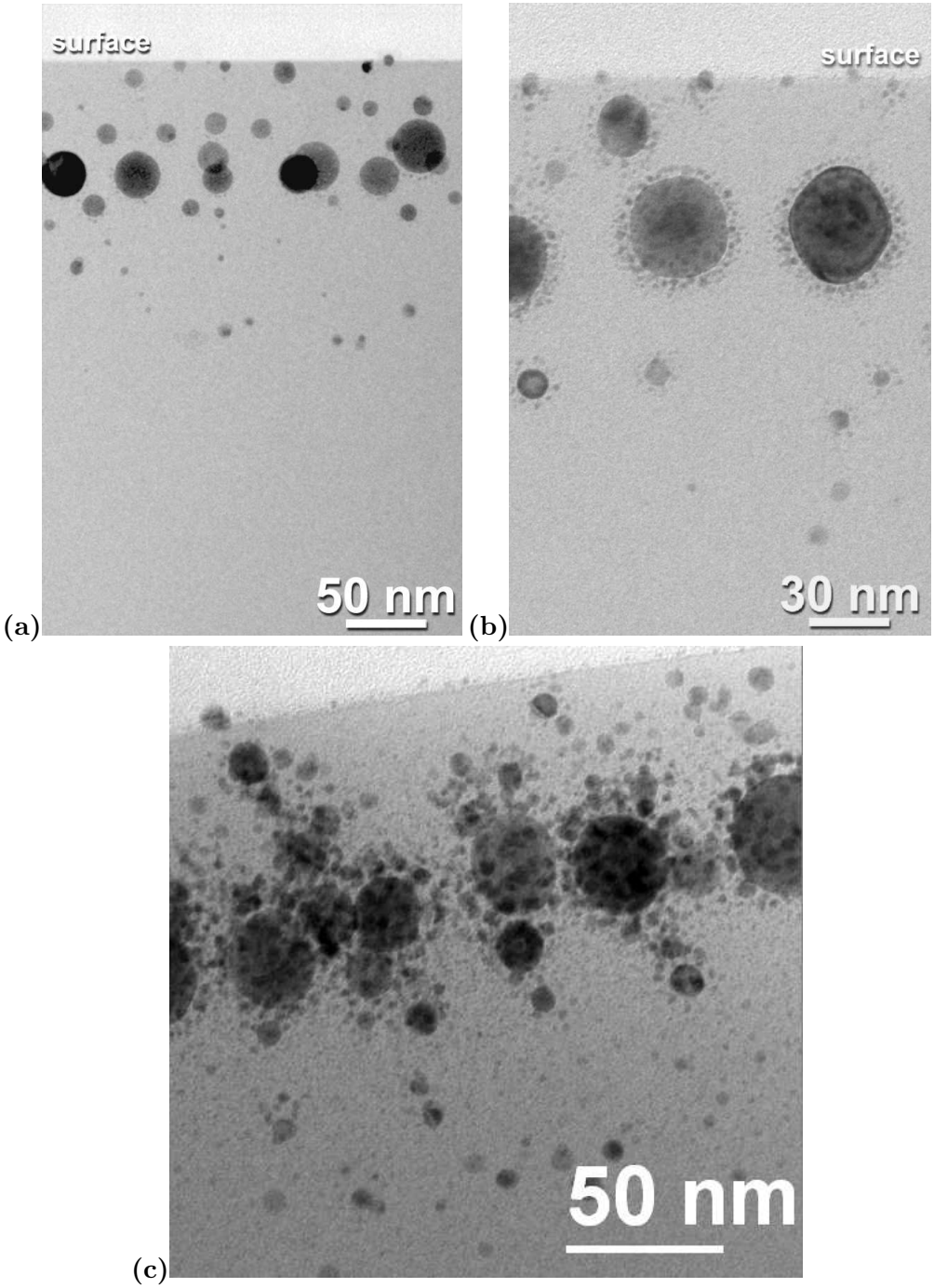


Figure 4.3.: Bright-field TEM cross-sectional micrograph of the reference sample AuAg irradiated with He ions at 25 keV (a), with Ne at 100 keV (b) and with Kr at 380 keV.

| Ion | satellite diameter (nm) | $d_{max}$ (nm) |
|---|---|---|
| $He^+$ | 1.1±0.1 | 3.8±0.6 |
| $Ne^+$ | 1.6±0.3 | 6.2±1.2 |
| $Kr^{++}$ | 2.3±0.5 | 7.7±1.2 |

Table 4.2.: *Experimental data from TEM analysis of the AuAg samples irradiated with different ions.*

visible on the recorded images because placed behind by original cluster, as TEM images are 2D projections of 3D specimens. Anyway, even if TEM image interpretation often challenging, there is not another characterization technique that allows such a detailed structural analysis at the nanometer scale.

The obtained structural data are summarized in Table 4.2: the mean value for each measure ± the standard deviation are reported.

Ion-irradiation may affect also the composition of the irradiated nanostructure, so we compare mother cluster composition with that of satellite clusters, performing EDS compositional analysis with a focused 2 nm electron beam of the FEG-TEM in the central part of the mother cluster and on the satellite cluster. The atomic ratios Au/Ag (comparing the AuL and AgL X-ray emission lines) measured on the two regions are summarized in Table 4.3. It is possible to see that ion irradiation promotes the Au preferential out-coming from the original alloy cluster, and this preferential elemental extraction is independent of the irradiating ion. The preferential Au emission from the original alloy could be explained in terms of an elemental-selective vacancy formation in the NCs, or it could be a consequence of elemental segregation, or radiation enhanced diffusion processes. Discussion of all these hypothesis is anyway behind the scope of the present chapter.

Figure 4.4 shows the experimental optical extinction for the *AuAg* and the subsequently irradiated samples. The unirradiated sample presents one single extinction band located at 478 nm, between the silver (410 nm) and gold (530 nm) plasmon resonances in silica (refractive index 1.45), as might been expected considering the alloy formation [8; 68]. Subsequently to the $He^+$ irradiation the extinction peak redshifts to 485 nm, its peak intensity is slightly reduced, while its full-width at half-maximum (FWHM) presents a moderate increase. $Ne^+$ irradiated sample shows a similar behavior: one single extinction feature

| Ion | Au/Ag mother cluster | Au/Ag satellite cluster |
|---|---|---|
| $He^+$ | 1.2±0.1 | 2.5±0.7 |
| $Ne^+$ | 1.2±0.1 | 2.8±0.9 |
| $Kr^{++}$ | 1.4±0.2 | 4.0±0.4 |

Table 4.3.: *EDS compositional analysis at AuL and AgL edges on the sample AuAg irradiated with different ions. Au/Ag atomic ratio measured in the central part of the original $Au_xAg_{1-x}$ NCs and on satellite cluster halo are reported.*

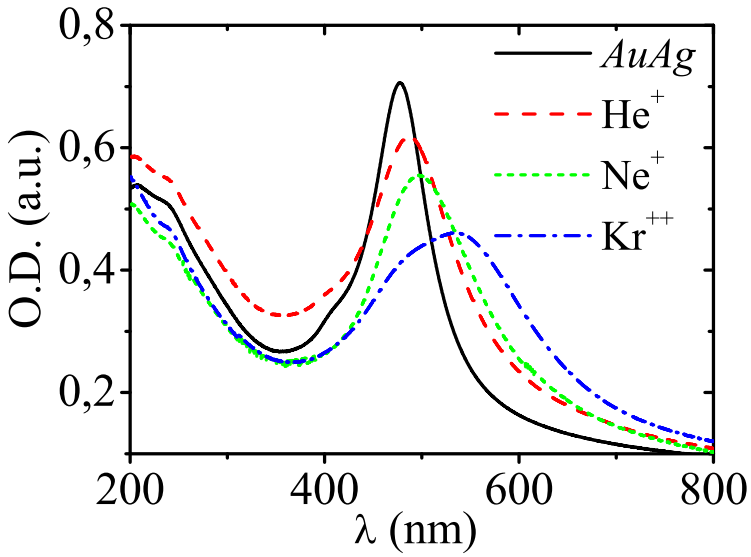


Figure 4.4.: Optical density of the reference sample *AuAg* before (a) and after ion irradiation with 25 keV He ions (b),100 keV Ne ions (c) and 380 keV Kr ions (d).

is present at 497 nm, with reduction of the peak intensity, an increase of its FWHM and a slightly more pronounced damping than in the helium case. This trend is only partially followed in $Kr^{++}$ irradiated sample. While stronger band damping and redshift are evident, the extinction spectrum shows two clearly distinct features: a shoulder at about 495 nm and a principal peak at 538 nm, beyond the pure gold plasmon peak in silica. All these changes may indeed be attributed to the electromagnetic coupling between the central and satellite clusters, and will be thoroughly investigated in the next chapter.

### 4.3.1. Conclusions

We have presented an ion beam-based multi-step approach to synthesize alloy NCs embedded in silica. In the first step, noble metal alloy NCs are synthesized by sequential ion implantation and post-thermal annealing. The second step is ion irradiation for tailoring size, composition and topology of pre-formed NCs. It has been found that ion irradiation promotes the material ejection from the original cluster with the subsequent formation of new satellite particles around each original cluster: these newly obtained configuration have been named nanoplanets. Satellite halo morphology has been found to be strongly related to the nuclear component of the released energy, and therefore to the mass of the incident ion. Moreover EDS compositional analysis reveals that satellite cluster are richer in Au than the original ones. Finally, by observing the optical-spectra of the samples irradiated with different ions, it is possible to note the presence of a single surface plasmon resonance band between those of pure Au and Ag clusters, with the position of the extinction peak always red-shifted with respect to the one of the unirradiated sample. It has also been noted that the plasmon red-shift increases with the mass of the irradiating ion.

We remark the great importance of nanoplanet optical features. Plasmon shift is probably an indication of strong interparticle coupling between satellites and between the satellites and the mother cluster. Along with the strong electrodynamic coupling strong local-field enhancement are likely to show up. Moreover the inherent flexibility of the ion beam synthesis process could possibly allow a precise tailoring of nanoplanet far- and local-field properties.

# 5. Modeling far- and local-field properties of bimetallic nanoplanets

## 5.1. Introduction

Interaction of light with metal nanoclusters embedded in insulating matrices has received a great deal of attention in the last decades [2]. In particular it is well known that glass-embedded noble metal nanoclusters exhibit strong surface plasmon resonance in the visible range, and can increase the third order susceptibility ($\chi^{(3)}$) of the host material by orders of magnitude [3]. If isolated spherical nanoclusters are involved, extinction and field distribution properties are essentially determined by the cluster size and by the metal and matrix dielectric responses. Speaking of interacting cluster ensembles instead, the optical properties are a strong function of the interparticle electromagnetic coupling. Particle size, number and relative position are essential parameters as well as the polarization state of the incident field, with one more degree of freedom if metal alloy nanocluster are involved [4; 62; 68]. Given their flexibility and the peculiar far- and local-field properties, ensembles of interacting nanospheres are attractive for a wealth of uses going from sensing employments to waveguiding applications [13; 14; 29; 81].

In spite of their attractive properties, it is difficult to obtain coupled cluster ensembles with controlled features such as interparticle spacing or structure topology, even if conventional lithography techniques allow the synthesis of high quality structures on a small scale [56; 82]. On the other hand ion beam processing provides a valuable approach in order to synthesize large quantities of metallic nanoclusters in different matrices. The inherent flexibility of this method, along with additional thermal treatments, allows to carefully tailor the compositional and topological characteristic of exotic structures such as AuAg bimetallic nanoplanets. While size and composition of the average structure may be decided in the first implantation steps, accompanied by thermal annealing, the overall multi cluster spatial configuration is tailored via ion irradiation.

Together with the control of the morphological characteristics also far- and local-field properties of the nanoparticle aggregate may be tightly tailored as a function of the interparticle coupling.

In this chapter far- and local-field properties of AuAg bimetallic nanoplanets are investigated by applying two distinct theoretical approaches:

- Generalized Multiparticle Mie theory: GMM method is applied to study far-field properties of nanoplanets. This theoretical framework is perfectly suited to model such structures, which given their complexity could

be hardly handled with an alternatively formalism such as FDTD method where 10 sphere aggregates poses already a significant computational challenge [4];

- Hybrid Mie Maxwell-Garnett (MMG): a simplified model based on the coupled use of core-shell Mie and Maxwell-Garnett (MG) effective medium theory is employed. In this framework only far-field properties and strictly isolated spherical geometries may be modeled, though this approach allows some interesting insight in the investigated physical phenomena and a useful double-check with the GMM results;

- Local-field Generalized Multiparticle Mie theory: GMM method is applied to study nanoplanet local-field properties on the base of far-field results.

Starting from the obtained modeling results, effects of the electromagnetic coupling on the extinction spectra and on the local-field distribution of alloy nanoplanets are discussed, envisaging the synthesis of possible systems characterized by even better plasmonic properties.

## 5.2. Far-field properties of alloy nanoplanets

### 5.2.1. Nanoplanet extinction properties by Generalized Multiparticle Mie approach

Noble metal nanoplanets are for many aspects an ideal system to be modeled within the framework of GMM theory, since they are essentially large ensembles of strongly coupled spherical nanoparticles. The simulation of such a system could be hardly handled with an alternative approach, such as FDTD method or DDA approximation, and when possible this would be at high computational costs [4]. GMM approach is here applied in order to model far- and local-field properties of AuAg alloy nanoplanets. Model targets are built following the here reported guidelines:

- a geometrical model target is built on the base of TEM images and structural data such as satellite size and distance distribution (Tab.4.2, Fig.5.2). Only the nanoplanets at the projected range $R_p$ are considered since: (i) the vast majority of the implanted species precipitates in that range [7]; (ii) the extinction cross section is know to scale as the nanoparticle volume in quasi-static approximation [2] (Fig.4.1). Moreover, even if in principle a statistical distribution of nanoplanets should be used in order to accurately model the optical properties of the whole system, only mean values for the central cluster size are used ($\langle D_{R_p} \rangle = 24$ nm). We are allowed to make this choice because the introduction of the experimental size distribution in the calculation of the *AuAg* sample extinction properties does not bring significant spectral shape modifications, with respect to the calculation carried on considering only the mean size values [83];

- according to TEM-EDS compositional analysis alloy composition is set to $Au_{0.6}Ag_{0.4}$ for the central clusters and to $Au_{0.75}Ag_{0.25}$ for the surrounding

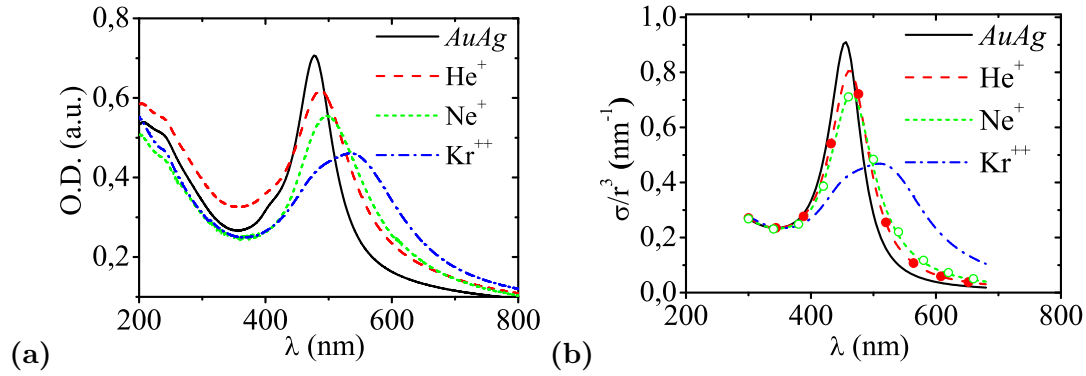


Figure 5.1.: (a) Experimental optical extinctions for unirradiated and irradiated samples as described in chapter 4, measured with unpolarized light. (b) Theoretical extinction spectra for a single $Au_{0.6}Ag_{0.4}$ particle of 12 nm of radius (black line), and for targets reported in Fig.5.4(b), Fig.5.5(b) and Fig.5.6(b) ($He^+$ dashed, $Ne^+$ short-dashed, $Kr^{++}$ dot-dashed lines), following GMM approach. Empty and filled circles correspond to spectra calculated following MMG approach.

satellites (Tab.4.3). Alloy optical constants are taken from the literature [84], and have been corrected for the reduced electron mean free path [54]. We remark that slight variations of alloy composition have minor effects on modeled spectral features. To take into account the atomic metal dispersed in the matrix after the irradiation treatment, the host local refractive index is raised to $n_m = 1.50$, corresponding to a local atomic concentration of about 1% in an effective medium picture with a silica matrix ($n_m = 1.45$).

Targets for $He^+$ and $Ne^+$ irradiated samples may be seen in Fig.5.4(b) and Fig.5.5(b), while the *AuAg* model consists in a $Au_{0.6}Ag_{0.4}$ isolated particle of 24 nm of diameter. With reference to the $Kr^{++}$ irradiated structure (Fig.5.6(b)), the dipolar coupling mechanism is not suitable for reproducing the observed spectral properties, which are likely to be determined by strongly coupled cluster of close dimensions. Thus a model target which includes high multipolar coupling between neighboring nanoplanets is proposed, where the coupling is provided by larger satellites that are present at the satellite halo intersections (Fig.5.6(b)). All the extinction spectra are now calculated for an unpolarized plane wave, in order to correctly take into account the model target lack of spherical symmetry, especially in the case of the $Kr^{++}$ irradiated sample.

Figure 5.1 shows calculated extinction spectra for a single $Au_{0.6}Ag_{0.4}$ particle (*AuAg* sample) and for the model targets reported from Fig.5.4 to Fig.5.6, corresponding to the irradiated samples. Spectral shapes and extinction peak trends are in good agreement with experimental data, for all the modeled samples. Small blueshift and underestimation of peak width are present: this discrepancy may probably be reduced by introducing a statistical size distribution for the nanoplanets, nevertheless it can not be ruled out that different effects, such as implantation damage or variations of the local refractive index, play a role in the small observed disagreement. In spite of this, general spectral behaviors

are reproduced with remarkable accuracy.

Plasmon shift and damping are attributed to the electromagnetic coupling between the central and satellite clusters, and to the atomic metal locally dispersed in the matrix after the irradiation treatment. With reference to the $Kr^{++}$ irradiated sample, the purely dipolar mechanism is unable to reproduce the measured spectral properties, and thus a three planet model target which includes high multipolar coupling is introduced, where the coupling is provided by larger satellites which are present at most of the satellite halo intersections (Fig.5.6(b)). The correspondence between theoretical and experimental extinctions is especially noteworthy, with the observed spectral features at 495 and 538 nm correctly reproduced, and interpreted as the contributions of different light polarization states. Redshifted peak arises from polarizations parallel to the axes of nanoplanet dimers or multimers, like the ones reported in Fig.5.6(b), while the lower wavelength shoulder is assigned to the normal polarization states (see Ch.2). Systematic calculations showed that the theoretical spectral shape is robust against minor statistical modifications of the assumed target, as far as planar coupling is preserved. The same calculations prove that satellite clouds strongly enhances planar NPs coupling in the case of parallel polarization states, and can therefore trigger the 538 nm peak intensity.

### 5.2.2. Nanoplanet far-field properties by Hybrid Mie Maxwell-Garnett approach

Bimetallic nanoplanets are constituted by a large central cluster surrounded by a halo of smaller satellite clusters very close to its surface (Fig.4.3). The whole structure retains a rough spherical symmetry, thus a simplified modeling technique could consist in considering the whole nanoplanet as a single core-shell cluster, where the core is identified with the central mother cluster, and the shell contains all the sourrounding satellites. Since the composition of the shell is not homogeneous, its optical response must be modeled by adopting an effective medium approach, with the two constitutive materials chosen to be the host dielectric matrix and the AuAg alloy which forms the satellites.

Maxwell-Garnett formalism is applied in order to obtain the shell dielectric function [85]: in this picture the heterogeneous material is made of an host matrix containing inclusions which are small if compared with the wavelengths of interest. Dipolar interaction among the inclusions is taken into account, with the their volume fraction $p = V_{\mathrm{inc}}/V_{\mathrm{tot}}$ limited to be a few percent so that higher multipolar orders can be neglected. The final expression for the Maxwell-Garnett effective dielectric function $\varepsilon_{MG}$ may then be written as [85]:

$$\frac{\varepsilon_{MG} - \varepsilon_m}{\varepsilon_{MG} + 2\varepsilon_m} = p\frac{\varepsilon_{AuAg} - \varepsilon_m}{\varepsilon_{AuAg} + 2\varepsilon_m}, \tag{5.1}$$

where $\varepsilon_m$ and $\varepsilon_{AuAg}$ are the dielectric functions of the host matrix and of the alloy satellites respectively. Only the $He^+$ and $Ne^+$ irradiated samples may be expected to be correctly modeled using the MMG approach, because the approximation adopted in this method explicitly exclude multipolar interaction. This kind of strong coupling is very likely to be present in the $Kr^{++}$ irradiated

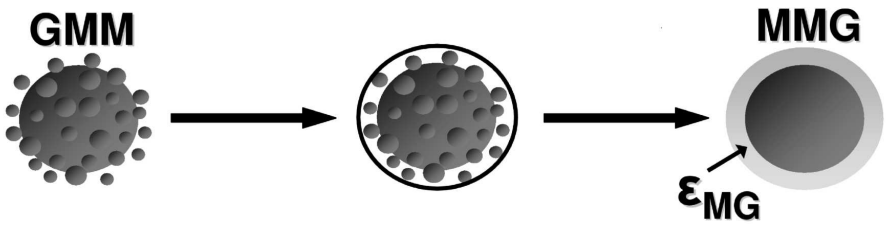


Figure 5.2.: Schematic representation of MMG model target construction.

sample, where central cluster and satellite dimensions are closer and high multipolar orders are likely to determine the extinction spectral shape (see Ch.2 and Ch.3).

In order to perform a successful modeling an accurate core-shell target must be built: to do so the procedure adopted for the GMM simulations is used, with an additional step which consists in building a shell effective dielectric function $\varepsilon_{shell}$ according to Eq.(5.1), obtaining

$$\frac{\varepsilon_{shell} - \varepsilon_m}{\varepsilon_{shell} + 2\varepsilon_m} = p\frac{\varepsilon_{sat}(\langle D_{sat}\rangle) - \varepsilon_m}{\varepsilon_{sat}(\langle D_{sat}\rangle) + 2\varepsilon_m}, \tag{5.2}$$

where $\varepsilon_m$ is the host matrix dielectric function and $\varepsilon_{sat}(\langle D_{sat}\rangle)$ the satellite one, which is dependent on the satellite average size after the electron damping correction. Finally $p$ is defined as

$$p = \frac{\sum_n^{n_{sat}} V_{sat,i}}{V_{shell}} \tag{5.3}$$

where $V_{shell}$ is the volume of the smallest possible shell containing all the satellites, and $V_{sat,i}$ is the volume of the $i$-th satellite.

Figure 5.3 reports experimental (a) and simulated MMG extinction spectra (b) for the as implanted ($AuAg$) and the $He^+$ and $Ne^+$ irradiated samples. Spectral shapes and extinction peak trends are in good agreement with experimental

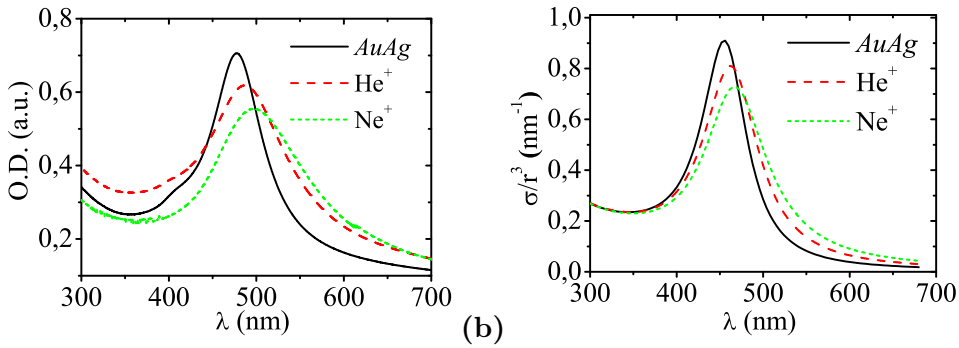


Figure 5.3.: (a) Experimental optical extinctions for unirradiated and irradiated samples as described in chapter 4, measured with unpolarized light. (b) Theoretical extinction spectra for a single $Au_{0.6}Ag_{0.4}$ particle of 12 nm of radius (black line), and for targets obtained from the ones reported in Fig.5.4(b) and Fig.5.5(b) ($He^+$ dashed, $Ne^+$ short-dashed lines), following MMG approach.

data, for each of the examined cases. A slight underestimation of peak width, as well as a small blueshift of the simulated extinction peaks can be noted, nevertheless complexity of the studied systems must be kept in mind, since parameters such as local refractive index, experimental dielectric function and implantation damage are not easily determined and modeled. In spite of this, general spectral behaviors are reproduced with remarkable accuracy, with this meaning also that only dipolar interactions between the satellites and the central cluster determine the far-field properties of $He^+$ and $Ne^+$ alloy nanoplanets. We remark that the optical extinctions of the $He^+$ and $Ne^+$ irradiated samples are calculated with both GMM and MMG formalisms, with obtained results reproducing the observed experimental behaviors and in mutual quantitative agreement. The above theoretical matching is corroborated by the fact that GMM far-field spectra converge by including only dipolar interactions.

## 5.3. Nanoplanet local-field properties by GMM approach

The large plasmon shift observed above is an evidence of strong interparticle coupling, and therefore of a substantial local-field enhancement and focusing [4; 6]. Figure 5.4(c) to Fig.5.6(c) report targets and TEM images of typical NPs

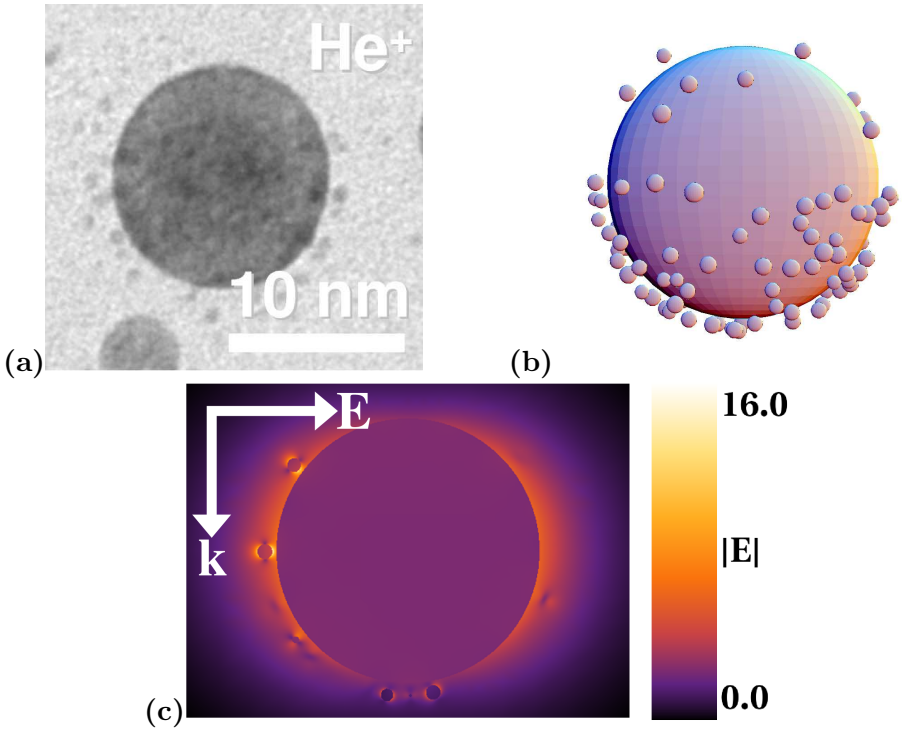


Figure 5.4.: (a) TEM image of a representative $He^+$ irradiated nanoplanet; (b) model target built one the base of TEM images and derived structural data; (c) local field modulus $|\mathbf{E}|$ map calculated on a nearly equatorial plane at the plasmon $\lambda \sim 462$ nm wavelength. Field wavevector and electric vector are as described in the figure.

configurations along with the plots of the local-field modulus $|\mathbf{E}|$. Electric field is computed on a nearly equatorial target cross-section, at the plasmon peak wavelength, with a linearly polarized plane wave normalized to unity chosen as incident field. Figures 5.4(c) and 5.5(c) report fields calculated for $He^+$ and $Ne^+$ samples at 462 and 466 nm. Strong enhancement and focusing are present at the interparticle gap between satellites and mother cluster, being a function of satellite distance and orientation with respect to the field polarization: maximum intensity is in fact obtained when satellite to central cluster axis is parallel to the electric field vector [4; 9]. In the studied cases enhancements as high as $|\mathbf{E}| \sim 20$ are obtained, confined to a region whose size is comparable to the satellite one. Enhancements of the order of $|\mathbf{E}| \sim 7$ are expected for a $Au_{0.6}Ag_{0.4}$ single particle with a 12 nm radius. It is convenient to underline the fact the high multipolar orders need to be included in order to bring local-field plot to convergence, even if extinction spectra are exhaustively described by an interacting dipolar approach. This means that the small strongly focused hot-spots are not able to influence the overall far-field distribution, while they still need a multipolar approach in order to be correctly described on a local scale.

The above discussion does not hold for the $Kr^{++}$ irradiated sample which requires a separated treatment, since inter nanoplanet coupling is here taken

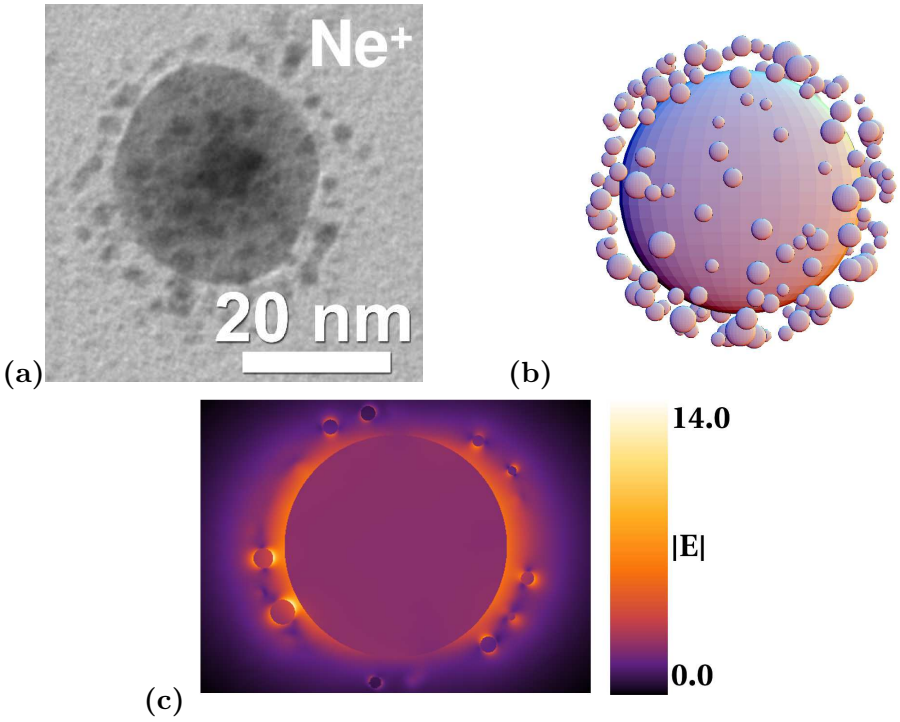


Figure 5.5.: (a) TEM image of a representative $Ne^+$ irradiated nanoplanet; (b) model target built one the base of TEM images and derived structural data; (c) local field modulus $|\mathbf{E}|$ map calculated on a nearly equatorial plane at the plasmon $\lambda \sim 466$ nm wavelength. Field wavevector and electric vector are as described in Fig.5.4.

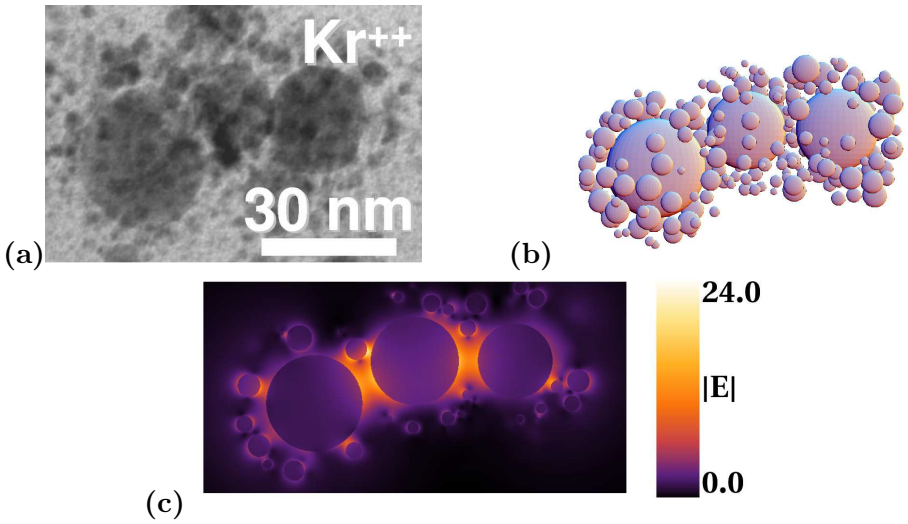


Figure 5.6.: (a) TEM image of a representative $Kr^{++}$ irradiated nanoplanet ensemble; (b) model target built one the base of TEM images and derived structural data; (c) local field modulus $|\mathbf{E}|$ map calculated on a nearly equatorial plane at the parallel plasmon $\lambda \sim 512$ nm wavelength. Field wavevector and electric vector are as described in Fig.5.4.

into account. We shall focus on local electromagnetic configuration at the resonance corresponding to parallel polarization states, since it has already been shown that higher enhancements are obtained for this kind of field configurations [6]. The assumed target of Fig.5.6(b) consists of three nanoplanets whose interaction is bridged by bigger satellites located at the satellite halos intersection. Local-field is calculated at 512 nm, with field oscillation parallel to the multimer principal axis. Figure 5.6(c) shows again that field enhancement is mainly localized at the interparticle gaps: the most significative difference with the previous cases is that clusters of closer dimensions provide a stronger coupling than observed before, reaching enhancement factors as high as $|\mathbf{E}| \sim 25$. Field localization is comparable with larger satellite sizes, while hot-spots at the junction between smaller satellites and central clusters are still present.

In order to fully elucidate the coupling mechanism between central and satellite clusters close-up of the local-field hot-spots are reported in Fig.5.7 for all the irradiated samples. It is evident that field patterns match closely the one seen for the symmetric silver and gold dimers (Ch.3), with the difference that the locally involved dimers are strongly asymmetric. Moreover Fig.5.7(c) effectively outlines the role of larger satellites in bridging the electromagnetic interaction between neighboring nanoplanets. One may argue if such a mechanism is present also in the samples irradiated with lighter ions: the fact that simulated spectra slightly underestimate peak width and wavelength may indeed be an indications that such a mechanism is present also in the former cases, nevertheless the reduced satellite size is unable to trigger the splitting of parallel and normal plasmon bands. Therefore we believe that the proposed description fully highlights the physical processes underlying the modification on nanoplanet plasmon bands.

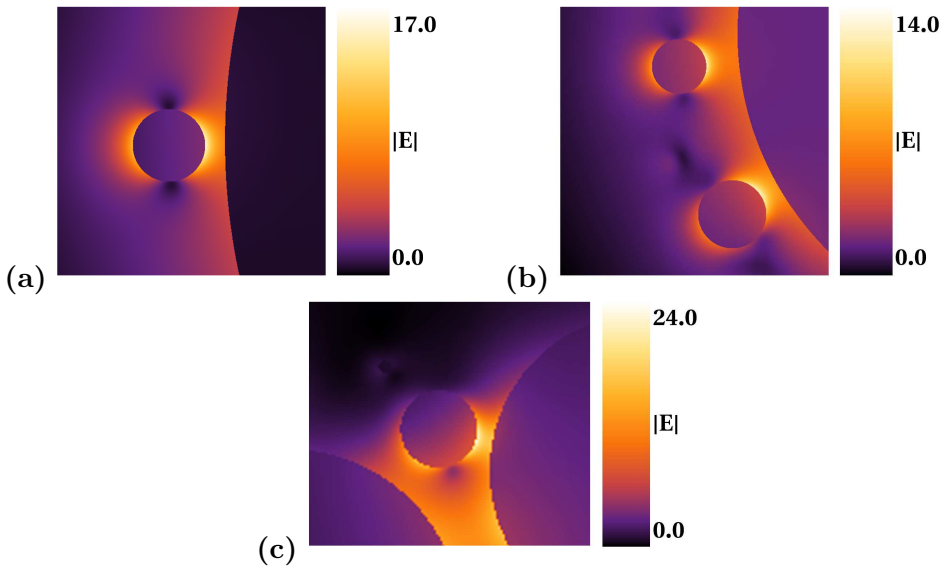


Figure 5.7.: Local field modulus $|\mathbf{E}|$ close-up maps for (a) $He^{+}$, (b) $Ne^{+}$ and (c) $Kr^{++}$ irradiated samples.

## 5.4. Conclusions

Far- and local-field optical properties of alloy nanoplanets obtained by ion beam processing have been described in the framework of two different theoretical approaches, i.e. the Hybrid core-shell Mie effective medium approach and the fully interacting GMM theory, which was expressively developed for this purpose. Their combined application allowed to deduced the following conclusions:

- overall extinction properties of alloy nanoplanets are triggered by the coupling between the central clusters and the satellite halos, with the exception of the $Kr^{++}$ irradiated sample, where coupling between neighboring nanoplanets must be taken into account in order to reproduce the observed spectral features;

- far-field properties of $He^{+}$ and $Ne^{+}$ irradiated samples are explained by taking into account a simple dipolar coupling, as it is shown by the quantitative agreement between the MMG and GMM approaches. Moreover GMM extinction spectra already converge in dipolar approximation.

- local-field hot-spots are always present in the satellite cluster halo, nevertheless only the larger hot-spots in the $Kr^{++}$ sample are able to influence significantly the overall far-field distribution, by triggering the coupling between neighboring nanoplanets;

- slight underestimation of peak width and position in $He^{+}$ and $Ne^{+}$ cases might be and indication that interplanetary coupling is also present in the light ion irradiated samples. Though this effect is neglected since overall spectral features are anyway correctly modeled.

It will be of course of great interest to investigate the optical properties of pure Ag and Au nanoplanets embedded in suitable matrices, in order to maximize plasmonic features of such attractive structures: this kind of calculations will be performed in the next chapter.

# 6. Local-field enhancement optimization in metallic nanoplanets

## 6.1. Introduction

Recently much effort has been devoted to the synthesis of new and exotic plasmonic nanostructures with useful and interesting far- and local-field properties: to name but a few we mention self-similar nanoparticle chains [9], nanoshell dimers [62], nanorice structures [86], gold and silver ellipsoids [6; 87] and nanoparticle linear chains and dimers [4; 88]. Alloy nanoplanets have proved to be a very interesting plasmonic nanostructures, given their plasmon tuning and far-field enhancement properties. Moreover the synthesis process is characterized by great flexibility which allows to carefully tailor nanoplanet compositional and topological properties .

To further optimize the nanoplanet topology in view of enhanced optical properties, in this chapter far- and local-field properties of model AuAg nanoplanets are compared with the ones of Ag structures with identical geometries. Silver is chosen for its excellent plasmonic properties and therefore as a suitable material to obtain large plasmon shifts and increase in local-field. Furthermore field enhancement properties are studied as a function of typical geometrical parameters such as satellite dimension and position, in order to assess the optimal structural conditions.

Comparison and local-field optimization are performed in two separate steps:

- as it was noted in Ch.5, alloy nanoplanets locally behave as nanoparticle dimers, with the peculiar characteristic that nanoparticle of different dimension are involved. For this reason strongly asymmetric dimers are chosen as test model systems to study the local-field properties of metallic nanoplanets. Optical properties will be studied as a function of satellite dimension and polarization state of the incident light, in order to analyze the effect of the free electron damping and the incident beam state;

- Plasmon tuning and field enhancement properties of alloy and pure Ag nanoplanets will be then investigated. In order to better visualize the local-field state multiple $|\mathbf{E}|$ plots on different nanoplanet sections other than the equatorial plane will be reproduced.

## 6.2. Local-field tuning in strongly asymmetric dimer

Local topological configurations in the nanoplanet satellite halo closely resemble the nanoparticle dimers described in Ch.2, with the distinction of a marked size

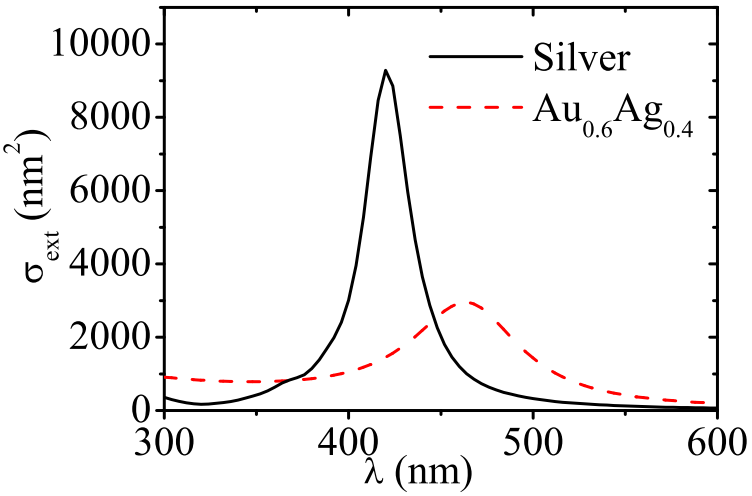


Figure 6.1.: Extinction properties of representative alloy and silver dimers: far-field spectra are essentially identical to the ones of the larger isolated cluster.

asymmetry. Therefore strongly asymmetric dimers are adopted as ideal model structures in order to investigate and optimize optical properties of metallic nanoplanets.

The first investigated structures are AuAg asymmetric dimers strongly related to the experimental systems treated in the former chapter. The larger dimer sphere of is set to be $D = 30$ nm in size, while for the satellites varying $D_{\mathrm{Sat}} = 2$ nm, $D_{\mathrm{Sat}} = 4$ nm and $D_{\mathrm{Sat}} = 6$ nm diameters are chosen in order to assess the effect of free electron damping on far and local optical properties; the interparticle gap is always $g = 1$ nm. Regarding the pair composition $Au_{0.6}Ag_{0.4}$ and $Au_{0.75}Ag_{0.25}$ alloys are adopted for the large and small cluster respectively, in agreement with TEM-EDS compositional data, with the corresponding dielectric functions corrected for the reduce electron mean free path. The host matrix refractive index set to be $n_m = 1.5$. A unitary amplitude linearly polarized plane wave illuminates the particle pair, moving along the cluster reference frame $z$ axis: three different polarization state are adopted, i.e. parallel, normal, and oblique at $\theta = 45°$ with respect to the dimer principal axis. This choice allows to better evaluate nanoplanet optical properties since in such a system local dimer configurations are randomly oriented with respect to the incident wave.

Figure 6.1 reports extinction spectra for two typical AuAg and silver asymmetric dimers. Extinction properties are essentially identical to the one of the isolated larger clusters, since the presence of the satellite is not able to modify the global far-field pattern. For this reason we are allowed to compute local-field maps at a fixed wavelength, which corresponds to the plasmon resonance, regardless of the satellite sizes and incident plane wave polarization state. In practice local-fields are computed at $\lambda = 464$ nm for the alloy systems and at $\lambda = 420$ nm in the case of silver.

Local-field modulus $|\mathbf{E}|$ plots for alloy dimers are reported in Fig.6.2, Fig.6.3 and Fig.6.4 in the case of $D_{\mathrm{Sat}} = 2$ nm, $D_{\mathrm{Sat}} = 4$ nm and $D_{\mathrm{Sat}} = 6$ nm satellite

diameters respectively. Plots are computed on the $z = 0$ equatorial plane at the plasmon wavelength, and as much as 25 multipoles are included in order to bring calculations to convergence.

As it may be expected, maximum field enhancements are obtained for parallel polarization illumination in all the three model systems ($|\mathbf{E}| \sim 21$ for the $D_{\mathrm{Sat}} = 6$ nm satellite). Likewise improved light intensities are seen at the dimer junctions if larger satellites are considered, since free electron damping mechanism are clearly more effective if reduced dimensions are involved. It is now extremely interesting to discuss field intensity distributions as a function of the incident wave polarization. First it may be noted that parallel polarization field distributions match the patterns observed in the former chapters. Surprisingly a similar situation is found in the $\theta = 45°$ polarization case, even if a largely different configuration might be expected. Along with the intensity pattern also a similar enhancement can be seen ($|\mathbf{E}| \sim 16$ for the $D_{\mathrm{Sat}} = 6$ nm satellite). This findings may be explained with the fact that displaced charges of opposite sign are still able to face at the junction given the small interparticle spacing, thus building up a large local-field with a distribution closely related to the one of the parallel case. The normal polarization case is totally different from the former two. For smaller satellites field distribution and intensities are analogue to the ones observed in the single particle situation [83], while in the third case a peculiar field map may be observed (Fig6.4(c)), with a large intensity drop exactly in the middle of the gap. This phenomenon has already been observed and attributed to the interference of plasmon waves traveling on the sphere surfaces [61].

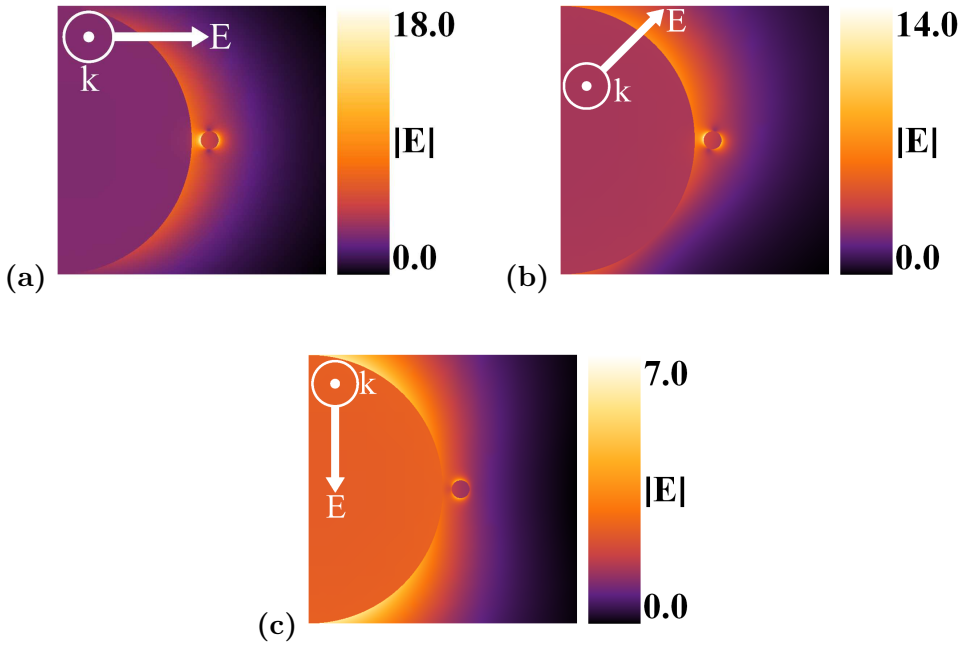


Figure 6.2.: $|\mathbf{E}|$ plots for the $D = 30$ nm, $D_{\mathrm{Sat}} = 1$ nm, $g = 1$ nm AuAg asymmetric dimer: (a) incident field polarization parallel to dimer principal axis, (b) incident field polarization at 45° with respect to dimer principal axis, (c) incident field polarization normal to dimer principal axis.

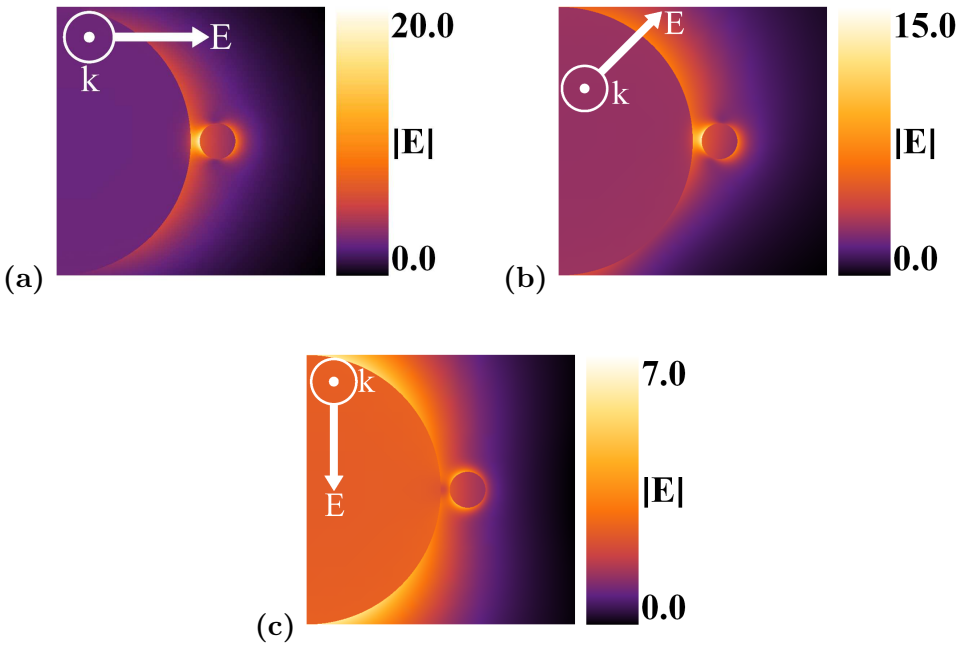


Figure 6.3.: $|\mathbf{E}|$ plots for the $D = 30$ nm, $D_{\mathrm{Sat}} = 2$ nm, $g = 1$ nm AuAg asymmetric dimer: (a) incident field polarization parallel to dimer principal axis, (b) incident field polarization at 45° with respect to dimer principal axis, (c) incident field polarization normal to dimer principal axis.

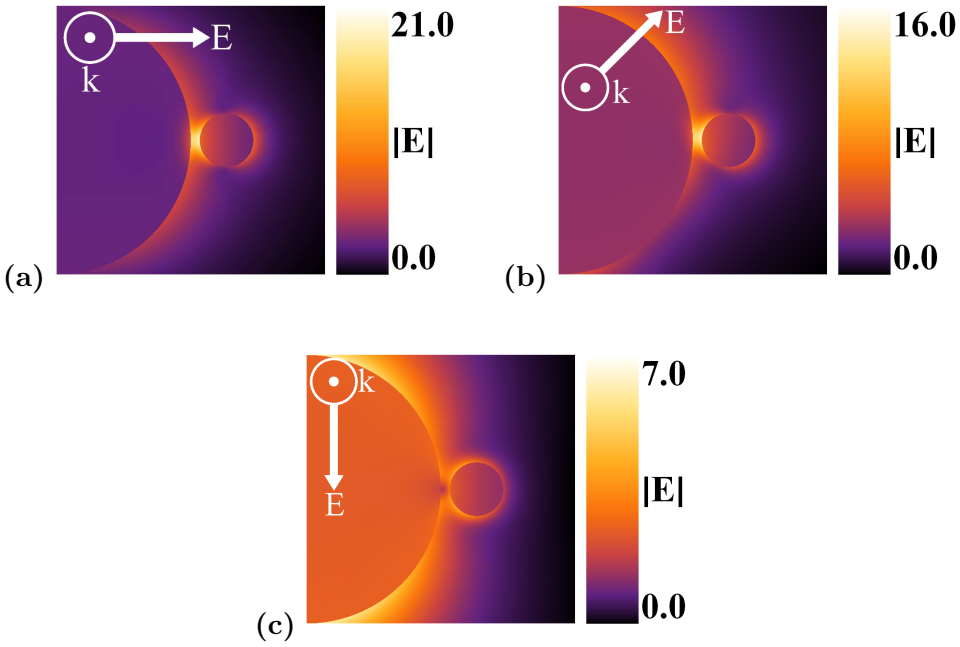


Figure 6.4.: $|\mathbf{E}|$ plots for the $D = 30$ nm, $D_{\mathrm{Sat}} = 3$ nm, $g = 1$ nm AuAg asymmetric dimer: (a) incident field polarization parallel to dimer principal axis, (b) incident field polarization at 45° with respect to dimer principal axis, (c) incident field polarization normal to dimer principal axis.

Identical model targets are utilized for the silver asymmetric dimers. Likewise local-field plots follow exactly the conventions adopted above, with the exception of the computation wavelength which is now $\lambda = 420$ nm, i.e. the position of dipolar resonance peak for a $D = 30$ nm silver particle embedded in a $n_m = 1.45$ silica matrix.

Fig.6.5, Fig.6.6 and Fig.6.7 report local-field modulus $|\mathbf{E}|$ maps for satellite of increasing dimensions.

Larger field intensities are again observed in the case of parallel polarizations, with enhancements one order of magnitude higher than the ones found in the alloy structures. If the $D_{\mathrm{Sat}} = 6$ nm satellite dimer is considered local-fields as high as $|\mathbf{E}| \sim 180$ are present at the junction, with just a $|\mathbf{E}| \sim 21$ local-field visible in the corresponding alloy system. If oblique incidence is considered the silver structures behave accordingly to what has been observed in the AuAg particle pairs, with intensities similar to the ones observed for the parallel polarization state. Likewise interference phenomena are observable when the incident plane wave is normally polarized with respect to the dimer principal axes, but this time better silver plasmonic properties allows the interference build-up even in the $D_{\mathrm{Sat}} = 4$ nm satellite case.

From this rough analysis it is clear that plasmonic properties of silver nanoplanets would be probably much more appealing that the alloy nanoplanet ones, since along with larger local-field enhancement strong plasmon tuning properties are probably present.

Given the higher potential interest of these structures a systematic analysis

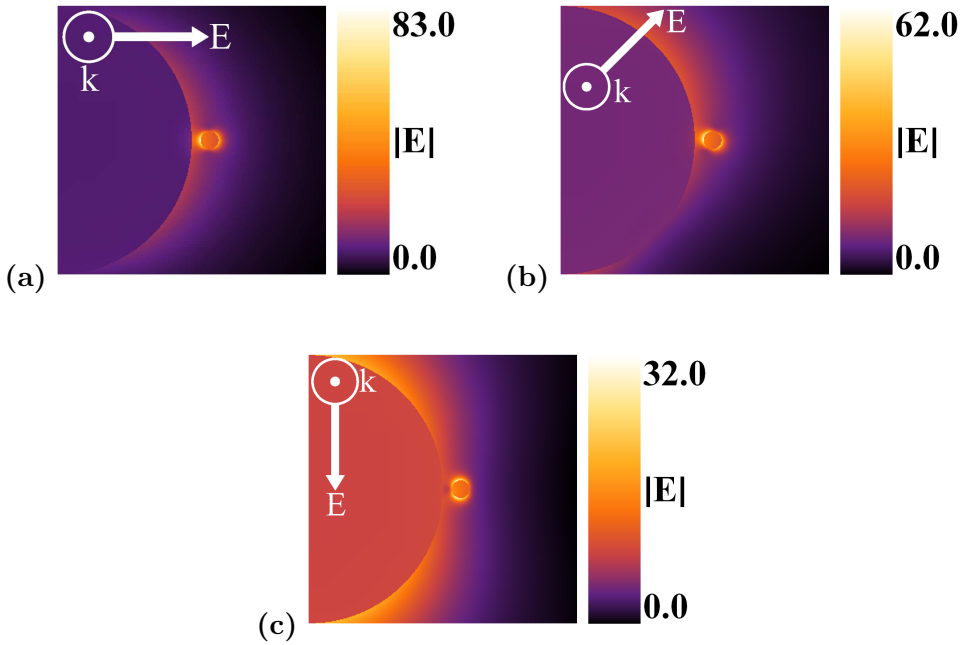


Figure 6.5.: $|\mathbf{E}|$ plots for the $D = 30$ nm, $D_{\mathrm{Sat}} = 1$ nm, $g = 1$ nm Ag asymmetric dimer: (a) incident field polarization parallel to dimer principal axis, (b) incident field polarization at 45° with respect to dimer principal axis, (c) incident field polarization normal to dimer principal axis.

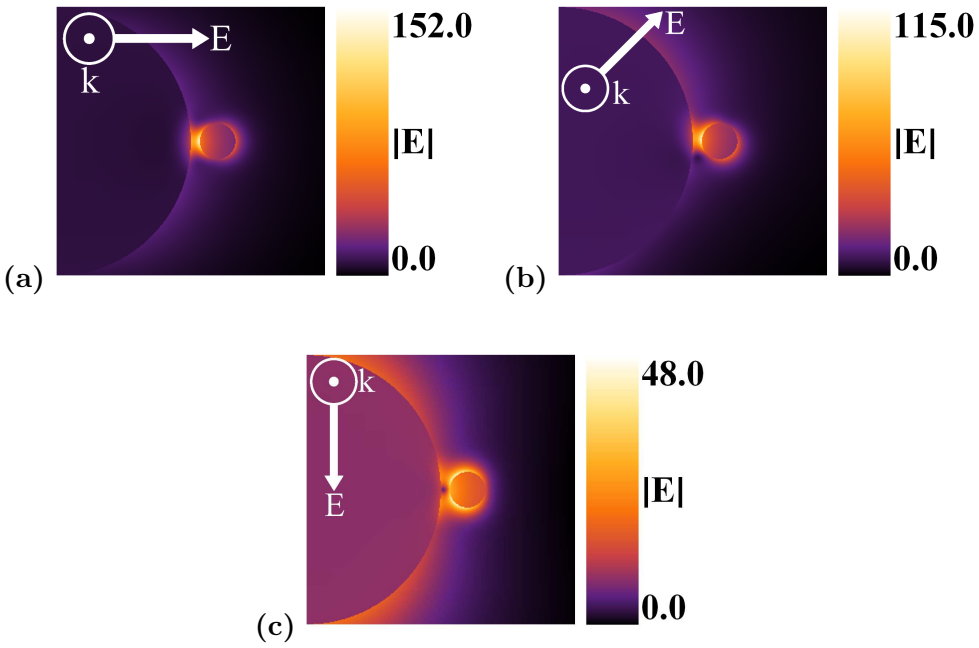


Figure 6.6.: $|\mathbf{E}|$ plots for the $D = 30$ nm, $D_{\mathrm{Sat}} = 2$ nm, $g = 1$ nm Ag asymmetric dimer: (a) incident field polarization parallel to dimer principal axis, (b) incident field polarization at 45° with respect to dimer principal axis, (c) incident field polarization normal to dimer principal axis.

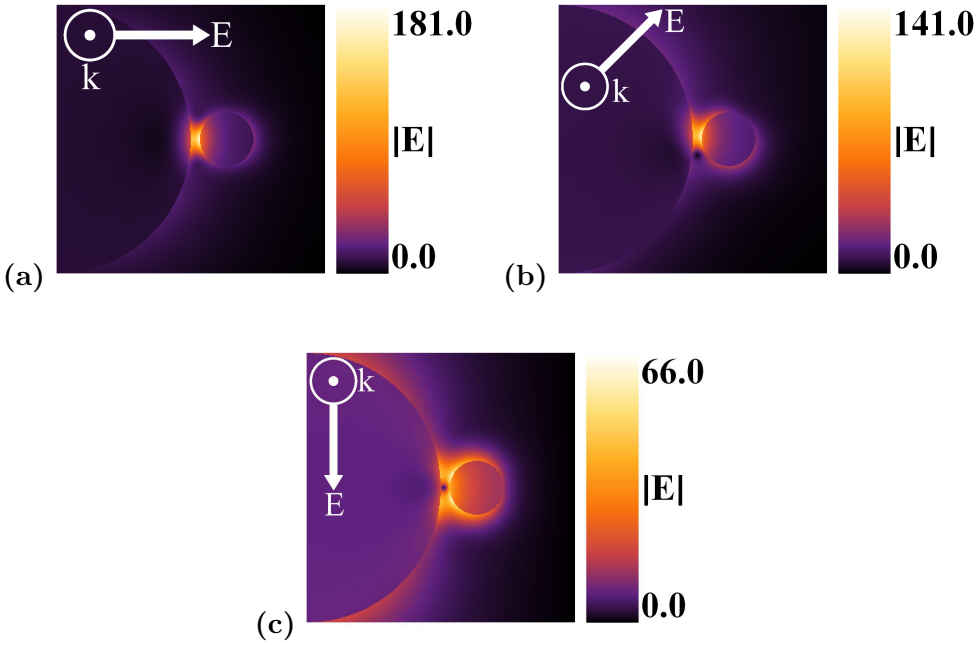


Figure 6.7.: $|\mathbf{E}|$ plots for the $D = 30$ nm, $D_{\mathrm{Sat}} = 3$ nm, $g = 1$ nm Ag asymmetric dimer: (a) incident field polarization parallel to dimer principal axis, (b) incident field polarization at 45° with respect to dimer principal axis, (c) incident field polarization normal to dimer principal axis.

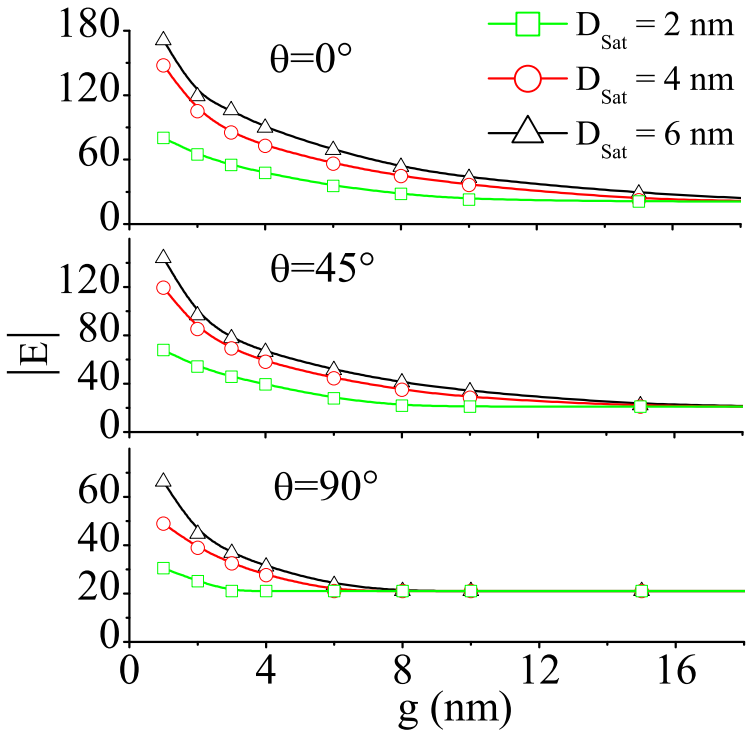


Figure 6.8.: Maximum field enhancement vs. interparticle distance plots for different incident field polarizations and satellite sizes. Asymptotic enhancement value for large gaps correspond to a single particle local-field enhancement for a $D = 30$ nm silver cluster.

of silver asymmetric dimer local-field properties has been carried out. Variable parameters are satellite size and distance from the mother cluster and incident field polarization. Figure 6.8 confirms that general trends agree with the particular observation performed above. The field intensity decreases with increasing distances, decreasing satellite dimensions and for polarizations different from the parallel one as expected, but within the 4 nm distance is greater than the $|\mathbf{E}| \sim 20$ limiting value, corresponding to the single mother cluster enhancement. The dependence on satellite size is mostly due to the electron mean free path reduction [54], while distance and polarization effects are simply attributable to a weaker interparticle coupling. As a final remark it is worth noting that particle coupling results in a significant field penetration in the satellites, with enhancements as high as $|\mathbf{E}| \sim 30$ in the sphere center.

## 6.3. Local-field enhancement in metallic nanoplanets

Once investigated the role of structural and compositional parameters on the local-field configuration of strongly asymmetric dimers, GMM theory is now applied to nanostructures which are closely related to the synthesized systems. Nanoplanets are peculiar nanoparticle ensembles obtained by keV ion irradiation of metallic nanocluster synthesized by ion beam processing, with procedure

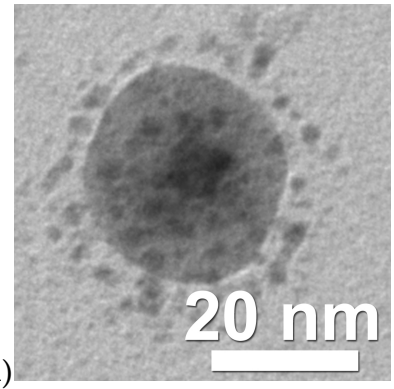


(a)

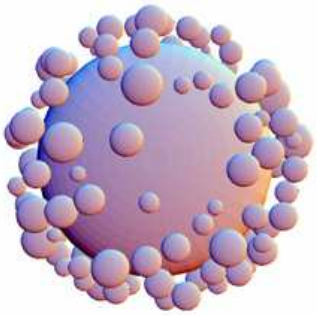

(b)

Figure 6.9.: Representative nanoplanet TEM image and model target build on the base of images and derived structural information.

which are reported in detail in Ref.[7; 8; 89]. Satellite cluster parameters such as number, dimension and distance from the central cluster surface can be tailored by varying ion irradiation conditions, i.e., current density, fluence and mass of the irradiating ion, and along with the satellite arrangement plasmonic properties of the system are significantly modified by the electromagnetic interparticle coupling. Details of the influence of synthesis parameters on $Au_xAg_{1-x}$ alloy nanoplanets, as well as effects on the plasmonic properties, have already been discussed in detail in the former chapter. Now a model target is built on the base of TEM images and derived structural information with a central cluster of 30 nm in diameter, and a roughly gaussian satellite size distribution, centered at $\langle d_{\mathrm{Sat}} \rangle = 3.2$ nm with $\sigma_{d_{\mathrm{Sat}}} = 0.4$ nm (Fig.6.9). Following the approach adopted for the asymmetric particle pairs, we chose two different compositions and host matrices for the systems to be studied: nanoplanets alloy composition is identical to the one adopted for the samples in Ch.2 and for the dimers in

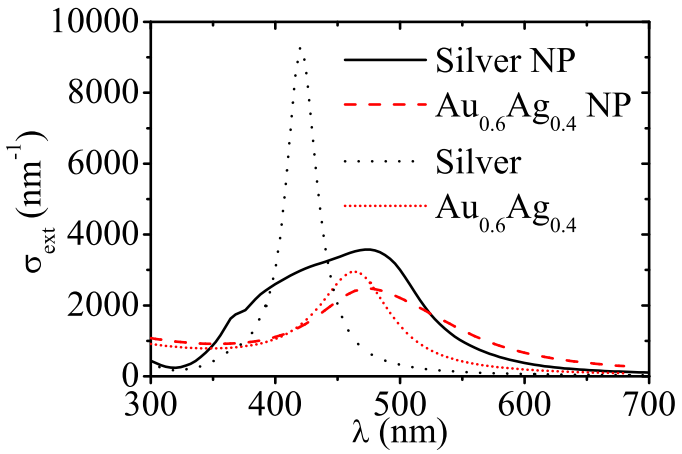


Figure 6.10.: Extinction spectra for AuAg and Silver nanoplanets illuminated by unpolarized light. Single particle spectra are reported for comparison (dotted lines)

Sec.6.2 with a $n_m = 1.5$ dielectric matrix, and the same is done for the silver structure in the $SiO_2$ host. Likewise structural parameters are identical for both systems, so that effects of different compositions are clearly visible.

Figure 6.10 reports extinction spectra for AuAg and pure silver nanoplanets, with single particle spectra included for comparison. Plasmon redshift and damping may be noted for both models, nevertheless much lager effects are seen

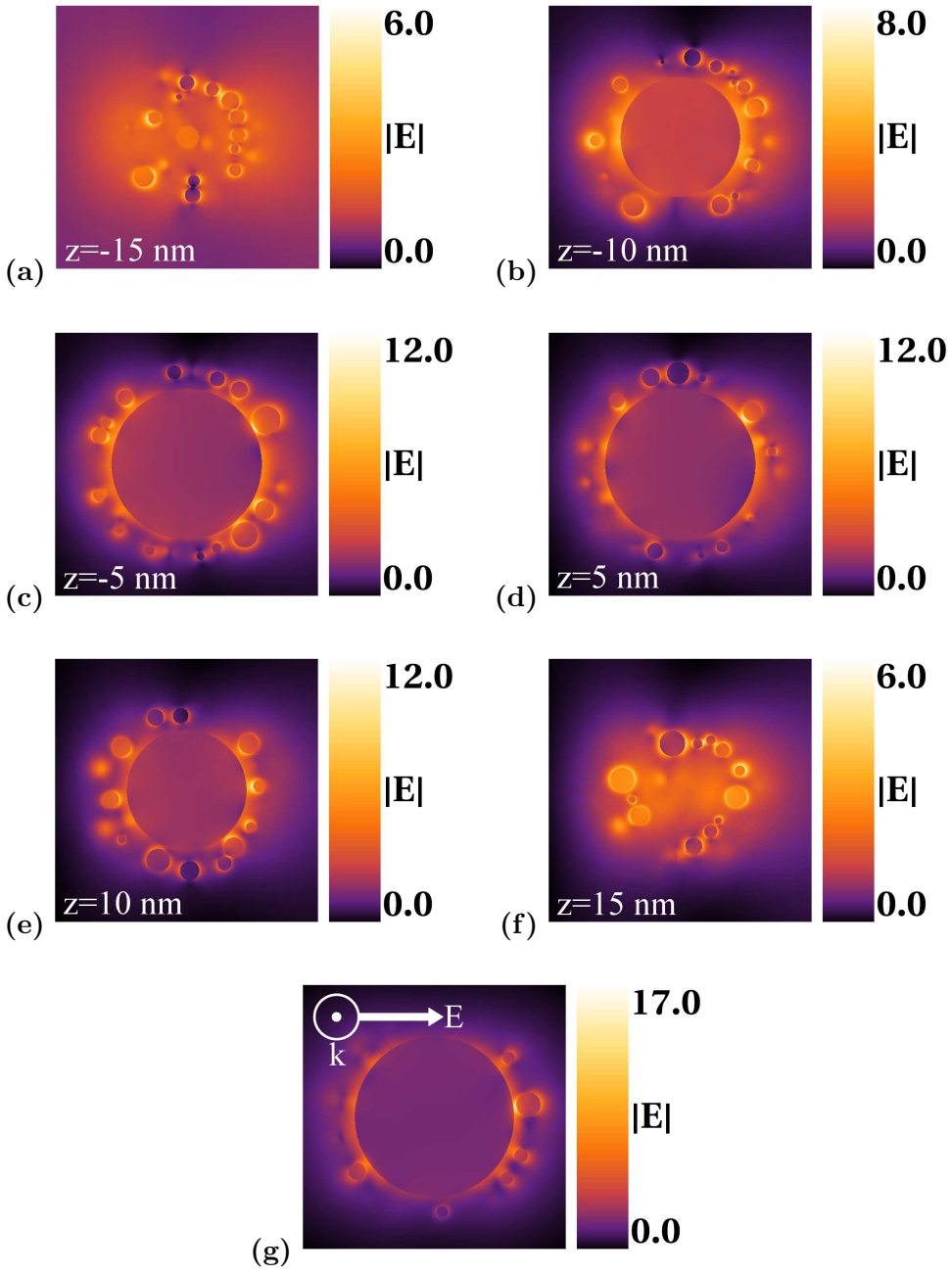


Figure 6.11.: Alloy $|\mathbf{E}|$ plots for different plane cuts along the $z$ axis. Field polarization and propagation direction always as in (g), which reports the equatorial plot.

for the silver system, given its better plasmonic properties. Alloy structure resonance redshift amounts to about 10 nm, while the one of Ag structure is almost 5 times larger, with peaks shifting from 464 nm to 476 nm and from 420 nm to 472 nm respectively. As it was already noted large resonance displacements are a clear indications of strong field enhancement and focusing, therefore large intensities are expected in the case of silver case, accordingly to what observed

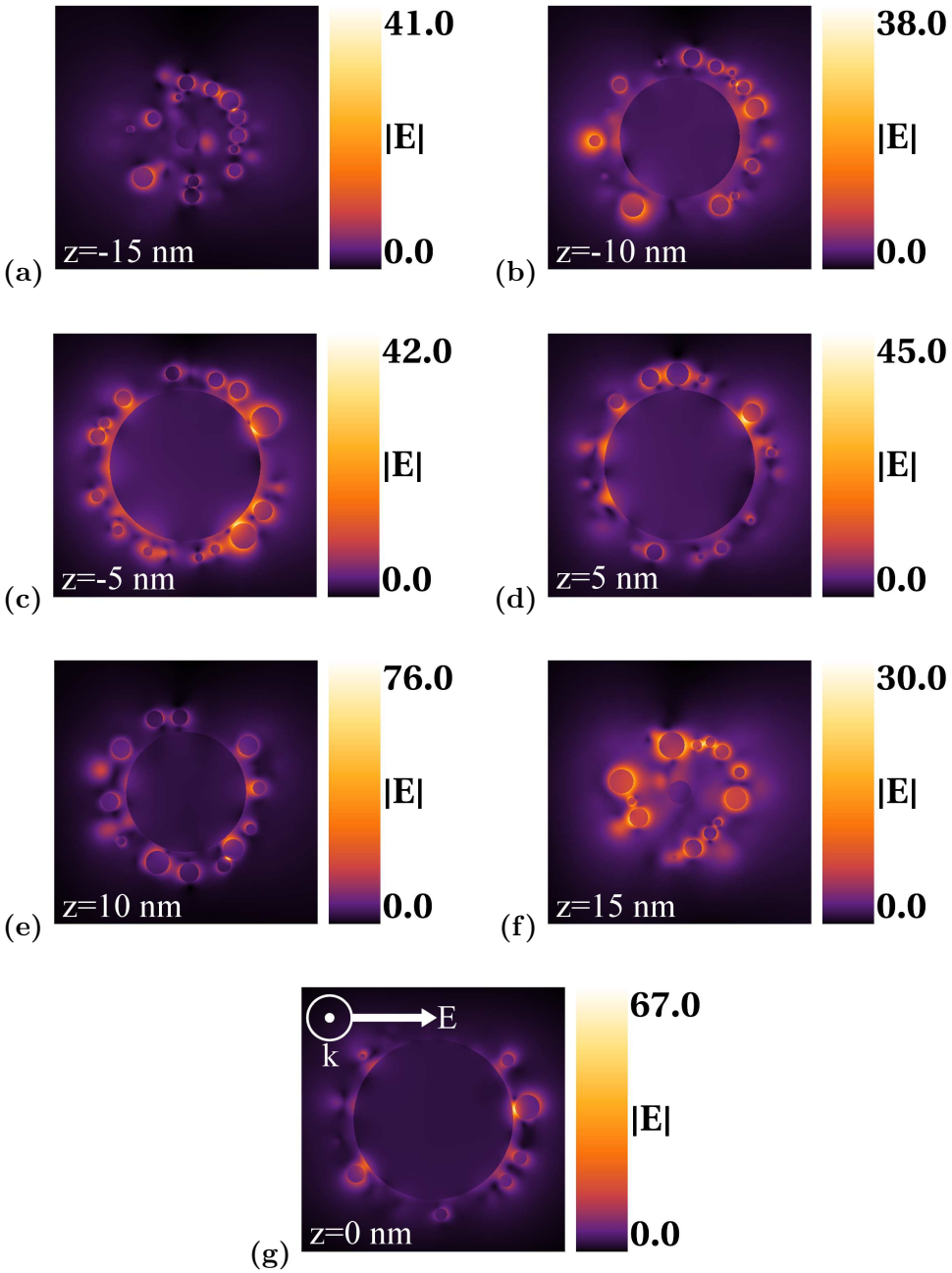


Figure 6.12.: Silver $|\mathbf{E}|$ plots for different plane cuts along the $z$ axis. Field polarization and propagation direction always as in (g), which reports the equatorial plot.

in the dimer model systems.

It would be of great interest to be provided with a wider view on nanoplanet local-field patterns, therefore in this occasion map computations are not limited to the $z = 0$ equatorial plane, but multiple cuts along the $z$ axis are taken so as to get a more general understanding of the field distribution. Figures 6.11 and 6.12 report these plots which give a comprehensive idea of the field intensity configuration in the satellite halo. Besides the expected enhancement differences between the alloy and Ag structures, it is worth noting that multiple field hot-spots are present in the whole satellite clouds. Strong coupling is found between the mother cluster and the satellites (Fig.6.12(g)), but also between the satellites themselves (Fig.6.12(e)), with enhancements factor as high as $\sim 80$ in the silver case. Nevertheless it must be underlined that in any situation intensities found in asymmetric dimers are at least twice higher than the ones seen in nanoplanets, and this is probably because of the global effect of the satellite halo which greatly contributes to the plasmon damping as is seen in the far-field spectrum (Fig.6.10). Such a wealth of closely spaced field hot-spots is anyway promising for the synthesis of high third order $\chi^{(3)}$ non-linear materials.

## 6.4. Conclusions

Local-field properties of metallic nanoplanets were systematically investigated as a function of their structural and compositional parameters. Strongly asymmetric dimers were chosen as preliminary model systems in order to assess the effect of light polarization state and satellite distance, composition and dimension on the local-field enhancements performances. Then field intensities and pattern of representative nanoplanets with different composition where thoroughly analyzed by performing field mapping along all the nanoplanet extension. After these investigations the following results have been established:

- as expected silver is the best performing material from the point of view of field enhancement properties. Asymmetric dimer calculations show that better performances are obtained for close interparticle spacings as already seen in chapter 2. Satellites of smaller dimensions suffer strong free electron damping, therefore synthesis conditions must be optimized so as to obtain sizes in the $D_{\mathrm{Sat}} \sim 6$ nm range if not larger;
- large field enhancements are seen in non optimal illumination conditions and even for normally polarized incident plane waves. This is an unexpected result if compared to what was found in Ch.2.
- field enhancement is less strong in nanoplanets than in asymmetric dimers, probably for damping effects attributable to the whole satellite halo. Nevertheless extensive field mapping showed that multiple field hot-spots characterized by large enhancements are present throughout the whole cluster extension.

Finally nanoplanets are extremely promising structures for plasmonic applications, especially if silver structures will be readily synthesizable.

# Part III.

# Multiple coupled cluster plasmonic nanoantennae

# 7. Plasmonic nanoantennae in the GMM framework

## 7.1. Introduction

Modification of emitter recombination rates by coupling with the external electromagnetic environment is a subject which has received a great deal of attention in particular since the early work of Purcell [90]. Recently much attention has been drawn by plasmonic nanoantennae, i.e by metal nanoparticle aggregates which are employed as devices to convert localized radiation into free propagating one. Nanoantennae may be used with different aims among which modification of emitter radiative and non-radiative recombination rates ($\gamma_r$, $\gamma_{nr}$) and quantum efficiency $q$ are probably the most important ones. Along with a very rich experimental literature [91–97], many different theoretical approaches including finite-difference time-domain (FDTD) calculations, boundary element method (BEM), multiple multipole (MMP) method and effective wavelength scaling have been adopted in order to design efficient optical nanoantennae [35; 36; 95; 98]. In the present chapter GMM theoretical framework is modified in order to be applied to a multisphere nanoantenna problem. In particular we are interest in nanoantenna mediated efficiency enhancement, since this is a problem of great technologically importance. The chapter is structured as follows:

- the antenna emitter problem is treated in the context of classical electrodynamics, following the approach outlined by Ruppin [99]. GMM approach is integrated within this context and important parameters such as modified quantum efficiency and recombination rates are computed as a function of quantities which are readily calculated in the multisphere approach;

- the modified theory is applied to an isolated silver sphere emitter structure. Emitter quantum efficiency $q$ and recombination rates are studied as a function of system parameters like sphere diameter and emitter orientation and distance from the antenna;

- GMM theory is then applied to silver dimer nanoantennae enclosing a dipole emitter exactly in the middle of their gap. Antenna performances are studied as a function of interparticle gap and emitter distance from the dimer principal axis. Variation of modified recombination rates are explored as functions of the particle gap as well.

## 7.2. Methods: GMM framework and the multisphere nanoantenna problem

The lifetime of an excited emitter near a spherical metallic nanoparticle is a peculiar and relatively simple problem to tackle, yet its solutions allows to draw general useful conclusion which may be naturally extended to the multisphere situation. The problem may be solved just by classical electrodynamic theory, where the emitter is described as a classical oscillating dipole. In this framework the modified radiative decay rate $\gamma_r$ is obtained by integrating the energy flow over a surface which encloses both the emitter and the nanoantennae. The nonradiative contribution $\gamma_{nr}$ instead is obtained by calculating the power dissipated inside the antenna. If $\gamma_{r,0}$ and $\gamma_{nr,0}$ are the isolated emitter radiative and nonradiative decay rates, then normalized modified values may be expressed as [99]:

$$\frac{\gamma_r}{\gamma_{r,0}} = \frac{W_r^{na}}{W_{r,0}}, \qquad \frac{\gamma_{abs}}{\gamma_{r,0}} = \frac{W_{abs}^{na}}{W_{r,0}}, \qquad \frac{\gamma_{nr}}{\gamma_{r,0}} = \frac{\gamma_{abs} + \gamma_{nr,0}}{\gamma_{r,0}} \tag{7.1}$$

where $W_r^{na}$ is the power radiated by the dipole antenna ensemble, $W_{abs}^{na}$ is the power dissipated inside the antenna, $W_{r,0}$ is the power radiated by the unperturbed dipole and $\gamma_{abs}$ is the antenna contribution to the nonradiative recombination rate. By knowing that the intrinsic quantum efficiency of an emitter may be written like $q_0 = \gamma_{r,0}/(\gamma_{r,0} + \gamma_{nr,0})$ [100], it can be easily shown that the modified yield is finally expressed as [100]:

$$q = \frac{\gamma_r/\gamma_{r,0}}{\gamma_r/\gamma_{r,0} + \gamma_{abs}/\gamma_{r,0} + (1-q_0)/q_0}. \tag{7.2}$$

Generalized Multiparticle Mie theory can be integrated in this classical electrodynamic approach by introducing minor modifications to its structure and to its software implementation, with the procedure given below successfully applied in practical calculations:

- as a first step a noble metal multisphere nanoantenna is created. The antenna may be composed by an arbitrary number of spheres just as all the systems described throughout this thesis;
- the dipole emitter is modeled as a small dielectric sphere. The sphere size $D^{dip}$ must me chosen so that it is much smaller than all the other spheres and so that its diameter is much smaller than the distance from each of the spheres composing the antenna.
- *only* the dielectric sphere is illuminated by a unitary amplitude linearly polarized plane wave. Provided that the above conditions are fulfilled the sphere behaves like and oscillating dipole whose dipole moment is [2]:

$$\mathbf{p} = 4\pi\varepsilon \left(\frac{\varepsilon_r - 1}{\varepsilon_r + 2}\right) (a^{dip})^3 \hat{\mathbf{e}}_{\mathbf{E}}, \tag{7.3}$$

  where $\varepsilon_r$ is the relative dielectric constant of the sphere and $\hat{\mathbf{e}}_{\mathbf{E}}$ is the unitary vector parallel to the field polarization. The dipole sphere is not

excited by the fields scattered by the multisphere antenna, and this is accomplished in practice by setting to zero the appropriate vector translation coefficients.

- at this point the only radiation source perceived by the nanoantenna is constituted by the oscillating dipole, therefore only the radiated powers reported in Eq.(7.1) need to be computed. It is now straightforward to understand that $W_r^{na} = W_{\text{sca}}$ and $W_{abs}^{na} = W_{\text{abs}}$, where $W_{r,0}$ is just the power radiated by a classical dipole [101], and $W_{\text{abs}}$ and $W_{\text{sca}}$ are the sphere ensemble (i.e. nanoantenna) absorbed and scattered powers defined in Ch.1.

- the last step consists in calculating the quantities $\gamma_r$, $\gamma_{nr}$ and $q$ by Eq.(7.1).

We are interested in investigating poor emitters quantum efficiency enhancement by plasmonic nanoantennae, therefore it will be set to $q_0 = 0.01$ for all the following calculations.

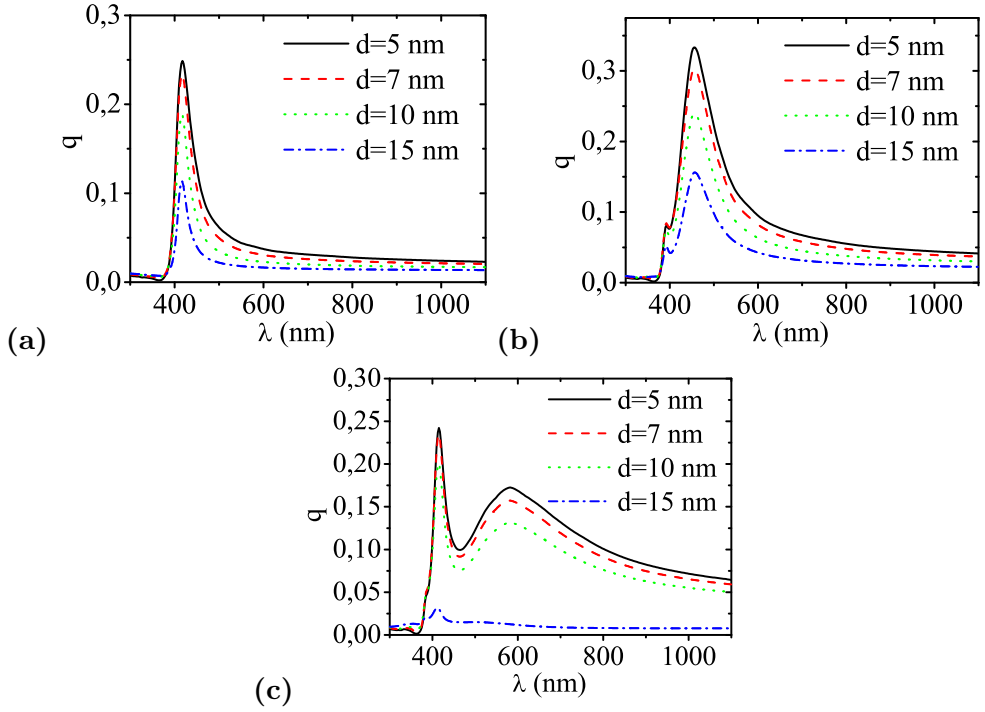


Figure 7.1.: Modified quantum efficiency vs $\lambda$ spectra for single sphere nanoantenna dipole systems, where $d$ stands for the sphere surface dipole separation, the dipole is normally oriented with respect to the sphere surface and sphere is made of silver:(a) $D = 30$ nm single sphere nanoantenna; (b) $D = 60$ nm single sphere nanoantenna; (c) $D = 100$ nm single sphere nanoantenna.

## 7.3. Application of GMM approach to the single spherical antenna problem

As mentioned before we are interested in nanoantennae as devices which are able to enhance the quantum efficiency $q$ of originally poor emitters. In order to design efficient light extracting structures we first investigate a simple Ag spherical nanoantenna system: silver is chosen for its better plasmonic properties with respect to other noble metals, while parameters such as antenna size and dipole position, orientation and emission wavelength are varied so as to envisage a strategy to maximize antenna performances. For practical calculations silver dielectric function is taken from the literature [53], while the host matrix refraction index is always set to be $n_m = 1.5$.

Figure 7.1 reports $q$ vs $\lambda$ spectra for spherical silver antennae whose sizes are $D = 30$ nm, $D = 60$ nm and $D = 100$ nm respectively. Spectra are calculated for different dipole antenna separations as reported in the figure, with the dipole normally oriented with respect to the sphere surface. In terms of general trends, antenna performances strongly depends on all the parameters included in the calculation, i.e antenna size and dipole position and emission wavelengths. Larger enhancements are obtained in correspondence of the isolated particle plasmon resonance and for dipoles placed closer to the sphere

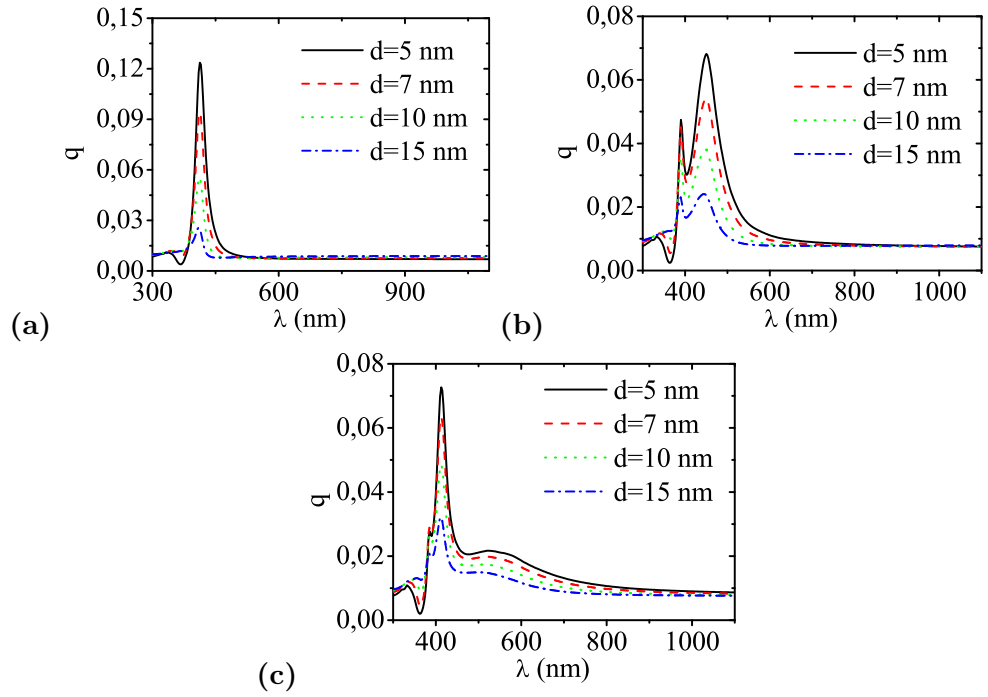


Figure 7.2.: Modified quantum efficiency vs $\lambda$ spectra for single sphere nanoantenna dipole systems, where $d$ stands for the sphere surface dipole separation, the dipole is parallel oriented with respect to the sphere surface and sphere is made of silver:(a) $D = 30$ nm single sphere nanoantenna; (b) $D = 60$ nm single sphere nanoantenna; (c) $D = 100$ nm single sphere nanoantenna.

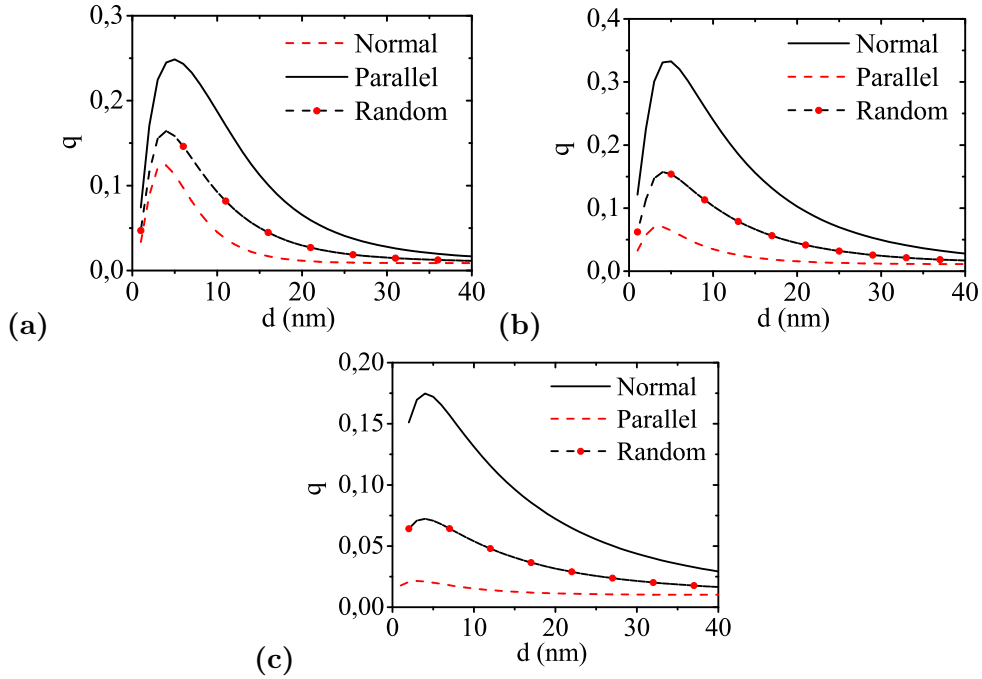


Figure 7.3.: Modified quantum efficiency vs $d$ spectra for single sphere nanoantenna dipole systems, where $d$ stands for the sphere surface dipole separation, and the sphere is made of silver. Spectra are calculated for normal, parallel and random orientation of the dipole, at the wavelength of maximum efficiency enhancement. (a) $D = 30$ nm single sphere nanoantenna at $\lambda = 418$ nm; (b) $D = 60$ nm single sphere nanoantenna at $\lambda = 458$ nm; (c) $D = 100$ nm single sphere nanoantenna at $\lambda = 590$.

surface, if separations up to 5 nm are considered. The $D = 60$ nm antenna is the best performing one (Fig.7.1(b)). This may be considered as the effect of the trade off between two different physical effects, i.e. the scattering efficiency of a given nanoantenna and the strength of its coupling with the corresponding emitting dipole: larger spheres ($D = 100$ nm) have better scattering efficiencies but smaller ones ($D = 30$ nm) couple more efficiently to the emitter outgoing radiation, therefore the $D = 60$ nm antenna turns out to be optimal choice. Starting from a $q_0 = 1\%$ emitter, efficiencies above 20% are obtained for all antenna dimensions, with enhancements larger than 30% in the $D = 60$ nm case. Enhancement bandwidth is again strongly related to the single particle plasmon shape [2]. Smaller particles are characterized by narrower plasmon resonances, and therefore by smaller enhancement bandwidth, while the $D = 100$ nm nanoantenna provides enhancements above 10% efficiency from 400 nm to 800 nm at worst. As a final remark it is worth noting that for the larger nanoantenna, and partially in the $D = 60$ nm case, an efficiency enhancement peak clearly attributable to particle quadrupolar modes may be seen around 400 nm.

Figure 7.2 reports $q$ vs $\lambda$ spectra for dipole antenna configurations identical to the one reported above, with the exception of dipole orientation, which is

now parallel to the sphere surface. It may be readily seen that the general enhancement feature outlined above are here reproduced, with a remarkable difference consisting in a much smaller overall efficiency enhancement, which amounts at most to $q \sim 10\%$. The above discussion clearly indicates that dipole orientation with respect to the nanoantenna must be considered as a major factor affecting the light extraction performances.

It is now interesting to give a closer look at the dependence of light extraction performance on the dipole nanoantenna separation. Figure 7.3 report $q$ vs $d$ spectra for all the three nanoantennae, where $d$ is the dipole antenna separation and the spectra are computed at the maximum enhancement wavelength. Quantum efficiency is reported for parallel and normally oriented dipoles as usual, moreover the efficiency enhancement for random orientation, which may be defined as [102]

$$q_r = \frac{q_{\parallel} + 2q_{\perp}}{3} \tag{7.4}$$

is also drawn. As before light extraction performances decrease as the dipole moves away from the sphere surface, with steeper variations for the smaller antennae. Quantum efficiency enhancement then reaches a maximum for dipole position roughly 5 nm away from the antenna surface, independently from the sphere size. For closer positions luminescence quenching appears since the emitter field couples with antenna nonradiative modes [99; 102].

This rapid analysis allows to determine ideal structural parameters for the construction of an efficient nanoantenna. The role of dipole orientation and distance from the antenna surface is elucidated, as well as the effect of sphere size on antenna efficiency and bandwidth. Therefore we are now able to model more complex multisphere antennae starting from the ideal parameter which were here figured out.

## 7.4. Application of GMM approach to the dimer nanoantennae

Dimer nanoantennae are a natural evolution of the single sphere ones and exhibit peculiar characteristics which make them ideal candidates to become extremely efficient light extraction devices. In fact under identical illumination conditions nanoparticle pairs show field enhancements at the junction which are much larger than the one revealed in isolated spheres. Using the reciprocity theorem [103], it may be argued that the emission of a dipole enclosed in the dimer junction could undergo a large enhancement with respect to the single particle case. Furthermore interparticle coupling shifts the dipole resonance toward the near infrared range, i.e. away from the range where noble metals such as silver and gold mostly exhibit their lossy behavior.

Figure 7.4 reports $q$ vs $\lambda$ spectra for a $q_0 = 0.01$ dipole coupled to silver dimer nanoantennae characterized by different interparticle gaps $g$. Consistently with what was found in the single sphere case, dimer sphere size is chosen to be $D = 60$ nm in order to maximize performances, with interparticle gaps $g$ ranging from 6 nm to 20 nm. The dipole is placed exactly in the middle of the dimer junction,

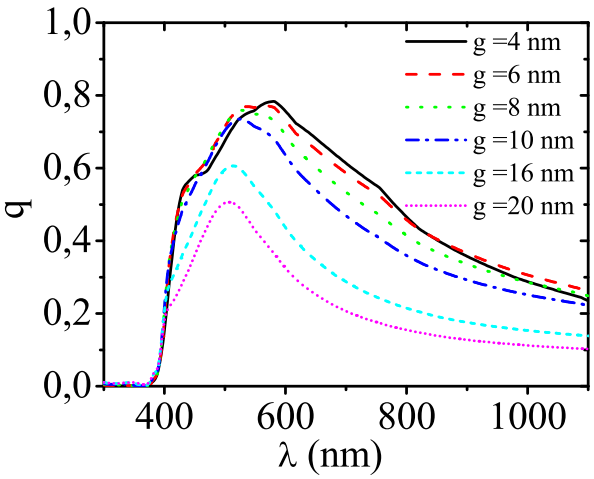


Figure 7.4.: Modified quantum efficiency vs $\lambda$ spectra for single dimer nanoantenna dipole systems, where $d$ stands for the dimer gap, the dipole is oriented parallel to the dimer principal axis, is equidistant from both the spheres and the dimer is made of silver. Dimer sphere diameter is chosen to be $D = 60$ nm

i.e. on the dimer principal axis and equally distant from the sphere surfaces, with its orientation parallel to the dimer principal axis. The silver dielectric function is taken from the literature [53] and the medium refractive index is chosen accordingly to what adopted in the single sphere case. The most evident feature of the present enhancement spectra is that quantum efficiencies much larger than in the single antenna system are obtained. The maximum attained efficiency increases as the interparticle gap drops with $q \sim 0.8$ in the case of the $g = 4$ nm and $g = 6$ nm interparticle spacings. From a practical standpoint it is also interesting to study quantum efficiency variations as a function of the dipole position, in particular when the dipole is displaced on a plane which is normal to the dimer principal axis and equidistant from both the spheres, with dipole orientation left untouched. To this purpose $(x, y)$ vs $q$ plots where performed, where $(x, y)$ represents the dipole position on the above described plane (point $(0, 0)$ is on the dimer axis), and $q$ is again the modified quantum efficiency. These plots are performed for dimers with different interparticle separations at the maximum excitation wavelength (Fig.7.4). Efficiency mappings performed on a 70 nm $\times$ 70 nm square and reported in Fig.7.5 exhibit the expected circular symmetry, with efficiencies above 0.1 even at the geometrical boundary of the dimer (the white circle in the figure). This feature is made even clearer by the radial efficiency plot reported in Fig.7.6, where it can also be noted that for smaller gaps ($g = 4$ nm , $g = 6$ nm) the maximum enhancement is outside the dimer principal axis, with quantum efficiencies larger that 0.8 seen 25 nm away from the dimer geometrical center. This fact is easily explained with what was observed in Sec.7.3, i.e. that for extremely small dipole antenna distances nonradiative modes become the dominating phenomenon and begin to quench the dipole radiation.

As a final analysis it is worth taking a look at the modification of radiative

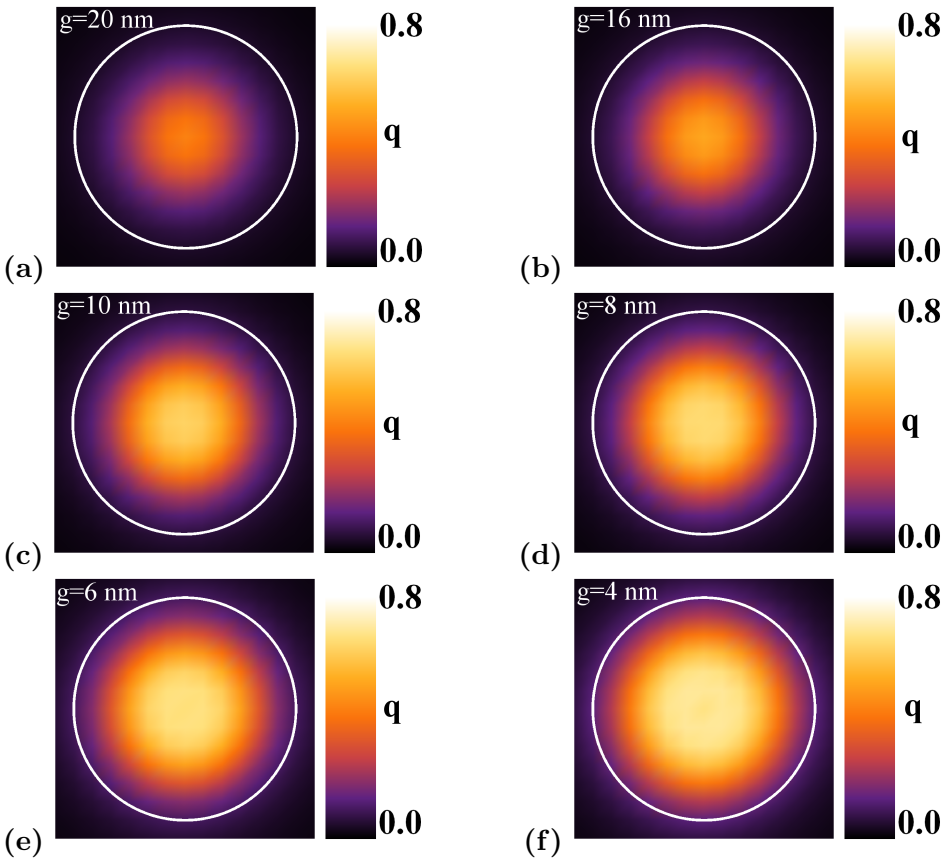


Figure 7.5.: Modified quantum efficiency mappings on a plane normal to the dimer principal axis and equidistant from both the spheres. Mapping is done on a 70 nm $\times$ 70 nm square at the maximum quantum efficiency wavelength for $D = 60$ nm dimers, where $g$ stands for the dimer gap. The white circle represents the sphere normal projection on the plane. (a) Mapping for the $g = 20$ nm dimer at $\lambda = 505$ nm; (b) Mapping for the $g = 16$ nm dimer at $\lambda = 512$ nm; (c) Mapping for the $g = 10$ nm dimer at $\lambda = 522$ nm; (d) Mapping for the $g = 8$ nm dimer at $\lambda = 530$ nm; (e) Mapping for the $g = 6$ nm dimer at $\lambda = 570$ nm; (f) Mapping for the $g = 4$ nm dimer at $\lambda = 580$ nm.

and nonradiative recombination rates induced by dimer nanoantennae. Even if we are mainly interested in efficiency enhancement, higher recombination rates in high efficiency emitters are also interesting from the point of view of light extraction, since pump saturation may be postponed and therefore higher intensities reached [15].

Figure 7.7 reports normalized radiative and nonradiative recombination rate spectra for two of the dipole antenna coupled systems described along this section, i.e for the $g = 20$ nm and the $g = 4$ nm dimer nanoantennae, where the dipole is locate in the middle of the gap as usual. In the case of $g = 20$ nm gap the radiative recombination rate $\gamma_r$ undergoes a 100-fold enhancement in correspondence of the antenna collective dipolar resonance, while a 400-fold enhancement is seen for the nonradiative rate $\gamma_{nr}$ in the blue region of the

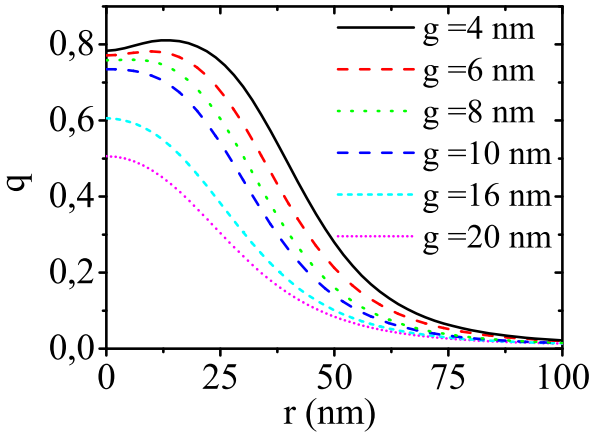


Figure 7.6.: Radial cuts of the mappings reported in Fig.7.5, where $g$ stands for the dimer gap, $r$ is the radial distance from the dimer principal axis and all the curves are computed at the maximum efficiency enhancement wavelength.

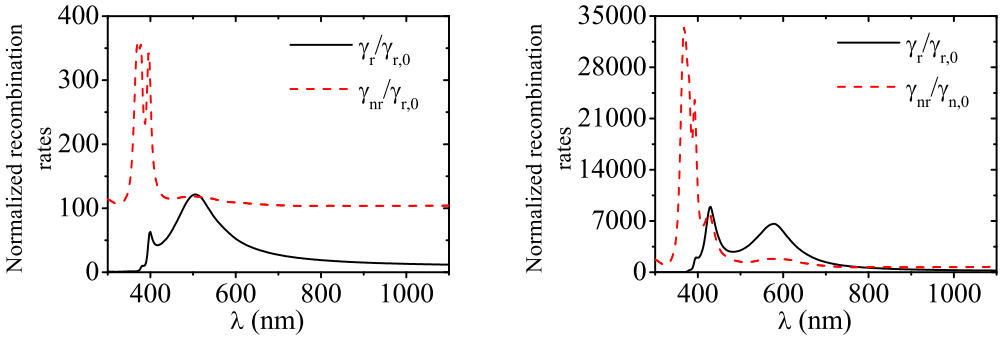


Figure 7.7.: Modified recombination rates vs $\lambda$ spectra for single dimer nanoantenna dipole systems, where $g$ stands for the dimer gap, the dipole is oriented parallel to the dimer principal axis, is equidistant from both the spheres and the dimer is made of silver. Dimer sphere diameter is chosen to be $D = 60$ nm

spectrum, where this effect is attributed to the activation of higher-order dark multipolar modes [102]. In the case of the non-radiative recombination rate a background is seen all along the spectrum: this is simply the effect of the initial $q_0 = 0.01$ quantum efficiency choice. If the closer gap nanoantenna is analyzed, enhancement of almost four orders of magnitude are detectable for the radiative recombination rates, and even larger ones are seen for the non radiative rates in the high energy regions, with all these effects simply attributable to a much stronger dipole antenna coupling [15].

## 7.5. Conclusions

Along this chapter Generalized Multiparticle Mie theory has been successfully applied to multisphere nanoantenna problem. GMM approach has been integrated in the classical electrodynamic framework which is commonly used to

study the single sphere antenna problem [99]. Then relevant physical quantities such as modified radiative and nonradiative recombination rates $\gamma_r$ and $\gamma_{nr}$ are calculated as functions of the sphere ensemble (i.e. nanoantenna) scattered and absorbed power, thus involving no additional computations with respect to the classical GMM solution.

The obtained theoretical tool has been first applied to single sphere nanoantenna systems. We have thus been able to optimize structural parameters such as antenna dimension and emitter spatial configuration so as to maximize light extraction performances.

Finally obtained optimized parameters are utilized to model efficiency enhancement properties of dimer nanoantennae. These structure have shown to provide 80-fold efficiency boosting in the case of low $q_0 = 0.01$ efficiency emitters, with increase of the radiative recombination rates up to 4 orders of magnitude.

# 8. Tunable efficiency enhancement via mixed plasmonic-photonic modes

## 8.1. Introduction

Employement of metal nanoparticles as optical nanoantennae, i.e. as devices that convert localized energy into free propagating radiation, is a subject which deserves great attention, as can be deduced from the results obtained in the previous chapter. Single molecule studies were performed to elucidate the influence on the spontaneous emission of parameters such as emitter orientation and distance with respect to a metal nanoparticle [95; 96; 104]. The effect of coupling between emitters and metallic structures with different shapes including ellipsoids, nanoshells and nanoparticle dimers was investigated as well [12; 91–93], showing that enhancement of molecule quantum efficiency can be achieved [91]. In spite of the great variety of employed geometries and materials, it must be underlined that a common nanoantenna feature is a strong broadband efficiency enhancement principally located in the near infrared range of the spectrum. This kinds of characteristic can also be seen in the dimer efficiency spectra reported in Ch.7.

In this chapter GMM theory is applied to study the modification of radiative recombination rate ($\gamma_r$) and quantum efficiency ($q$) of emitters coupled to periodic linear arrays of silver nanoparticles [16; 52]. These structures, which have been already treated in Ch.2, are known to support mixed photonic-plasmonic resonances characterized by narrow line shapes and strong position dependence on the geometrical parameters of the system [5; 29; 57; 58].

As a first step GMM approach is used to analyze the single building blocks of the linear arrays, i.e coupled systems constituted by the emitter, either close to a silver sphere surface or in the gap of a silver sphere dimer. Then the attention is switched to the arrays, and influence on the radiative properties of the emitter is studied as a function of system characteristics such as cell parameter and environment refractive index, where with cell parameter we intend the separation between building blocks, i.e. the isolated nanoantennae.

## 8.2. Light extraction properties of single building blocks

In order to provide a broad band plasmon resonance able to support diffractive modes over a wide range of wavelengths $D = 100$ nm spheres are chosen for the building block, be it an isolated sphere or a sphere dimer [2].

Fig.8.1 reports the $q$ vs $\lambda$ dependence for a dipole 10 nm away from the $D =$ 100 nm silver sphere, and normally oriented with respect to the sphere surface. Maximun enhancement is again obtained around the plasmon resonance with

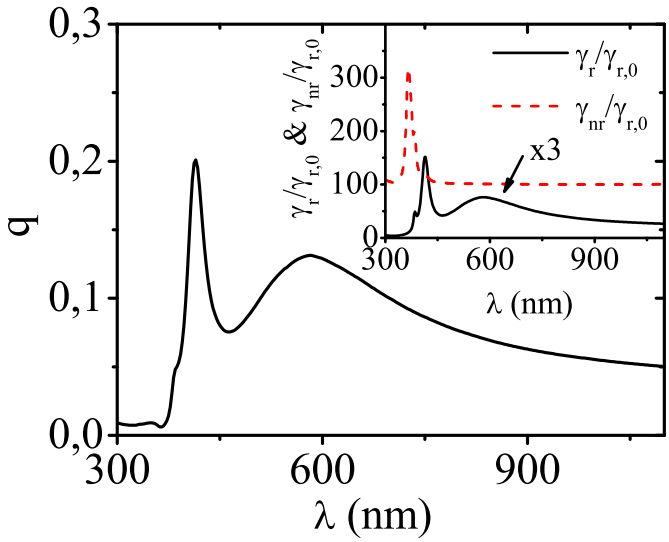


Figure 8.1.: Quantum efficiencies for the $D = 100$ nm sphere-emitter system in a $n = 1.5$ dielectric medium. Dipole sphere separation is set to be $d = 10$ nm with dipole orientation normal to the sphere surface. Normalized recombination rates are reported in the inset.

$q \sim 0.2$ as best efficiency. Radiative and non-radiative rates are reported in the inset: rates are again enhanced around the plasmon resonance, with non-radiative modes dominating the spectrum especially in the high energy range.

Fig.8.2 is the same for a $D = 100$ nm silver sphere dimer, enclosing an emitter in the middle of a 20 nm gap. Higher radiative recombination rates are obtained, with a maximum quantum efficiency around 50%, partially assignable to the larger spectral separation between the radiative dipolar mode and the higher order dark ones [93]. Common features of both structures are broad resonances and large quantum efficiency enhancement mainly located in the near-infrared range. We remark one more times that the above underlined feature are hardly controllable by varying antenna geometry and composition, therefore an orginal method must be devised in order to get a finer control over the antenna properties.

## 8.3. Light extraction via mixed plasmonic-photonic modes

The main idea of the proposed approach is to exploit collective plasmonic-photonic resonances of silver particle chains, in order to obtain tunable and wavelength selective recombination rate enhancement for emitters coupled to these metallic structures. Furthermore, driven by the fact that large field enhancement are obtained in the gap of nanoparticle dimers, we aim to combine local and collective effects so as to obtain better light extraction performances [15]. To this aim we now analyze linear chains constituted by the coupled sphere-emitter and dimer-emitter units described before: chain length is set to

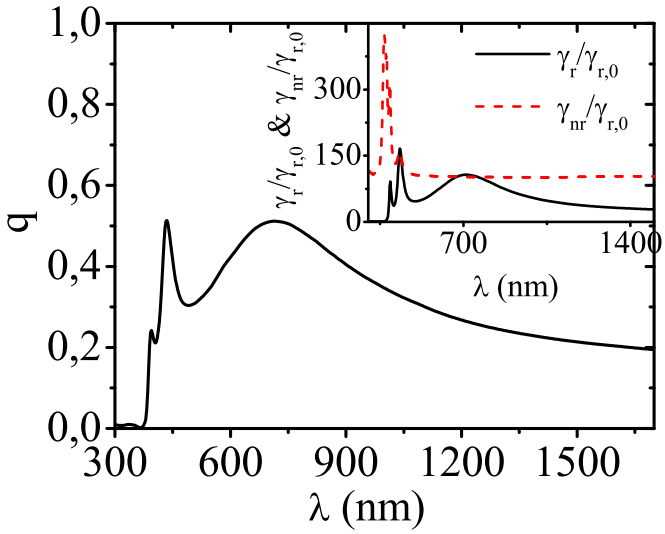


Figure 8.2.: Quantum efficiencies for the $D = 100$ nm dimer-emitter system in a $n = 1.5$ dielectric medium. Dipole sphere separation is set to be $d = 10$ nm for both the spheres with dipole orientation normal to the sphere surfaces and parallel to the dimer principal axis. Normalized recombination rates are reported in the inset.

be 600 unit cells (i.e 600 spheres or dimers) so as to assure the convergence of the mixed modes [58], and is normally oriented with respect to basis structure principal axis. Medium refractive index is set to be $n = 1.5$, optical constants for silver are obtained from Ref.[53], while cell parameter $a$ is varied between 500 and 800 nm. We emphasize the fact that convergence for all the spectra was checked against the number of included multipoles, thus taking into account all the active higher order non-radiative modes.

Fig.8.3 shows $q$ vs. $\lambda$ spectra for the sphere-emitter system. Without tackling the details of mixed-mode resonances supported by these structures, which are discussed elsewhere [5; 57], we first notice that large enhancement peaks manifest roughly at $\lambda \simeq a \cdot n$, where $a$ is the cell parameter and $n$ the medium refractive index, as might been expected. Resonances may show up in the spectrum as a peak or a dip, depending on the electromagnetic response of the single basis unit and on the resonance position itself, being larger for wavelengths around the maximum efficiency of the isolated unit structure. For $a = 500$ nm quantum efficiency enhancement of about two orders of magnitude is obtained, while larger cell parameters push the mixed-modes outside the isolated structure plasmon spectral region, thus causing a decrease in the intensity of the resonance peak [5]. We finally remark that for suitable cell parameters resonances of different orders are found in the spectrum.

Quantum efficiency spectra for dimer units are reported in Fig.8.4: while, for the effect of the different basis structure, resonance peaks present larger widths, it is clear that light extraction performances benefit of the cooperative action between local and collective resonance modes, allowing to get much larger spectral tunability and an 80-fold quantum efficiency enhancement, again for

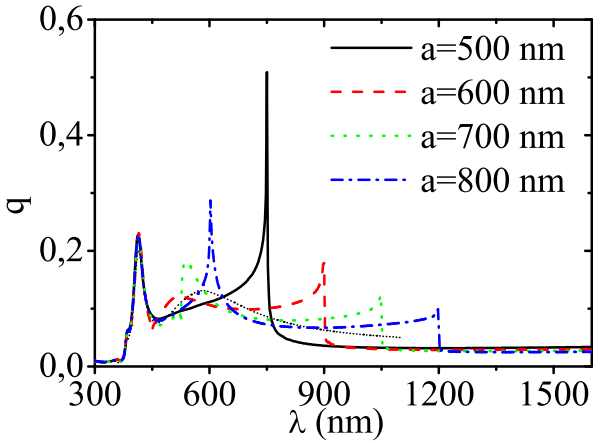


Figure 8.3.: Quantum efficiencies for the $D = 100$ nm dimer-emitter chains in a $n = 1.5$ dielectric medium. Dipole sphere separation is set to be $d = 10$ nm with dipole orientation normal to the sphere surfaces. Chain length is set to be 600 spheres.

$a = 500$ nm cell parameter. In the present case, the much broader dimer plasmon resonance allows to obtain large efficiency enhancements even in the near-infrared range.

A further idea which can be explored is the possibility to tune the resonance position by changing the medium refractive index. Fig.8.5(a) reports $q$ vs. $\lambda$ spectra for a $a = 500$ nm sphere-emitter chain, embedded in a transparent matrix with refractive index ranging from $n = 1.0$ to $n = 2.0$. By exploiting the sensitivity of the mixed-mode resonance to the dielectric environment, it is possible to displace the efficiency enhancement peak from the visible to the

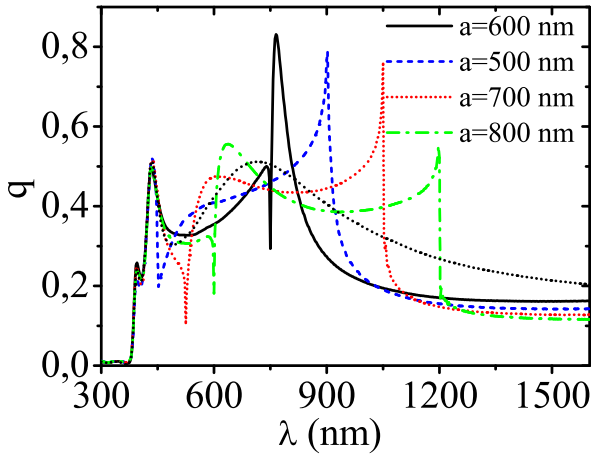


Figure 8.4.: Quantum efficiencies for the $D = 100$ nm dimer-emitter chain in a $n = 1.5$ dielectric medium. Dipole sphere separation is set to be $d = 10$ nm for both the spheres with dipole orientation normal to the sphere surfaces and parallel to the dimer principal axis. Chain length is set to be 600 dimers.

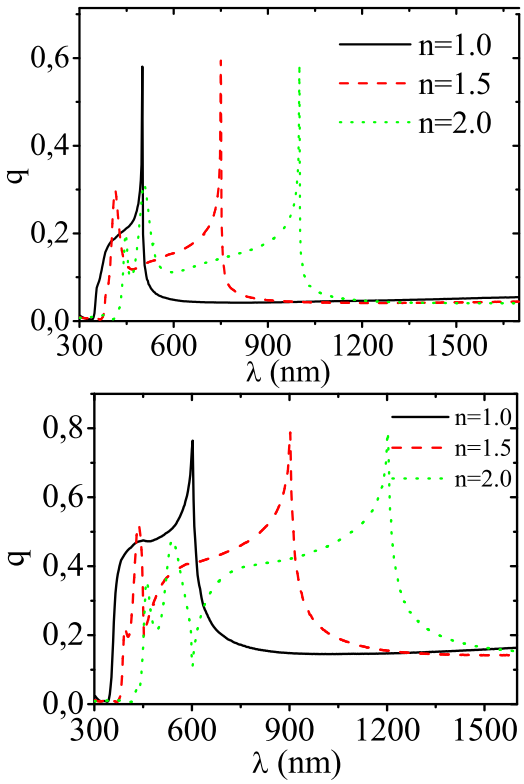


Figure 8.5.: Quantum efficiencies as a function of the medium variable refractive index:(a) $D = 100$ nm sphere-emitter chain with a $a = 500$ nm cell parameter. Dipole sphere separation is set to be $d = 10$ nm with dipole orientation normal to the sphere surfaces. Chain length is set to be 600 spheres. (b) $D = 100$ nm dimer-emitter chain in a $n = 1.5$ dielectric medium. Dipole sphere separation is set to be $d = 10$ nm for both the spheres with dipole orientation normal to the sphere surfaces and parallel to the dimer principal axis. Chain length is set to be 600 dimers.

infrared range. In the case of dimer chains Fig.8.5(b) shows that the larger flexibility of the mixed-modes supported by these structures allows to push the wavelength selective enhancement toward the relevant telecommunication range around 1.5 $\mu$m. It is possible indeed, by carefully choosing the system parameters, to obtain large quantum efficiencies (above 50%) in all the visible and near infrared spectrum, from 400 nm to 1.5 $\mu$m, even for bad $q_o \simeq 1\%$ emitters like the one here adopted. Better $q_o \simeq 10\%$ emitters could provide higher final efficiencies (above 90%), partially at the expenses of the resonance sharpness, as can be argued from the $q_o$ dependence in Eq.7.2.

## 8.4. Conclusions

In summary we have demonstrated tunable and wavelength selective recombination rate enhancement spanning the visible and near-infrared range, by

exploiting mixed plasmonic-photonic modes supported by metal nanoparticle chains. In the two analyzed cases extended coupled structures were more performing than the single building blocks, with isolated nanoantennae mainly characterized by broad resonances in the near-infrared range. Photonic structures showing sharp quantum efficiency peaks well above 50% also in the case of bad emitters in the blue-green range can be obtained. A careful exploration of free parameters such as antenna materials, interparticle spacing and metallic particle shapes could lead to structures with even better performances. The results here reported could be of great importance for light emitting and telecommunication devices, given the possibility to obtain high quantum efficiencies in the visible and near-infrared spectrum, and the fabrication amenability of these structures via conventional lithography techniques [105].

# Summary

Optical properties of nanocluster-based plasmonic materials were studied along this thesis by the Generalized Multiparticle Mie approach. Far- and local-field optical properties of basic plasmonic structures such as sphere dimers and chains were successfully analyzed as a function of their composition and their topological features.

The provided physical insight is then exploited in the modeling of strongly coupled complex structures obtained by ion beam processing. These systems were called nanoplanets since they are constituted by a large central cluster surrounded by small satellite ones very close to its surface. Nanoplanets show extremely interesting far- and local-field properties which may be carefully tailored by varying the ion beam synthesis conditions. GMM theory allowed to establish that the strong interparticle coupling is at the base of their peculiar optical features.

Finally multiple coupled cluster are proposed as efficient nanoantennae. Nanoparticle dimers were proved to provide extremely efficient broadband light extraction. If regular sphere array are used instead, broadband limitation imposed by isolated antennae may be overcome and tunable wavelength selective recombination rate enhancement is obtained.

Overall this thesis gives an interesting insight in the plasmonic properties of functional multiple coupled cluster nanostructures.

# Sommario

Le proprietà ottiche di strutture plamoniche nanostrutturate sono state studiate in questa tesi tramite l'applicazione della teoria generalizzata di Mie. Il campo ottico locale e lontano di strutture plasmoniche basilari come dimeri e catene di sfere è stato analizzato con successo in funzione delle caratteristiche composizionali e topologiche del sistema.

La comprensione dei sottostanti fenomeni fisici così ottenuta è stata poi sfruttata nella modellizzazione di strutture complesse fortemente accoppiate, ottenute per sintesi tramite impianto ionico. Questi sistemi sono stati chimati nanopianeti poiché sono costituiti da un grande cluster centrale circondato da piccoli cluster satelliti estremamente vicini alla sua superficie. I nanopianeti mostrano proprietà ottiche di campo lontano e vicino estremamente interessanti, che possono essere attentamente controllate variando le condizioni di sintesi e impianto. La teoria generalizzata di Mie ha permesso di stabilire che un forte accoppiamento elettromagnetico tra particelle è alla base delle loro interessanti proprieta ottiche.

Infine strutture di nanoparticelle accoppiate sono proposte come efficienti nanoantenne. Dimeri di nanoparticelle hanno dimostrato di fornire alte prestazioni per quel che riguarda l'estrazione di luce a larga banda. Se invece lunghe catene regolari di particelle vengono impiegate come nanoantenne, è possibile ottenere un aumento dei coefficienti di ricombinazione radiativa che sia selettivo per quel che riguarda la lunghezza d'onda, e facilmente controllabile per quel che riguarda la sua posizione.

Complessivamente questa tesi fornisce un'interessante introspettiva delle proprietà plasmoniche di strutture di nanocluster accoppiati.

# List of publications

List of the publications related to this thesis

- G. Mattei, V. Bello, P. Mazzoldi, G.Pellegrini, C. Sada, C. Maurizio and G. Battaglin, *Modification of composition and structure of bimetallic nanocluster in silica by ion beam irradiation*, Nucl. Instrum. Meth. B **240**, 128 (2007);

- G.Pellegrini, G. Mattei, V. Bello and P. Mazzoldi, *Interacting metal nanoparticles: Optical properties from nanoparticle dimers to core-satellite systems*, Mat. Sci. Eng. C **27**, 1347 (2007);

- G.Pellegrini, G. Mattei, V. Bello and P. Mazzoldi, *Local-field enhancement in metallic nanoplanets*, Mat. Sci. Eng. B (2007) **doi:10.1016/j.mseb/2007.09.060**;

- G.Pellegrini, G. Mattei, V. Bello and P. Mazzoldi, *Local-field enhancement and plasmon tuning in bimetallic nanoplanets*, Opt. Express **15**, 1097 (2007);

- G.Pellegrini, G. Mattei, and P. Mazzoldi, *tunable and wavelength selective recombination rate enhancement via mixed plasmonic-photonic modes*, submitted

# Bibliography


[1] C. F. Bohren and D. R. Huffman, *Absorption and Scattering of Light by Small Particles* (1983).

[2] U. Kreibig and M. Vollmer, *Optical properties of metal clusters* (Springer-Verlag, Berlin Heidelberg, 1995).

[3] G. Battaglin, P. Calvelli, E. Cattaruzza, F. Gonella, R. Polloni, G. Mattei, and P. Mazzoldi, "Z-scan study on the nonlinear refractive index of copper nanocluster composite silica glass," Appl. Phys. Lett. **78**, 3953 – 3955 (2001).

[4] L. A. Sweatlock, S. A. Maier, H. A. Atwater, J. J. Penninkhof, and A. Polman, "Highly confined electromagnetic fields in arrays of strongly coupled Ag nanoparticles," Phys. Rev. B **71**, 235408 (2005).

[5] S. L. Zou, N. Janel, and G. C. Schatz, "Silver nanoparticle array structures that produce remarkably narrow plasmon lineshapes," J. Chem. Phys. **120**, 10871 – 10875 (2004).

[6] J. J. Penninkhof, A. Polman, L. A. Sweatlock, S. A. Maier, H. A. Atwater, A. M. Vredenberg, and B. J. Kooi, "Mega-electron-volt ion beam induced anisotropic plasmon resonance of silver nanocrystals in glass," Appl. Phys. Lett. **83**, 4137 – 4139 (2003).

[7] V. Bello, G. De Marchi, C. Maurizio, G. Mattei, P. Mazzoldi, M. Parolin, and C. Sada, "Ion irradiation for controlling composition and structure of metal alloy nanoclusters in SiO2," J. Non-Cryst. Solids **345-46**, 685 – 688 (2004).

[8] G. Mattei, G. D. Marchi, C. Maurizio, P. Mazzoldi, C. Sada, V. Bello, and G. Battaglin, "Chemical- or radiation-assisted selective dealloying in bimetallic nanoclusters," Phys. Rev. Lett. **90**, 085502 (2003).

[9] K. R. Li, M. I. Stockman, and D. J. Bergman, "Self-similar chain of metal nanospheres as an efficient nanolens," Phys. Rev. Lett. **91**, 227402 (2003).

[10] C. Sönnichsen, B. Reinhard, J. Liphardt, and A. Alivisatos, "A molecular ruler based on plasmon coupling of single gold and silver nanoparticles," Nat. Biotech. **23**, 741–745 (2005).

[11] J. R. Krenn, A. Dereux, J. C. Weeber, E. Bourillot, Y. Lacroute, J. P. Goudonnet, G. Schider, W. Gotschy, A. Leitner, F. R. Aussenegg, and

C. Girard, "Squeezing the optical near-field zone by plasmon coupling of metallic nanoparticles," Phys. Rev. Lett. **82**, 2590 – 2593 (1999).

[12] F. Tam, G. P. Goodrich, B. R. Johnson, and N. J. Halas, "Plasmonic enhancement of molecular fluorescence," Nano Lett. **7**, 496 – 501 (2007).

[13] S. A. Maier, P. G. Kik, H. A. Atwater, S. Meltzer, E. Harel, B. E. Koel, and A. A. G. Requicha, "Local detection of electromagnetic energy transport below the diffraction limit in metal nanoparticle plasmon waveguides," Nat. Mater. **2**, 229 – 232 (2003).

[14] M. Quinten, A. Leitner, J. R. Krenn, and F. R. Aussenegg, "Electromagnetic energy transport via linear chains of silver nanoparticles," Opt. Lett. **23**, 1331 – 1333 (1998).

[15] L. Rogobete, F. Kaminski, M. Agio, and V. Sandoghdar, "Design of plasmonic nanoantennae for enhancing spontaneous emission," Opt. Lett. **32**, 1623 – 1625 (2007).

[16] R. Ruppin, "Decay of an excited molecule near a small metal sphere," J. Chem. Phys. **76**, 1681 – 1684 (1982).

[17] Y. L. Xu, "Electromagnetic scattering by an aggregate of spheres," Appl. Optics **34**, 4573 – 4588 (1995).

[18] S. A. Maier, M. L. Brongersma, P. G. Kik, S. Meltzer, A. A. G. Requicha, and H. A. Atwater, "Plasmonics - A route to nanoscale optical devices," Adv. Mater. **13**, 1501 (2001).

[19] H. A. Atwater, S. Maier, A. Polman, J. A. Dionne, and L. Sweatlock, "The new "p-n junction". Plasmonics enables photonic access to the nanoworld," MRS Bull. **30**, 385 – 389 (2005).

[20] S. A. Maier, "Plasmonics - Towards subwavelength optical devices," Curr. Nanosci. **1**, 17 – 23 (2005).

[21] S. A. Maier and H. A. Atwater, "Plasmonics: Localization and guiding of electromagnetic energy in metal/dielectric structures," J. Appl. Phys. **98**, 011101 (2005).

[22] S. A. Maier, "Plasmonics: Metal nanostructures for subwavelength photonic devices," IEEE J. Sel. Top. Quant. **12**, 1214 – 1220 (2006).

[23] S. A. Maier, "Plasmonics: The promise of highly integrated optical devices," IEEE J. Sel. Top. Quant. **12**, 1671 – 1677 (2006).

[24] R. Zia, J. A. Schuller, A. Chandran, and M. L. Brongersma, "Plasmonics: the next chip-scale technology," Materials Today **9**, 20 – 27 (2006).

[25] H. A. Atwater, "The promise of plasmonics," Sci. Am. **296**, 56 – 63 (2007).

[26] M. L. Brongersma, R. Zia, and J. A. Schuller, "Plasmonics - the missing link between nanoelectronics and microphotonics," Appl. Phys. A-Mater. **89**, 221 – 223 (2007).

[27] C. E. Talley, J. B. Jackson, C. Oubre, N. K. Grady, C. W. Hollars, S. M. Lane, T. R. Huser, P. Nordlander, and N. J. Halas, "Surface-enhanced Raman scattering from individual Au nanoparticles and nanoparticle dimer substrates," Nano Lett. **5**, 1569 – 1574 (2005).

[28] C. Oubre and P. Nordlander, "Optical properties of metallodielectric nanostructures calculated using the finite difference time domain method," J. Phys. Chem. B **108**, 17740 – 17747 (2004).

[29] S. L. Zou and G. C. Schatz, "Coupled plasmonic plasmon/photonic resonance effects in SERS," Top. Appl. Phys. **103**, 67 – 85 (2006).

[30] S. A. Maier, P. G. Kik, and H. A. Atwater, "Observation of coupled plasmon-polariton modes in Au nanoparticle chain waveguides of different lengths: Estimation of waveguide loss," Appl. Phys. Lett. **81**, 1714 – 1716 (2002).

[31] S. A. Maier, P. G. Kik, and H. A. Atwater, "Optical pulse propagation in metal nanoparticle chain waveguides," Phys. Rev. B **67**, 205402 (2003).

[32] M. L. Brongersma, J. W. Hartman, and H. A. Atwater, "Electromagnetic energy transfer and switching in nanoparticle chain arrays below the diffraction limit," Phys. Rev. B **62**, 16356 – 16359 (2000).

[33] S. A. Maier, M. L. Brongersma, and H. A. Atwater, "Electromagnetic energy transport along arrays of closely spaced metal rods as an analogue to plasmonic devices," Appl. Phys. Lett. **78**, 16 – 18 (2001).

[34] S. A. Maier, M. L. Brongersma, and H. A. Atwater, "Electromagnetic energy transport along Yagi arrays," Mat. Sci. Eng. C-Bio. S. **19**, 291 – 294 (2002).

[35] L. Novotny, "Effective wavelength scaling for optical antennas," Phys. Rev. Lett. **98**, 266802 (2007).

[36] S. Gerber, F. Reil, U. Hohenester, T. Schlagenhaufen, J. R. Krenn, and A. Leitner, "Tailoring light emission properties of fluorophores by coupling to resonance-tuned metallic nanostructures," Phys. Rev. B **75**, 073404 (2007).

[37] D. W. Mackowski, "Analysis of radiative scattering for multiple sphere configurations," P. Roy. Soc. Lond. A. Mat. **433**, 599 – 614 (1991).

[38] Y. L. Xu, "Fast evaluation of the Gaunt coefficients," Math. Comput. **65**, 1601 – 1612 (1996).

[39] Y. L. Xu, "Calculation of the addition coefficients in electromagnetic multisphere-scattering theory," J. Comput. Phys. **127**, 285 – 298 (1996).

[40] Y. L. Xu, "Calculation of the addition coefficients in electromagnetic multisphere-scattering theory (vol 127, pg 285, 1996)," J. Comput. Phys. **134**, 200 – 200 (1997).

[41] Y. L. Xu, "Fast evaluation of Gaunt coefficients: recursive approach," J. Comput. Appl. Math. **85**, 53 – 65 (1997).

[42] Y. L. Xu, "Efficient evaluation of vector translation coefficients in multiparticle light-scattering theories," J. Comput. Phys. **139**, 137 – 165 (1998).

[43] Y. L. Xu, "Electromagnetic scattering by an aggregate of spheres: far field," Appl. Optics **36**, 9496 – 9508 (1997).

[44] Y. L. Xu, B. A. S. Gustafson, F. Giovane, J. Blum, and S. Tehranian, "Calculation of the heat-source function in photophoresis of aggregated spheres," Phys. Rev. E **60**, 2347 – 2365 (1999).

[45] Y. L. Xu, B. A. S. Gustafson, F. Giovane, J. Blum, and S. Tehranian, "Calculation of the heat-source function in photophoresis of aggregated spheres (vol E 60, pg 2347, 1999)," Phys. Rev. E **6403**, 039903 (2001).

[46] Sleijpen G. L. G. and Fokkema D. R., "BiCGstab(ell) for linear Equations involgin unsymmetric matrices with complex spectrum," ETNA pp. 11 – 32 (1993).

[47] Y. L. Xu, "Electromagnetic scattering by an aggregate of spheres: asymmetry parameter," Phys. Lett. A **269**, 30 – 36 (1998).

[48] H. Du, "Mie-scattering calculation," Appl. Opt. **43**, 1951 (2004).

[49] A. R. Edmonds, *Angular momentum in quantum mechanics* (Princeton University Press, Princeton, 1957).

[50] R. Ruppin, "Effects of high-order multipoles on the extinction spectra of dispersive bispheres," Opt. Commun. **168**, 35 – 38 (1999).

[51] S. L. Zou and G. C. Schatz, "Narrow plasmonic/photonic extinction and scattering line shapes for one and two dimensional silver nanoparticle arrays," J. Chem. Phys. **121**, 12606 – 12612 (2004).

[52] G. Pellegrini, G. Mattei, V. Bello, and P. Mazzoldi, "Interacting metal nanoparticles: Optical properties from nanoparticle dimers to core-satellite systems," Mat. Sci. Eng. C-Bio. S. **27**, 1347 – 1350 (2007).

[53] P. B. Johnson and R. W. Christy, "Optical nonstants of noble metals," Phys. Rev. B **6**, 4370 (1972).

[54] H. Hovel, S. Fritz, A. Hilger, U. Kreibig, and M. Vollmer, "Width of cluster plasmon resonances - Bulk dielectric functions and chemical interface damping," Phys. Rev. B **48**, 18178 – 18188 (1993).

[55] P. Nordlander, C. Oubre, E. Prodan, K. Li, and M. I. Stockman, "Plasmon hybridizaton in nanoparticle dimers," Nano Lett. **4**, 899 – 903 (2004).

[56] E. M. Hicks, S. L. Zou, G. C. Schatz, K. G. Spears, R. P. Van Duyne, L. Gunnarsson, T. Rindzevicius, B. Kasemo, and M. Kall, "Controlling plasmon line shapes through diffractive coupling in linear arrays of cylindrical nanoparticles fabricated by electron beam lithography," Nano Lett. **5**, 1065 – 1070 (2005).

[57] S. L. Zou and G. C. Schatz, "Response to "Comment on 'Silver nanoparticle array structures that produce remarkable narrow plasmon line shapes' " [J. Chem. Phys. 120, 10871 (2004)]," J. Chem. Phys. **122**, 097102 (2005).

[58] S. L. Zou and G. C. Schatz, "Theoretical studies of plasmon resonances in one-dimensional nanoparticle chains: narrow lineshapes with tunable widths," Nanotechnology **17**, 2813 – 2820 (2006).

[59] A. F. Koenderink, J. V. Hernandez, F. Robicheaux, L. D. Noordam, and A. Polman, "Programmable nanolithography with plasmon nanoparticle arrays," Nano Lett. **7**, 745 – 749 (2007).

[60] R. de Waele, A. F. Koenderink, and A. Polman, "Tunable nanoscale localization of energy on plasmon particle arrays," Nano Lett. **7**, 2004 – 2008 (2007).

[61] S. E. Sburlan, L. A. Blanco, and M. Nieto-Vesperinas, "Plasmon excitation in sets of nanoscale cylinders and spheres," Phys. Rev. B **73**, 035403 (2006).

[62] C. Oubre and P. Nordlander, "Finite-difference time-domain studies of the optical properties of nanoshell dimers," J. Phys. Chem. B **109**, 10042 – 10051 (2005).

[63] L. Gunnarsson, T. Rindzevicius, J. Prikulis, B. Kasemo, M. Kall, S. L. Zou, and G. C. Schatz, "Confined plasmons in nanofabricated single silver particle pairs: Experimental observations of strong interparticle interactions," J. Phys. Chem. B **109**, 1079 – 1087 (2005).

[64] Z. P. Li, Z. L. Yang, and H. X. Xu, "Comment on "Self-similar chain of metal nanospheres as an efficient nanolens"," Phys. Rev. Lett. **97**, 079701 (2006).

[65] G. Battaglin, Nucl.Instr.Meth.B **116**, 102 (1996).

[66] E. Cattaruzza, Nucl.Instr.Meth.B **169**, 141 (2000).

[67] F. Gonella and P. Mazzoldi, *Handbook of nanostructured Materials and Nanotechnology*, vol. 4 (Academic Press, San Diego, 2000).

[68] G. Mattei, "Alloy nanoclusters in dielectric matrix," Nucl. Instrum. Meth. B **191**, 323 – 332 (2002).

[69] G. Mattei, G. De Marchi, C. Maurizio, P. Mazzoldi, C. Sada, V. Bello, and G. Battaglin, Phys. Rev. Lett. **90**, 085502–1–4 (2003).

[70] F. Gonella, G. Mattei, P. Mazzoldi, C. Sada, G. Battaglin, and E. Cattaruzza, Appl. Phys. Lett. **75**, 55 (1999).

[71] C. de Julian Fernandez, C. Sangregorio, G. Mattei, C. Battaglin, F. Gonella, A. Lascialfari, S. Lo Russo, D. Gatteschi, P. Mazzoldi, and J. Gonzalez, Nucl.Instr.Meth.B **479**, 4249 (2001).

[72] P. Mazzoldi, G. Arnold, G. Battaglin, F. Gonella, and R. Haglund, Nonlin. Opt. Phys. Mat. **5**, 285 (1996).

[73] G. Mattei, V. Bello, G. Battaglin, G. De Marchi, C. Maurizio, P. Mazzoldi, M. Parolin, and C. Sada, J. Non-Cryst. Solids **322**, 17 (2003).

[74] L. Thome, J. Jagielski, G. Rizza, F. Garrido, and J. Pivin, Appl.Phys.A **66**, 327 (1998).

[75] J. Pivin, Mat.Sci.and Eng. A **293**, 30 (2000).

[76] R. Zimmerman, D. Ila, C. Muntele, and I. Muntele, Nucl.Instr.Meth.B **241**, 506 (2005).

[77] R. Birtcher, S. Donnelly, L. Rehn, and L. Thome, Nucl.Instr.Meth.B **175**, 40 (2001).

[78] G. Rizza, M. Strobel, K. Heinig, and H. Bernas, Nucl.Instr.Meth.B **178**, 78 (2001).

[79] K. Heinig, T. Muller, B. Schmidt, M. Strobel, and W. Moller, App. Phys. A **77**, 17 (2003).

[80] J. Pivin and G. Rizza, Thin Solid Films **366**, 284 (2000).

[81] G. C. Schatz, M. A. Young, and R. P. Van Duyne, "Electromagnetic mechanism of SERS," Top. Appl. Phys. **103**, 19 – 45 (2006).

[82] W. Rechberger, A. Hohenau, A. Leitner, J. R. Krenn, B. Lamprecht, and F. R. Aussenegg, "Optical properties of two interacting gold nanoparticles," Opt. Commun. **220**, 137 – 141 (2003).

[83] G. Pellegrini, V. Bello, G. Mattei, and P. Mazzoldi, "Local-field enhancement and plasmon tuning in bimetallic nanoplanets," Opt. Express **15**, 10097–10102 (2007).

[84] K. Ripken, "Die optischen konstanten von au, ag und ihren legierungen im energiebereich 2, 4 bis 4, 4 ev," Z. Phys A-Hadron Nucl. **250**, 228–234 (1972).

[85] D. E. Aspnes, "Local-field effects and effective medium theory: a microscopic perspective," Am. J. Phys. **50**, 704 (1982).

[86] H. Wang, D. W. Brandl, F. Le, P. Nordlander, and N. J. Halas, "Nanorice: A hybrid plasmonic nanostructure," Nano Lett. **6**, 827 – 832 (2006).

[87] J. Penninkhof, C. Graf, T. van Dillen, A. M. Vredenberg, A. van Blaaderen, and A. Polman, "Angle-dependent extinction of anisotropic silica/Au core/shell colloids made via ion irradiation," Adv. Mater. **17**, 1484 – 1488 (2005).

[88] S. A. Maier, M. L. Brongersma, P. G. Kik, and H. A. Atwater, "Observation of near-field coupling in metal nanoparticle chains using far-field polarization spectroscopy," Phys. Rev. B **65**, 193408 (2002).

[89] G. Mattei, G. Battaglin, V. Bello, G. De Marchi, C. Maurizio, P. Mazzoldi, M. Parolin, and C. Sada, "De-alloying behaviour of metal nanoclusters in SiO2 upon irradiation and thermal treatments," J. Non-Cryst. Solids **322**, 17 – 21 (2003).

[90] E. Purcell, "Modification of spontaneous emission," Phys. Rev **69**, 681 (1946).

[91] O. L. Muskens, V. Giannini, J. A. Sanchez-Gil, and J. G. Rivast, "Strong enhancement of the radiative decay rate of emitters by single plasmonic nanoantennas," Nano Lett. **7**, 2871 – 2875 (2007).

[92] J. S. Biteen, N. S. Lewis, H. A. Atwater, H. Mertens, and A. Polman, "Spectral tuning of plasmon-enhanced silicon quantum dot luminescence," Appl. Phys. Lett. **88**, 131109 (2006).

[93] H. Mertens and A. Polman, "Plasmon-enhanced erbium luminescence," Appl. Phys. Lett. **89**, 211107 (2006).

[94] H. Mertens, J. S. Biteen, H. A. Atwater, and A. Polman, "Polarization-selective plasmon-enhanced silicon quantum-dot luminescence," Nano Lett. **6**, 2622 – 2625 (2006).

[95] P. Anger, P. Bharadwaj, and L. Novotny, "Enhancement and quenching of single-molecule fluorescence," Phys. Rev. Lett. **96**, 113002 (2006).

[96] P. Bharadwaj, P. Anger, and L. Novotny, "Nanoplasmonic enhancement of single-molecule fluorescence," Nanotechnology **18**, 044017 (2007).

[97] B. M. Deutsch and L. Novotny, "Optical antennae enable nanoscale microscopy and spectroscopy," Laser Focus World **42**, 91 – + (2006).

[98] J. S. Biteen, L. A. Sweatlock, H. Mertens, N. S. Lewis, A. Polman, and H. A. Atwater, "Plasmon-enhanced photoluminescence of silicon quantum dots: Simulation and experiment," J. Phys. Chem. C **111**, 13372 – 13377 (2007).

[99] R. Ruppin and O. J. F. Martin, "Lifetime of an emitting dipole near various types of interfaces including magnetic and negative refractive materials," J. Chem. Phys. **121**, 11358 – 11361 (2004).

[100] P. Bharadwaj and L. Novotny, "Spectral dependence of single molecule fluorescence enhancement," Opt. Express **15**, 14266–14274 (2007).

[101] J. Jackson, *Classical Electrodynamics: second edition* (John Wiley & Sons, New York, 1975).

[102] H. Mertens, A. F. Koenderink, and A. Polman, "Plasmon-enhanced luminescence near noble-metal nanospheres: Comparison of exact theory and an improved Gersten and Nitzan model," Phys. Rev. B **76**, 115123 (2007).

[103] R. Carminati, M. Nieto-Vesperinas, and J. Greffet, "Reciprocity of evanescent electromagnetic waves," J. Opt. Soc. Am. A **15**, 706–712 (1998).

[104] S. Kuhn, U. Hakanson, L. Rogobete, and V. Sandoghdar, "Enhancement of single-molecule fluorescence using a gold nanoparticle as an optical nanoantenna," Phys. Rev. Lett. **97**, 017402 (2006).

[105] E. M. Hicks, O. Lyandres, W. P. Hall, S. L. Zou, M. R. Glucksberg, and R. P. Van Duyne, "Plasmonic properties of anchored nanoparticles fabricated by reactive ion etching and nanosphere lithography," J. Phys. Chem. C **111**, 4116 – 4124 (2007).